Evaluation and application of GPS and altimetry data over central Dronning Maud Land, Antarctica: annual elevation change, a digital elevation model, and surface flow velocity

Dissertation

zur Erlangung des Grades Dr. rer. nat
vorgelegt dem Fachbereich Geowissenschaften
der Universität Bremen

von

Christine Wesche

Alfred-Wegener-Institut für Polar- und Meeresforschung
Bremerhaven

August 26, 2008

Gutachter

Prof. Dr. H. Miller

Prof. Dr. K. Huhn

Prüfer

Prof. Dr. T. Mörz

Prof. Dr. T. von Dobeneck

Promotionskolloquium

am 16. Januar 2009

Name:..... Datum:.....

Anschrift:.....

Erklärung

Hiermit versichere ich, dass ich

1. die Arbeit ohne unerlaubte fremde Hilfe angefertigt habe,

2. keine anderen als die von mir angegebenen Quellen und Hilfsmittel benutzt habe und

3. die den benutzten Werken wörtlich oder inhaltlich entnommenen Stellen als solche kenntlich gemacht habe.

_____, den _____

_____

(Unterschrift)

Wussten sie schon,

dass der Gipfel der Zugspitze
am oberen Ende des Berges abgebracht ist?

Loriot

Contents

List of Figures

List of Tables

Kurzfassung

Die polaren Eisschilde der Erde sind einzigartige Paläoklimaarchive und spielen im rezenten und zukünftigen Klimageschehen eine große Rolle. Ein Abschmelzen dieser großen Süßwasserreservoire ließe nicht nur den Meeresspiegel deutlich ansteigen, sondern hätte veränderte Meeresströmungen zur Folge. Daher ist es von großem Interesse, die derzeitig vorhandenen numerischen Klimamodelle ständig zu verbessern, um Klimaveränderungen und deren Folgen so genau wie möglich darstellen zu können.

In dieser Arbeit wird die Evaluierung von GPS- und Altimeterdaten, sowie deren Anwendungen hinsichtlich der Verbesserungen von Modellen beschrieben. Das antarktische Untersuchungsgebiet, Dronning Maud Land (DML), spielt für die deutsche Polarforschung eine große Rolle, da sich sowohl die Überwinterungsstation Neumayer als auch die Sommerstation Kohnen in diesem Gebiet befinden. Im Umkreis dieser Stationen wurden in verschiedenen Messkampagnen hochgenaue kinematische GPS Messungen durchgeführt, welche die Grundlagen für das hier präsentierte Höhenmodell bilden. Da diese jedoch nur sehr kleinräumig vorliegen, werden sie mit verschiedenen Fernerkundungsdaten ergänzt. Dazu gehören zwei Methoden der flugzeuggestützten Altimetrie, sowie satellitengestützte Laserhöhenmessungen des Ice, Cloud, and land Elevation Satellite (ICESat). Wichtigstes Werkzeug für die Kombination dieser Datensätze ist die Kreuzungspunktanalyse. Hierbei werden Höhendifferenzen zwischen zwei Datensätzen an gleichen Positionen (sogenannten Kreuzungspunkten) ermittelt. Mit Hilfe dieses Verfahrens werden zum einen die Genauigkeiten der Datensätze und zum anderen die Höhendifferenzen der Fernerkundungsdaten zu den hochgenauen GPS Daten ermittelt. Diese berechneten Werte werden dann zur Anpassung der Fernerkundungsdaten an die hochgenauen kinematischen GPS Daten verwendet. Mit Hilfe des geostatistischen Interpolationsverfahrens "Ordinary Kriging" entstand ein verbessertes Höhenmodell mit der Auflösung von 2.5 km $\times$ 2.5 km im Gebiet zwischen 20 °W und 20 °O sowie 69 °S bis 86 °S. Vergleiche mit bereits existierenden Höhenmodellen für die komplette Antarktis zeigen, dass gerade in der Küstenregion des Untersuchungsgietes sehr große Höhenunterschiede von teilweise mehreren 100 m existieren. Durch die Verwendung von bodengebundenen GPS Daten wird gerade in den Küstenregionen DMLs die Genauigkeit erheblich verbessert.

Eine Anwendung des Höhenmodells ist die Neupositionierung der im Untersuchungsgebiet existierenden Eisscheiden. Eisscheiden sind die Grenzen ziwschen benachbarten Einzugsgebieten und können mit Hilfe der aus dem Höhenmodell ermittelten Exposition der Topographie bestimmt werden. Ergänzend dazu wurden statische GPS Messungen ausgewertet, um die Oberflächengeschwindigkeit und daraus

die Deformation des Eises im Umkreis der Kohnen Station zu ermitteln. Diese Ergebnisse tragen dazu bei, die Interpretation des zwischen 2001 und 2006 an der Kohnen Station im Rahmen des European Project for Ice Coring in Antarctica (EPICA) gebohrten Eiskerns (EDML) zu verbessern.
Mit Hilfe der ICESat Altimeterdaten aus verschiedenen Messperioden zwischen 2003 und 2007 wurde zusätzlich zu den oben beschriebenen Arbeiten der Trend der jährlichen Höhenänderungen im Untersuchungsgebiet berechnet. Aus Kreuzungspunktanalysen wurde das jährliche Mittel der Höhenänderungen in der Küstenregion und auf dem Plateau im Inneren Dronning Maud Lands ermittelt. Die mittleren jährlichen Höhenänderungen von 0.06 m (Küstenregion) bzw. -0.02 m (Plateau) zeigen einen abnehmenden Trend der Höhe im Untersuchungsgebiet.
Die neu gewonnenen Datensätze geben Aufschluss über die Gegebenheiten im Untersuchungsgebiet und können als Eingangsgrößen der numerische Modellierung diese verbessern.

Abstract

The polar ice sheets are unique paleoclimatic archives and play an important role in recent and future climate. The melting of the big freshwater reservoirs will not only increase the global sea level, but will also influence the ocean currents. Therefore, it will be of particular interest to improve the currently available numeric climate models to achieve more accurate statements about climatic change and its consequences.

In this work, the evaluation and the different applications of GPS and altimetry data will be described in respect to enhance models. The antarctic area of investigation, Dronning Maud Land (DML), is of particular interest for German polar research, because both the overwintering station Neumayer and the summer station Kohnen are located within it. In the surroundings of these two stations, highly accurate kinematic GPS measurement were made, which will be the basis for the digital elevation model presented here. Because these data are spatially limited, they are supplemened with remotely sensed data. For this purpose, two airborne altimetry data sets and spaceborne laser altimetry data of the Ice, Cloud, and land Elevation Satellite (ICESat) are used. The basic tool for the combination of these data sets is the crossover-point analysis. In this process, the elevation differences at equal positions (crossover points) of two different data sets are determined. On the basis of this process, the vertical accuracy of the different data sets and the elevation differences to the ground-based kinematic GPS data are determined. These differences are used to shift the remotely sensed data to the highly accurate ground-based GPS data. With the aid of the geostatistical interpolation method "Ordinary Kriging" an improved digital elevation model with a resolution of 2.5 km $\times$ 2.5 km of the region within 20°W to 20°E and 69°S up to 86°S was generated. A comparison with commonly used digital elevation models, covering the whole continent, shows high elevation differences up to several 100 m in the coastal region. Due to the use of ground-based highly accurate GPS data, the elevation model could be significantly improved above all for the coastal region of DML.

An application of this elevation model is the re-locating of the ice divides in the area of investigation. Ice divides are the lines between two neighboring catchment areas. Their location is determined by the aspect of the topography. Additionally, static GPS measurements are processed to determine the surface flow velocity of the ice, which is further used for the calculation of the strain rate in the vicinity of Kohnen station. These results will improve the interpretation of climate proxies of the deep ice core (EDML), which was drilled between 2001 and 2006 at Kohnen station within the European Project for

Ice Coring in Antarctica (EPICA).

On the basis of ICESat ice sheet altimetry data from different measurement periods between 2003 and 2007, the mean annual elevation change trend was calculated. From crossover-point analyses mean annual elevation change was determined for the coastal region and the plateau. The mean annual elevation change trend shows decreasing elevations in the coastal region (0.06 m) as well as at the plateau (-0.02 m).

The data sets presented here give an explanation about the natural facts in the area of investigation and may be used as input parameter, to improve numeric modeling.

1. Introduction

Ice sheets are unique archives for reconstructing the paleoclimate and play an important role in the Earth's past, present and future climate system. They have direct and indirect impacts on patterns of oceanic and atmospheric circulation worldwide. Furthermore, they are sensitive indicators and modulators of climate variability and change. Changes in mass balance of the polar ice sheets resulted in global sea level change of 1.8 mm a^{-1} since 1961 and 3.1 mm a^{-1} since 1993 (Intergovernmental Panel on Climate Change (IPCC), 2007). Several investigations on elevation changes of the Antarctic ice sheet were carried out for estimating the mass loss and gain (Wingham and others, 1998; Davis and Ferguson, 2004; Zwally and others, 2005; Helsen and others, 2008) and thus estimate Antarctica's contribution to sea level change (Arthern and Hindmarsch, 2006; van den Broeke and others, 2006).

Numerical modeling of ice sheets plays a big role in understanding past and future climate and offers estimations to key questions in geoscience, e.g. estimating the consequence of climate variability, reconstructing and forecasting of the global sea level. Digital elevation models (DEMs) provide important boundary conditions for accurate numerical ice sheet modeling (Paterson, 1994; Huybrechts and others, 2000; Huybrechts, 2003). Their accuracy and resolution have a high impact on the quality of ice dynamic modeling (Alley and others, 2005).

This chapter gives a short introduction in the world's largest ice sheet and the area of investigation. An overview of two commonly used digital elevation models and the motivation of this work is also given in the following sections.

1.1. Antarctica and area of investigation

The world's southernmost continent Antarctica is nearly completely covered with ice and snow and stores $\sim$90 % of the world's ice which equivalents to $\sim$70 % of its freshwater. The ice sheet covers an area of $\sim 12.4 \times 10^6$ km^2 and has an average ice thickness of $\sim$2.4 km. The maximum ice thickness is 4.776 km (www.scar.org/information/statistics/). A melting of the whole Antarctic ice sheet would result in a global sea level rise of about 65 m (Massom and Lubin, 2006).

Antarctica is divided into three parts: (i) East Antarctica, (ii) West Antarctica, which are separated by the Transantarctic Mountains, and (iii) Antarctic Peninsula. The three largest floating ice masses (ice shelves) are: Filcher-Ronne Ice Shelf and Ross Ice Shelf in West Antarctica, and the Amery Ice Shelf in

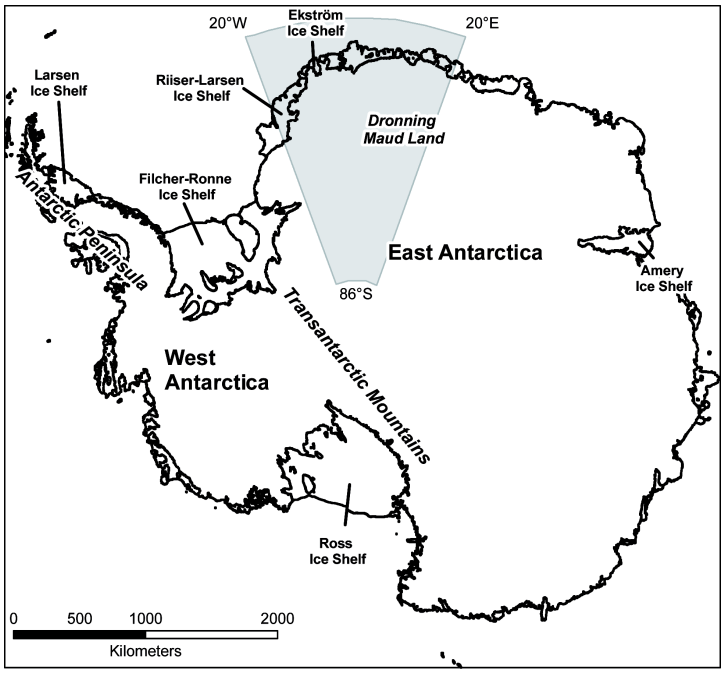

Figure 1.1.: Map of the Antarctic continent. The area of investigation is marked with the grey shaded circle slice. The grounding and coast line are taken from MODIS Mosaic of Antarctica (MOA - Haran and others (2006)).

East Antarctica (Figure 1.1).

The mass balance of the Antarctic ice sheet is dominated by accumulation, basal melting, and calving of ice bergs at the ice edges (Rignot and Thomas, 2002). To observe significant effects on mass balance of the Antarctic ice sheet, long time trends in net balance changes have to be measured. Alley and others (2007) show that the current warming could result in a slight growth of the ice sheet averaged over the next century. Because of warmer temperatures, the global evaporation increases, which in turn increases the snowfall over Antarctica.

The area of investigation is located in Dronning Maud Land (DML) in East Antarctica and covers the region between 20°W and 20°E and 69°S up to 86°S (shaded area in Figure 1.1). It comprises different landscapes, the coastal region, the inland ice plateau and the mountainous region in-between. For geographic names see Figure 1.2.

The focus of the ground-based GPS data is set on two subset regions, marked with blue rectangles in Figure 1.2. The first region is the area surrounding the German summer station Kohnen, where within the European Project for Ice Coring in Antarctica (EPICA) a deep ice core (EDML) was drilled. EDML was drilled between 2000/01 and 2005/06 (EPICA Community Members, 2006) and lies in the immediate vicinity of an ice divide on the Antarctic plateau (a description of ice divides is given in Section 4.3). The area can be described as a flat region with slight slopes to the West (Wesche and others, 2007).

The second investigated area is the coastal region in the hinterland of the German overwintering station

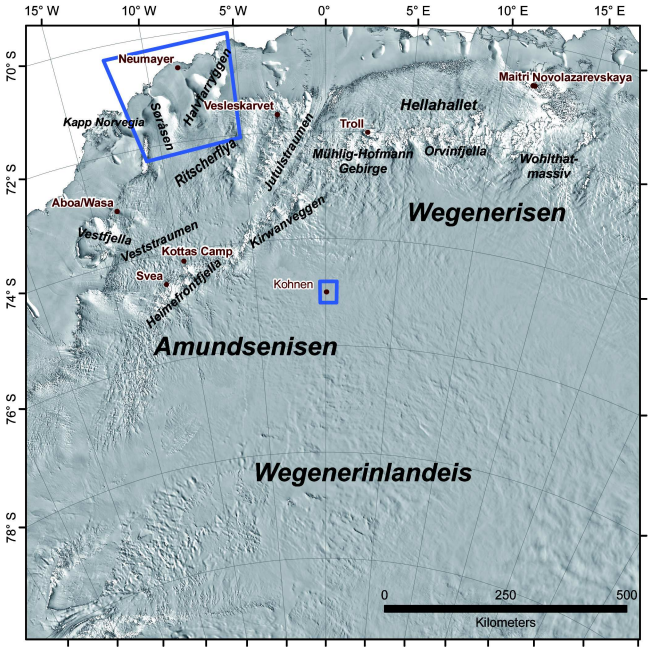

Figure 1.2.: MODIS Mosaic of Antarctica satellite image of the area of investigation (Haran and others, 2006). The blue rectangles represent the areas of investigation in publication I and II.

Neumayer. The two grounded ice ridges surrounding the Ekströmisen, on which Neumayer is located (Søråsen (West) and Halvfarryggen (East)), rise up to a maximum height of 760 m (WGS-84) at Søråsen. Southwards of the ice ridges, the elevation increases to the Ritscherflya up to 1000 m (WGS-84). This area is characterized by steep slopes at the transition from grounded ice to the floating ice of the ice shelf (grounding zone) and moderate slopes at the remaining parts. The mean slope is 0.75° with a standard deviation of 0.50° and is thus mostly higher than the slopes at the plateau (0.16 ± 0.14°).

For both regions, DEMs derived from different data sets are presented in Paper I (Wesche and others, 2007) and Paper II (Wesche and others, accepted). Additionally, a flow field based on static GPS measurements is derived from static GPS measurements for the surrounding of the Kohnen station. To get a complete picture of central DML, a new improved DEM for the region between 20° W and 20° E is generated by a combination of ground-based GPS and remotely sensed altimetry data (Paper III - Wesche and others (in review)).

1.2. Existing elevation models

Currently existing DEMs are based on a multiplicity of different measurement methods are used for comparison with the newly derived DEM. In this work, two commonly used DEMs. The one published in 1997 by J. L. Bamber and R. A. Bindschadler (Bamber and Bindschadler, 1997), hereafter called JLB97 and the DEM of the Radarsat Antarctic Mapping Project (RAMP), described by Liu and others (2001),

are used for comparison with the newly derived DEM. Both data sets are available at the National Snow and Ice Data Center (NSIDC - http://nsidc.org/).

1.2.1. JLB97

The DEM, generated by Bamber and Bindschadler (1997), is derived from the geodetic phase of the European Research Satellite 1 (ERS-1). The ERS-1 was launched on 17 July 1991 in a nearly circular orbit at an altitude of 780 km with an inclination of 98.5°. The nadir-looking radar altimeter onboard operated in Ku-band (13.5 GHz) in ocean or ice mode. The accuracy of the radar altimeter was determined to be 10 cm (Seeber, 2003). The across-track spacing of ERS-1 ground measurements at 70° latitude is 2 km and the along-track spacing of data points is 335 m. Bamber and Bindschadler (1997) generated a 5 km $\times$ 5 km resolution surface topography of the whole Antarctic ice sheet up to 81.5°S. The elevation accuracy of < 1.5 m given in Bamber and Huybrechts (1996) is valid for surface slopes less than 0.4° (JLB97 is an improved DEM of the one presented in Bamber and Huybrechts (1996), but in Bamber and Bindschadler (1997) no detailed accuracy information is given) (Figure 1.3).

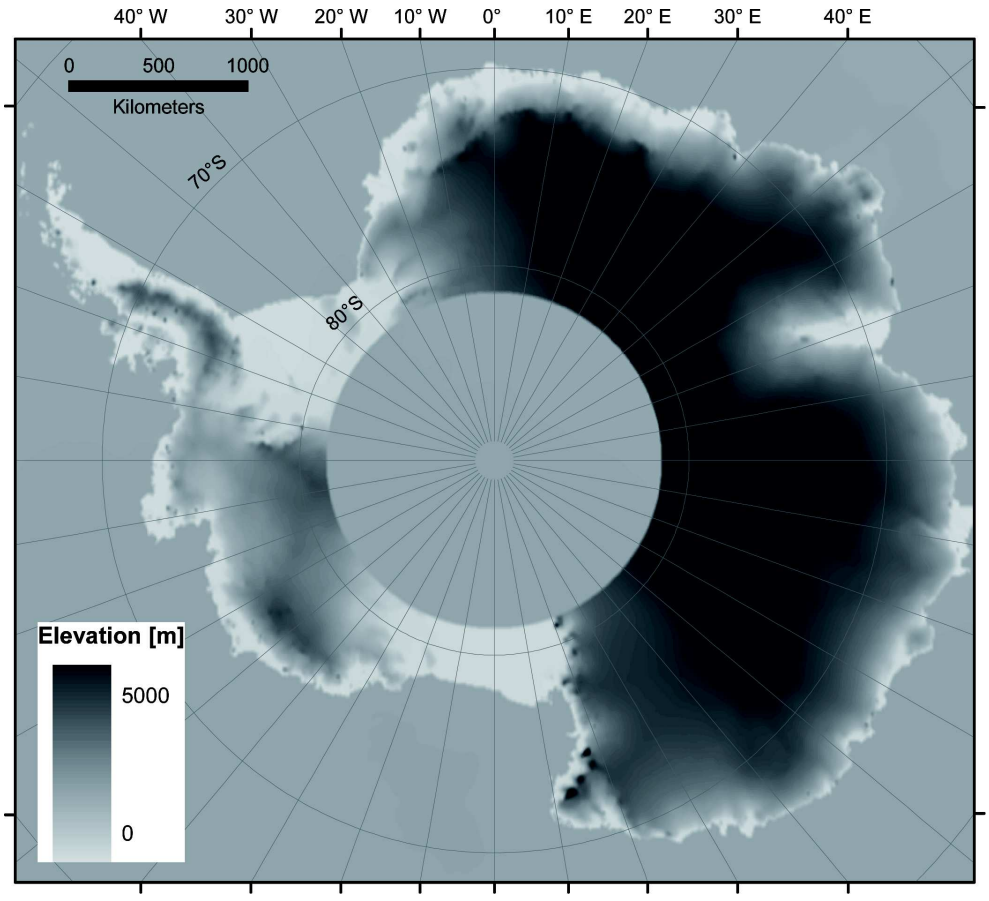

Figure 1.3.: The DEM of Bamber and Bindschadler (1997) gridded from the 5 km $\times$ 5 km ascii data set.

1.2.2. RAMP

The DEM of the Radarsat Antarctic Mapping Project (RAMP) consists of satellite altimetry, airborne radar survey data, updated Antarctic Digital Database (ADD) data (version 2) and large-scale topographic maps from the U.S. Geological Survey (USGS) and the Australien Antarctic Division (Figure 1.4). The satellite data are identical with the ones used for the JLB97 DEM. The DEM is available in 1 km $\times$ 1 km, 400 m $\times$ 400 m and 200 m $\times$ 200 m resolution. RAMP covers the grounded ice masses of the Antarctic continent. The absolute vertical accuracy depends on the region. Over rugged mountainous areas the standard deviation of the vertical accuracy is ± 100 m, for steeply sloped coastal regions ±15 m, on the ice shelves ±1 m, for the gently sloped interior ±7.5 m, for rough and steeply sloped portions of the ice sheet perimeter ±17.5 m and ±50 m south of 81.5 °S (Liu and others, 1999, 2001).

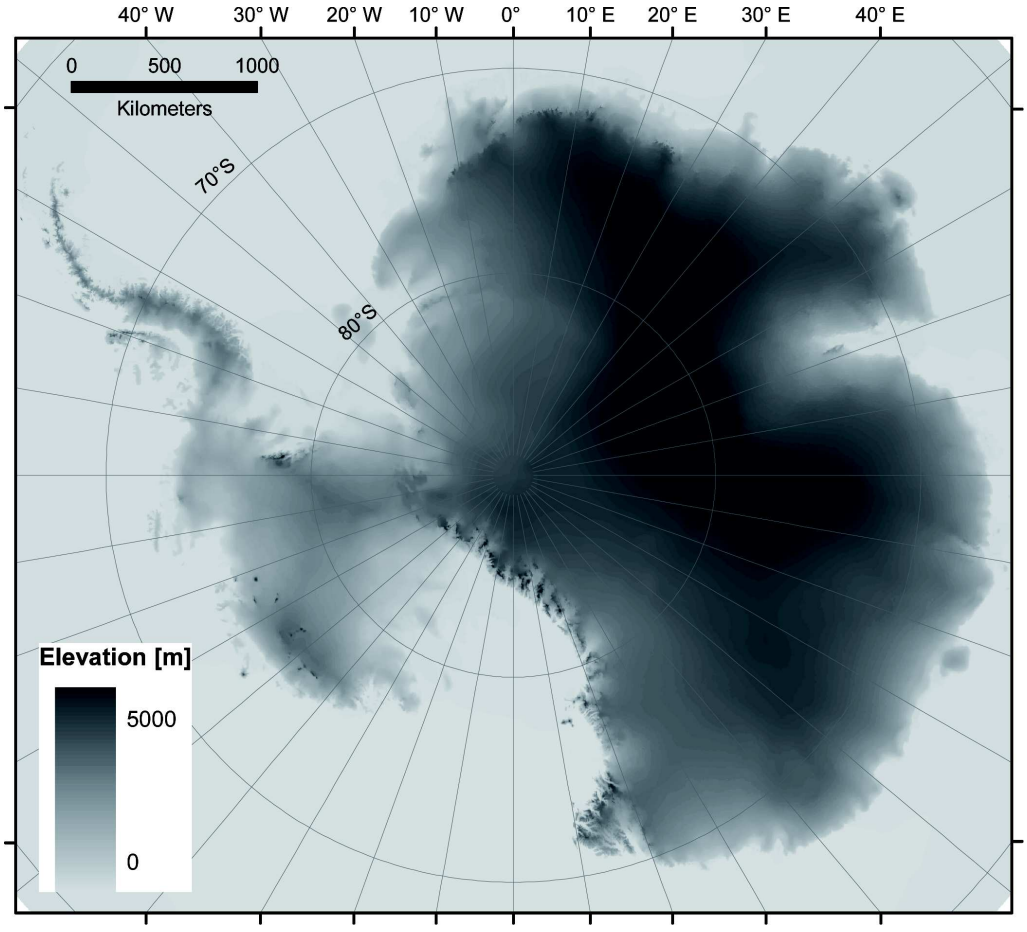

Figure 1.4.: The RAMP DEM with a resolution of 200 m $\times$ 200 m.

1.3. Motivation

The EDML deep-drilling site is situated on the plateau of DML, in the direct vicinity of an ice divide. Being drilled in the Atlantic sector of Antarctica, the deep ice core is used to study the teleconnection of northern and southern hemisphere climate variability in the past (EPICA Community Members, 2006). For accurate paleoclimatic interpretation of the ice core, the knowledge of past and present ice dynamics is essential. The mean flow velocity at the EDML deep-drilling site is 0.76 m a^{-1} (Wesche and others, 2007) and by an estimated age of 128 ka at a depth of 2366 m of the ice drilled at EDML (Ruth and others, 2007), the snow would have been deposited 96.8 km upstream (assuming a constant flow velocity). Based on an accurate DEM the location of topographic ice divides can be determined (see Section 4.3) and ice dynamic modeling and thus a localization of the deposition area of the snow can be improved. The surface topography and surface slopes at the steep margins are a crucial input parameter for climate modeling. Krinner and others (2007) show, that the gradient of decreasing precipitation, towards the interior of an ice sheet, is bounded by three effects: (i) orographic effect of the steep margins of the ice sheets, (ii) decreasing oceanic moisture by increasing distance to the coast and (iii) the temperature gradient towards the plateau regions. To reduce uncertainties of climate modeling and thus improve the estimation of future mass balance and sea level change an accurate elevation model is an important boundary condition (Paterson, 1994; Huybrechts and others, 2000; Huybrechts, 2003). Both DEMs described in the previous section have shortcomings in the mountainous and coastal regions as shown by Bamber and Gomez-Dans (2005). Elevation differences up to 1000 m between the JLB97 and RAMP DEM make the need of an improved DEM very clear.

In this work, four different data sets were used to generate an improved DEM: (i) ground-based kinematic GPS, (ii) airborne radar altimetry, (iii) airborne radio echo sounding, and (iv) spaceborne laser altimetry. By combining different altimetry measurement methods disadvantages of single data sets can be reduced. For example, highly accurate ground-based GPS data are not affected by cloud cover or penetration of the signal into the snow surface, which cause false readings by applying laser, respectively radar altimetry. They are recorded near the surface and give the best approximation of the true surface. But these data are very limited in their spatial extent due to the time consuming survey speed, and are therefore be supplemented with remotely sensed data, if larger regions are investigated.

The core of this work is the combination of these data sets with different typical features to a highly accurate elevation data set for central DML. Furthermore, ice divides were localized in DML and the spaceborne laser altimetry is used to estimate the mean elevation change between 2003 and 2007.

This thesis answers the following questions:

1. Is it possible to determine annual elevation change from spaceborne laser altimetry data?
2. How can different elevation data sets be combined into one to obtain an improved DEM?

3. Are there elevation differences between the improved regional DEM and currently existing continental DEMs?
4. Can the location of the ice divides in DML be confirmed or improved with the new DEM?
5. How fast does the ice move and how large are the strain rates around the EDML deep-drilling site?

2. Scope of papers

Paper I: Wesche, C., Eisen, O., Oerter, H., Schulte, D. and D. Steinhage. Surface topography and ice flow in the vicinity of the EDML deep-drilling site, Antarctica.
Journal of Glaciology, Vol. 53, No. 182, pp. 442-448, 2007.

This paper investigates the surface topography in the vicinity of the EDML deep-drilling site derived from highly accurate ground-based kinematic GPS measurements and spaceborne laser altimetry from NASA's Ice, Cloud, and land Elevation Satellite (ICESat). Because of the data point coverage in the area of investigation, the surface topography has a horizontal resolution of 5 km x 5 km. Additionally, static GPS measurements were used to determine the flow field around the deep-drilling site. Based on the surface velocities, a strain-field for the area around the drilling site could be established and contribute to an improved interpretation of EDML ice-core data. I processed most of the data and wrote the manuscript, which was improved by the co-authors who also contributed to the data base.

Paper II: Wesche, C., Riedel, S. and D. Steinhage. Precise surface topography of the grounded ice tongues at the Ekströmisen, Antarctica, based on several geophysical data sets.
ISPRS Journal of Photogrammetry and Remote Sensing, accepted.

This publication describes the method of combining different data sets to a DEM. The grounded part of a coastal region in the hinterland of the German overwintering station Neumayer II is investigated with highly accurate ground-based kinematic GPS, ICESat laser altimetry and airborne radar altimetry. A new precise surface topography was generated with a spatial resolution of 1 km x 1 km. The comparison with existing DEMs show obvious differences. Most of the data were processed by myself. The co-authors helped with interpreting the data and improved the manuscript I wrote.

Paper III: Wesche, C., Riedel, S., Eisen, O., Oerter, H., Schulte, D. and D. Steinhage. An improved DEM and refined locations of ice divides for Dronning Maud Land, Antarctica
Journal of Glaciology, in review

In this paper the combination of four altimetry data sets to an accurate elevation data sets in DML is pre-

sented. The methods established in the first two publications were applied to generate a new improved DEM for DML within 20°W and 20°E and 69°S to 86°S. Due to the use of ground-based GPS data, the DEM could be improved, which is shown by a comparison with commonly used DEMs. The DEM has a resolution of 2.5 km $\times$ 2.5 km and was used for the localization of the ice divides in DML. A flow field, consisting of 18 velocity measurements, shows the flow conditions near the German summer station Kohnen and the wider surroundings. I processed and interpreted the data and wrote the manuscript. The co-authors contributed to the data base and improved the manuscript.

Paper IV: Drews, R., Rack, W., Wesche, C. and V. Helm. A new digital elevation model in western Dronning Maud Land (Antarctica), based on differential SAR Interferometry.
IEEE Transactions on Geoscience and Remote Sensing, accepted.

This study describes the methodology of interferometric SAR analyses and presents a high resolution (50 m $\times$ 50 m) DEM for the grounded part of coastal DML within 5° to 20°W and up to 76°S. The paper shows also an accuracy assessment of generated DInSAR DEM, checked by ground-based kinematic GPS data, laser scanner data, and ICESat data and the JLB97 DEM and RAMP DEM.
Own contributions to Paper IV:

- processing of the GLA12 (see section 3.3) release 24 data, which were used as ground control points
- processing of the GLA12 release28 data, which were used for comparison with the final DInSAR DEM
- processing of the ground based kinematic GPS data, including the interpolation of the reference stations
- contributions to the text

3. Data and Methods

The focus of this work is the generation of an improved DEM. To achieve an optimal result, four measurement methods are combined in a way that uses the advantages and compensates for the disadvantages of the single methods.
The DEM consists of four different data sets:

(i) highly accurate ground-based kinematic GPS measurements
(ii) airborne radar altimetry (ARA)
(iii) airborne radio echo sounding (RES)
(iv) spaceborne laser altimetry (ICESat).

In the following sections, the different GPS, ARA, RES and ICESat are presented and discussed with respect to their advantages and disadvantages.

3.1. Global Positioning System (GPS)

The Global Positioning System (GPS) is part of the Global Navigation Satellite System (GNSS) and was developed by the US Department of Defense in 1973. The present GPS, which is used here, is a navigation system with timing and ranging (NAVSTAR) GPS. A detailed description is given in Hofmann-Wellenhof and others (2008). In the following sections, the principle of positioning, possible error sources, and the different processing methods are described.

3.1.1. Positioning with GPS

The core of the NAVSTAR GPS are 32 operational satellites in 20200 km altitude above the Earth's surface. Together with a dual frequency GPS receiver, operating with the L1 carrier frequency at 1575.42 MHz and L2 at 1227.60 MHz, it is possible to determine the precise position of every point at the Earth's surface. For position determination, at least four simultaneously operating satellites have to be visible for the GPS receiver. Basically, the distances (range) between the satellites (equipped with an atomic clock) and the GPS receiver (equipped with a quartz clock) are determined by the signal run

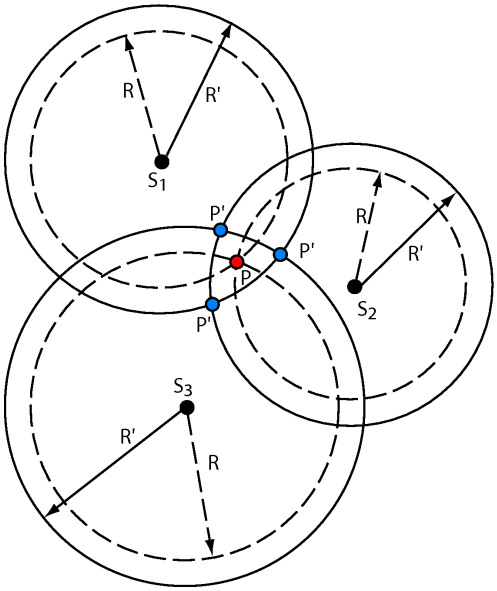

Figure 3.1.: Principle of pseudorange positioning with three satellites.

time, whereas the positions of the satellites are always known. The range is defined as the radius of a sphere, which has the center point at the satellite position. In Figure 3.1 the positioning is presented schematically. Three satellites ($S_{1\text{-}3}$) are needed for estimating the position (longitude, latitude and elevation). Because of the clock offset of the GPS receiver at the Earth's surface to the satellite's clock, the measured range (R') differs from the true range (R), which results in three possible solutions for the position (P'). If a fourth satellite is included, the time difference between the measured and the true range and thus the true position at the surface (P) can be calculated.

3.1.2. GPS errors

GPS measurements are affected by several systematic errors, which can be separated into three groups: (i) satellite-related errors (clock bias and orbital errors), (ii) propagation-medium-related errors (ionospheric and tropospheric refraction) and (iii) receiver related errors (antenna phase center variation, clock bias and multipath). Table 3.1 shows a short summary of the systematic errors and their contribution to uncertainties of the calculated position. Satellite and receiver specific errors can be eliminated by differential GPS (DGPS) processing (see following section) and most of the systematic errors are minimized by including precise ephemerides (highly accurate orbital information) and atmospheric models. Multipath errors are signal delays caused by buildings, surface reflections etc. Because of the use of a Choke Ring antenna and the typically flat surface, they can be neglected in the area of investigation, but were mentioned here for the sake of completeness. A more detailed description of the error sources and their minimization is given for example in Hofmann-Wellenhof and others (2008).

Table 3.1.: Overview of the ranges of the systematic GPS errors after Hofmann-Wellenhof and others (2008).

Error source	Error [m]
Ephemerides data	2.1
Satellite clock	2.0
Ionosphere	4.0
Troposphere	0.5
Multipath	1.0
Receiver error	0.5

3.1.3. Differential GPS processing

Differential GPS processing (DGPS) is a technique, where at least two GPS receivers are required. One static receiver with known coordinates (longitude, latitude and elevation) as reference station, which are taken into account when determining the position of the so-called rover. The corrections which are determined by calculating the fixed position of the reference receiver are applied to the rover. The distance between the reference station and the rover is called baseline.

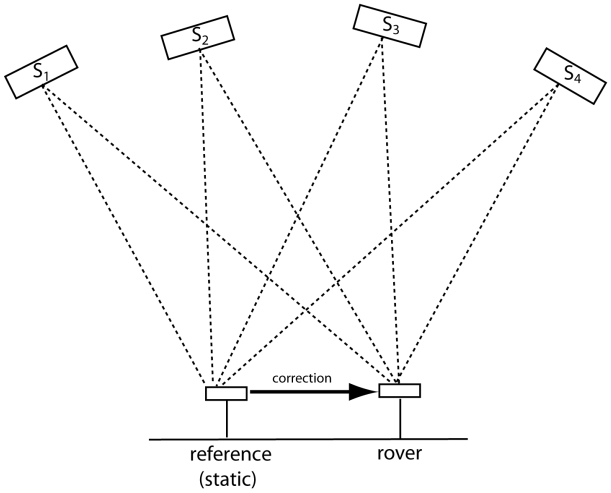

Figure 3.2.: Basis concept of differential GPS after Hofmann-Wellenhof and others (2008).

The reference station calculates the pseudorange correction. This can be done in real-time and results in an improvement of the accuracy of the positions with respect to the reference station immediately. Nevertheless, in real-time there are no precise orbital information (ephemerides) available (Hofmann-Wellenhof and others, 2008). To reduce the systematic error nearly completely, the DGPS post-processing technique is used in this work. The DGPS post-processing is performed with post-processing software packages and several permanent and short-time reference stations. In Figure 3.3 and in Table A.1 and A.2 in the appendix all permanent and short-time references stations are shown.

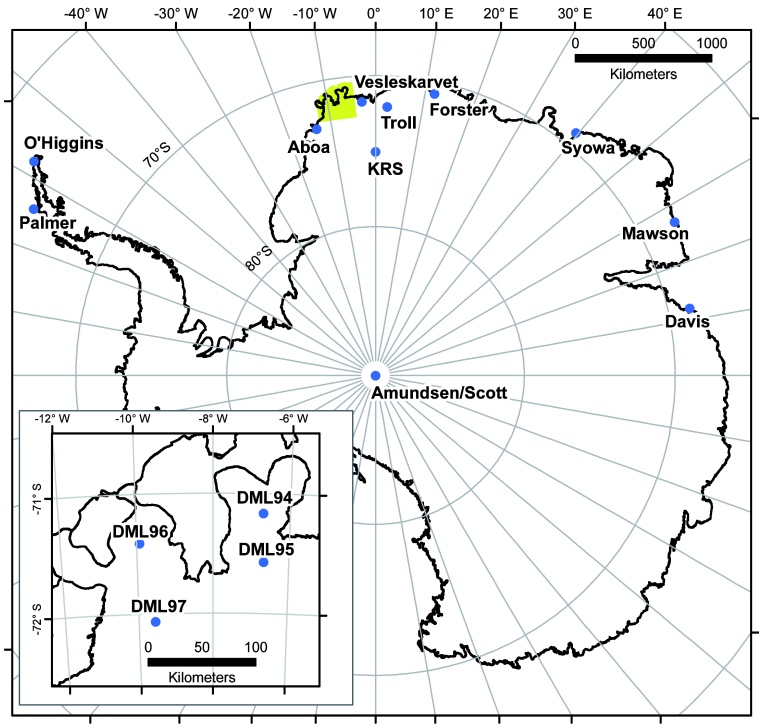

Figure 3.3.: A map of GPS reference stations used here. The black lines are the grounding and coast line from MOA (Haran and others, 2006).

During processing the ionospheric-free solution (reduces the effects of the ionospheric refraction (King, 2004; Hofmann-Wellenhof and others, 2008)) and precise ephemerides were always applied. Two different techniques are used in this investigation: (i) static DGPS processing for point observations and (ii) kinematic DGPS processing for profile measurements.

Static DGPS processing

Static processing is the determination of the accurate position of a rover assumed stationary. In this work it is used for establishing local reference stations for kinematic DGPS processing (Wesche and others, accepted) and for the calculation of surface velocities (Wesche and others, 2007). In the surrounding of the Kohnen station (see Section 1.1), the positions were determined with Trimble Geometrics Office (TGO™) and the costal positions were calculated with Waypoint's static solution GrafNet™. To reduce systematic GPS errors affected by long baselines (because of the sparse distribution of reference stations), local reference station have to be set up and their position has been determined by using a net of several reference stations in all possible directions (Figure 3.4).

A list of static measurements determined during this work is given in Table A.3 in the appendix. In Wesche and others (2007) a detailed description of the velocity determinations and hence resulting strain-field analyses around Kohnen is given.

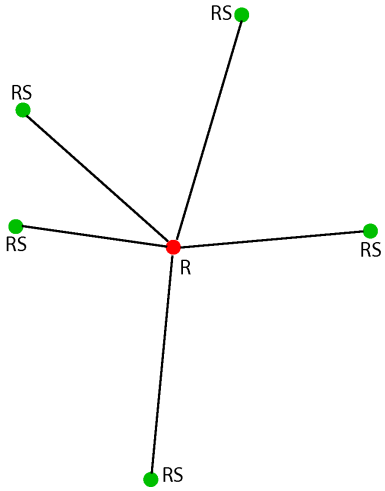

Figure 3.4.: Schematic illustration of network of reference stations. The rover (R) is nearly ideally surrounded by the reference stations (RS).

Kinematic GPS processing

During kinematic processing, the rover moves relative to the reference station. As described in the publications, the kinematic GPS data used here were recorded with the aid of snow vehicles. The recorded profiles of ground-based kinematic GPS measurements are shown in Figure 3.5. Kinematic raw data were processed with TGO™ and Waypoint's kinematic solution GrafNav™. In order to improve the accuracy of the rover position, the length of the baselines has been reduced by using local reference stations. For example, for the leaf like and pentagon profiles on Halvfarryggen and Søråsen (see Figure 3.5) the local stations DML94 to DML97 (see Figure 3.3 inset and Table A.3 in the appendix) were used, and therefore the maximum baseline length was 26 km (except for one profile). For GPS profiles using a local reference, the mean elevation accuracy is 0.03 m (in this work: accuracy = the mean absolute elevation difference calculated by crossover-point analyses) (Wesche and others (2007) and Wesche and others (accepted)). For profiles in the region of the Ekströmisen, using data collected at the reference station Vesleskarvet near the South African station SANAE IV, the mean accuracy is 0.06 m (Wesche and others, in review). For processing of the kinematic data collected on the logistic traverse from Neumayer station to Kohnen station (Figure 3.5), two different reference stations were used (Vesleskarvet for the first part and the reference station at the Finnish Aboa station for the second part). Due to a baseline length of several hundred kilometers, the elevation accuracy is lower compared to the other GPS profiles. Unfortunately, there are no crossover points for the determination of the elevation accuracy. Therefore, the accuracies of the processing report, given by Waypoint, were used. All in all, 78 % of the data points are in the accuracy range of 0.05 - 0.40 m (Drews and others, accepted; Wesche and others, in review).

Because the ellipsoidal heights of ice shelves are influenced by the ocean tides, all kinematic GPS data collected there have to be corrected for tidal movement. For this purpose, the global tide model TPXO7.1

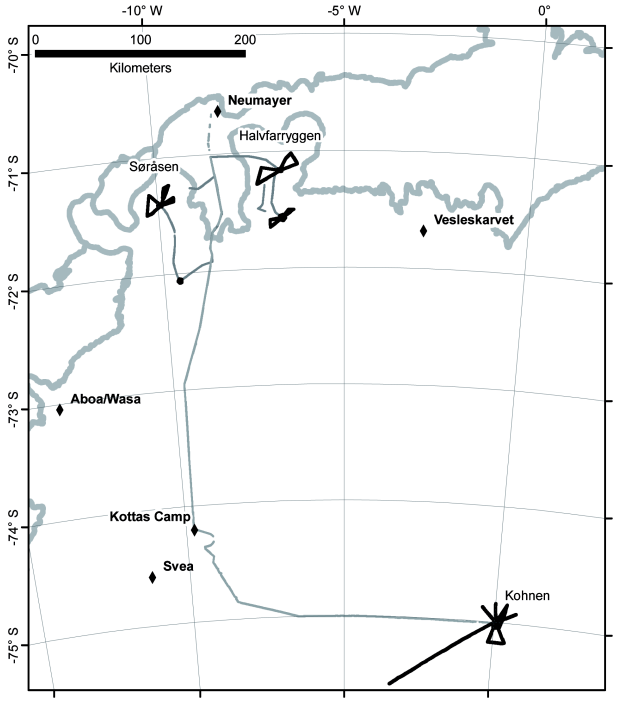

Figure 3.5.: Location of the ground based kinematic GPS profiles. The black lines indicate data processed with a local reference station (max. baseline length 26 km, except for the long profile around Kohnen station), whereas the thin grey profiles were processed with remote reference stations (baseline length greater 100 km). The grounding and coast line (bold grey lines) were derived from MOA (Haran and others, 2006). Stations and camps are marked with black rhombi.

(http://www.coas.oregonstate.edu/research/po/research/tide/global.html) was applied by using the Ohio State University Tidal Prediction Software (OTPS) (Wesche and others, in review).

3.2. Airborne altimetry

Airborne altimetry data were recorded with sensors installed on the AWI research aircraft POLAR2. To determine the surface elevation from altimetry, several on-board instruments were used: (i) two Trimble 4000SSI GPS receivers with roof mounted GPS antennas each for determining the exact flight track, (ii) a HONEYWELL AA-300 radar altimeter system for determining the flying altitude above ground and (iii) a radio echo sounding system, which is specially designed for the use in polar regions.

The airborne data used here are a byproduct of the pre-site survey for the EPICA project, respectively the VISA survey (Validation, densification, and Interpretation of Satellite data in Antarctica using airborne and groundborne measurements for the determination of gravity field, magnetic field, ice-mass balance and crustal structure). Because of their independence of weather conditions, the data are suitable for extending the ground-based kinematic GPS data.

The basic principle of airborne altimetry is to determine the aircrafts flying altitude above ground and

subtract it from the GPS heights recorded during the flight (Figure 3.6).

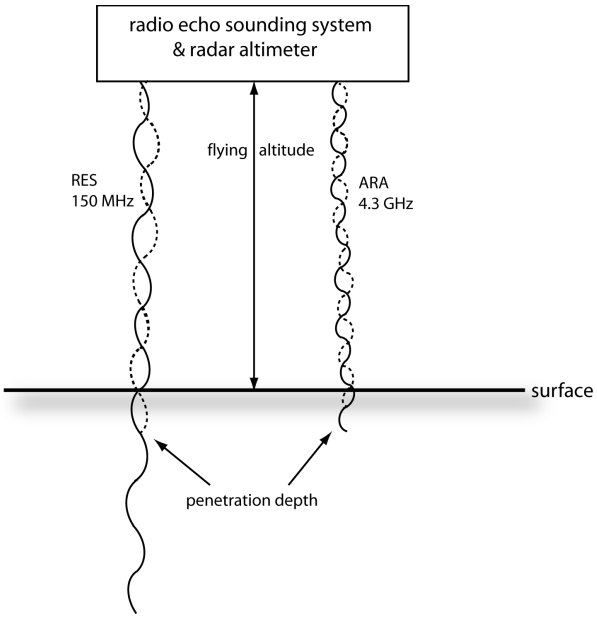

Figure 3.6.: Schematic figure of the basics of airborne altimetry. The solid wave lines represent the emitted radar signal and the dashed wave lines the backscattered signal.

The different approaches of airborne radar altimetry (ARA) and radio-echo sounding (RES) will be described in the following two sections.

3.2.1. Radar altimetry

The basic of this airborne radar altimetry is to calculate the height of the aircraft above surface by measuring the travel time of the radar signal from its emission to arrival of the backscattered signal. Since the altimeter emits microwave radiation (C-band, 4.3 GHz), the signal penetrates clouds and is therefore independent of weather conditions. But there are serious limitations of this method. Brenner and others (1983) show that slopes are influencing the vertical accuracy of the radar altimeters. The so called 'slope-induced error' is caused by the reflection of the radar signal from the antenna nearest point instead of the nadir point. The measured surface lies over the true surface (for more information on the slope-induced error, see Brenner and others (1983)). Another error source of the radar altimetry is the penetration of the signal into the snow surface. The absorption of the radar signal is mainly controlled by the snow temperature and decreases from the coast to the interior of Antarctica. This yields to a spatial and temporal variation of the penetration depth (Legresy and Remy, 1998).

The operational altitude range above the surface of the HONEYWELL-AA 300 radio altimeter system is 0-2500 ft, which is equivalent to 0-760 m (Honeywell AA-300 Manual, 1998). According to the ground speed of the aircraft of about 240 km h^{-1} and a measurement interval of one second, the along track

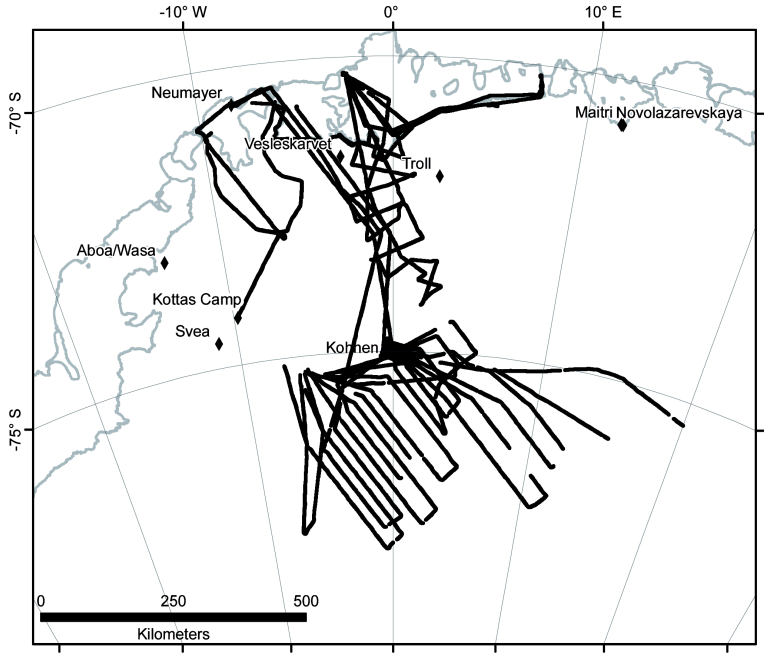

Figure 3.7.: Location of the ARA profiles. The grounding and coast line, derived from MOA, are presented in bold grey lines (Haran and others, 2006). Stations and camps are marked with black rhombi.

spacing of data points is 66.7 m. Because of the limited operational range of the radar altimeter, only two campaigns (1998/99 and 2000/01) with usable data are available (Figure 3.7).

The first step of processing the ARA data is the kinematic DGPS processing (see Section 3.1.3) of the GPS data, recorded during flight by using TGO™. Reference stations were chosen depending on the location of the starting point of the flight track and the availability of reference data during the whole flight. In campaign 1998/99, all profiles were processed with reference data of Vesleskarvet. Data of campaign 2000/01 were processed with reference data collected at the Japanese station Syowa, Vesleskarvet and Kohnen Reference Station (KRS). Because of the range of the aircraft and the sparse distribution of reference stations, long baselines could not be avoided during processing, which reduced the accuracy of the kinematic DGPS processing.

Processing (with TGO™) resulted in a root-mean-square of the positioning accuracy of 0.01 m, but this value is overoptimistic. This software reported error has to be multiplied by 5 to 20 to get a realistic value for the positioning accuracy (personal communication M. King, 2006).

The mean positioning accuracy of the airborne kinematic GPS can be assumed to range between 0.2 and 0.4 m. Because of the aircrafts orientation (roll, pitch and yaw angle) and the resulting elevation errors, the ARA data have to be processed with regard to the aircrafts orientation. This is done with a modified Airborne SAR Interferometric Altimeter System (ASIRAS) processor, which was developed by V. Helm and S. Hendricks from AWI. The processor requires the post-processed GPS data and the according raw navigation file of the flight. Based on the installation coordinates of the radar altimeter on-

board the aircraft and the navigation file, which includes the orientation angles, the error of the reflected radar signal can be estimated. With the aid of the operating time (seconds per day), the GPS height is corrected by the determined altitude above the ground of the aircraft. However, the elevation accuracy still depends on the surface slope. The slope-induced-error (ΔH) over a slope (α) with a flying altitude (H) above ground can be estimated by:

$$\Delta H = \frac{H\alpha^2}{2} \tag{3.1}$$

For α = 0.026rad (1.5°) and H = 760 m (flying altitude above ground), the slope-induced error amounts to 0.26 m. The maximum slope in the area of investigation is 12° (0.078 rad), which results in a maximum slope-induced error of 16.59 m. To avoid a high slope-induced error, all ARA data recorded over a surface topography with a slope over 1.5° were removed from this investigation. The vertical accuracy (2σ corrected) of 1.8 m is determined by a crossover-point analysis.

3.2.2. Radio echo sounding

During gravimetry measurements of the VISA campaigns, between 2001 and 2005, the flying altitude had to be constant during the whole flight. Depending on the surface height along the flight track, the flight level was chosen between 3600 and 4800 m, a.s.l. which was mostly too high above ground to obtain usable ARA data. Therefore, the radio-echo-sounding system on-board the AWI research aircraft is used to get surface elevation information over large parts of DML. The RES uses a carrier frequency of 150 MHz and pulse lengths of 60 ns and 600 ns. The system is able to measure in ”toggle mode”, thus the pulse length is switched between 60 ns and 600 ns for a different vertical resolution (5 m, respectively 50 m). A measurement interval of 20 Hz at a ground speed of the aircraft of 240 km h^{-1} results in an along-track data point distance of 3.25 m, or rather 6.5 m for the individual pulse length (Steinhage and others, 1999). For more details about the RES system see Nixdorf and others (1999).

Analog to the ARA data, the RES data were processed using the kinematic GPS data recorded during the flight. Because of the different propagation velocities of electromagnetic waves in air, snow and ice, the onset of the snow surface is clearly visible as a first reflection in the radargram. The result of this investigations is the ”thickness” of the medium air, i.e. the flying altitude of the aircraft above the surface. Afterwards, the airborne kinematic GPS data and the altitude were synchronized using the operation time. The altitude is subtracted from the GPS heights to obtain the surface topography.

In Figure 3.8 the VISA flight lines are shown, but not for every line RES elevation data are available. The RES data were recorded in a pattern of parallel lines with a profile separation of 10 km, respectively 20 km. Flight lines crossing the parallel lines (tie lines) were flown to obtain crossover points for correction of magnetic and gravity data and can be used for determining the quality of the RES elevation measurements. To avoid elevation branches within the RES campaigns, the data were corrected with a block shift using these tie lines. This first correction was only a statistical approach and may not show

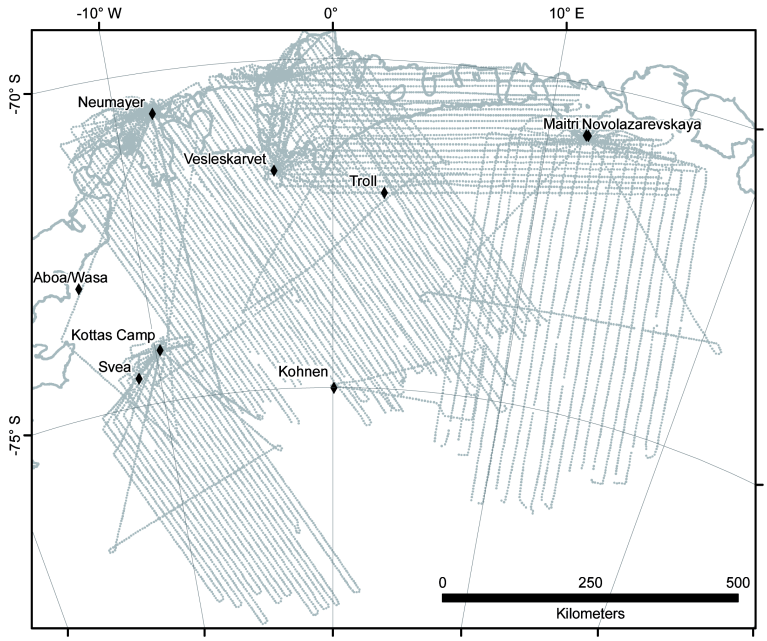

Figure 3.8.: Location of the VISA flight lines. The grounding and coast line, derived from MOA, are presented in bold grey lines (Haran and others, 2006). Stations and camps are marked with black rhombi.

the true surface elevations. This data set is provided by Sven Riedel. The accuracy of this data set is determined by a crossover-point analysis and results in an absolute mean elevation differences at crossover points (2σ corrected) of 2.25 m.

3.3. Ice, Cloud and land Elevation Satellite (ICESat)

The Ice, Cloud and land Elevation Satellite (ICESat) was launched in January 2003 for monitoring inter-annual and long-term changes in polar ice masses of the Greenland and Antarctic ice sheets among other objectives. The ICESat is part of NASA's Earth Observing System (EOS). Since February 20th, 2003 the Geoscience Laser Altimeter System (GLAS), on-board ICESat, provides a multiplicity of data worldwide. Altogether the GLAS offers 15 different data sets, which can be downloaded at the home-page of the National Snow and Ice Data Center (NSIDC - http://nsidc.org/data/icesat). The altimetry measurements are carried out with a near infrared laser (1064 nm) with a pulse repetition rate of 40 Hz. The laser illuminates a footprint of about 70 m at the Earth's surface and the along-track spacing of data points is about 170 m. The height of the surface topography is calculated from the mean of the elevation in-between the footprint and the coordinates (longitude and latitude) showing the center point of the illumination spot at the surface. Zwally and others (2002), Brenner and others (2003) and Schutz (2002) described the concept of GLAS in more detail.

In this investigation the ice sheet elevation data of the GLA12 release 28 data set were used (Zwally and others, 2007). At the time of writing 11 laser periods were available (Table 3.2).

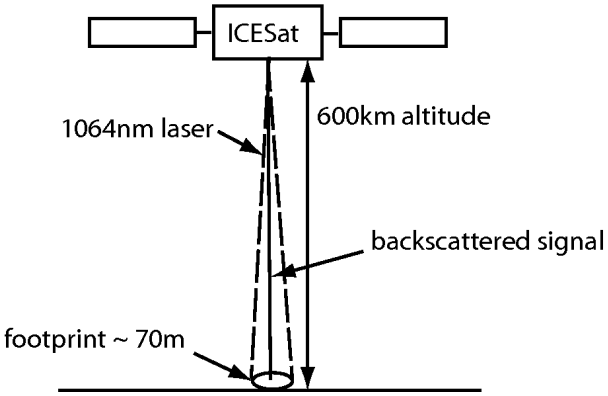

Figure 3.9.: A schematic illustration of the basic concept of ICESat laser altimetry.

Table 3.2.: Overview of the GLA12 release 28 laser measurement periods available at the time of writing.

Laser identifier	Days in operation	Start date	End date
1	38	2003-02-20	2003-03-29
2a	55	2003-09-24	2003-11-18
2b	34	2004-02-17	2004-03-21
3a	37	2004-10-03	2004-11-08
3b	36	2005-02-17	2005-03-24
3c	35	2005-05-20	2005-06-23
3d	35	2005-10-21	2005-11-24
3e	34	2006-02-22	2006-03-27
3f	33	2006-05-24	2006-06-26
3g	34	2006-10-25	2006-11-27
3h	34	2007-03-12	2007-04-14

For the final GLA12 data, the IDLreadGLAS tool offered by the NSIDC was used to convert the binary raw file to an ascii file. Afterwards, a simple shell script extracts all necessary information (longitude, latitude, elevation, time of measuring, ocean tide, ocean load tide and saturation correction factor). The saturation correction factor has to be applied to the elevation data, if the return energy is higher than predicted. The elevation error caused by detector saturation is shown in Fricker and others (2005). After adding the saturation correction factor to the elevation data, the ocean tide and ocean load tide correction (component of ocean tides, which is propagated a few kilometer inland on the grounded ice masses (Riedel, 2003)) is removed from the elevation data. Based on the laser shot time, the global tide model of TPXO7.1, recommended by King and Padmann (2005), was applied by using OTPS (http://www.coas.oregonstate.edu/research/po/research/tide/global.html), replacing the routinely

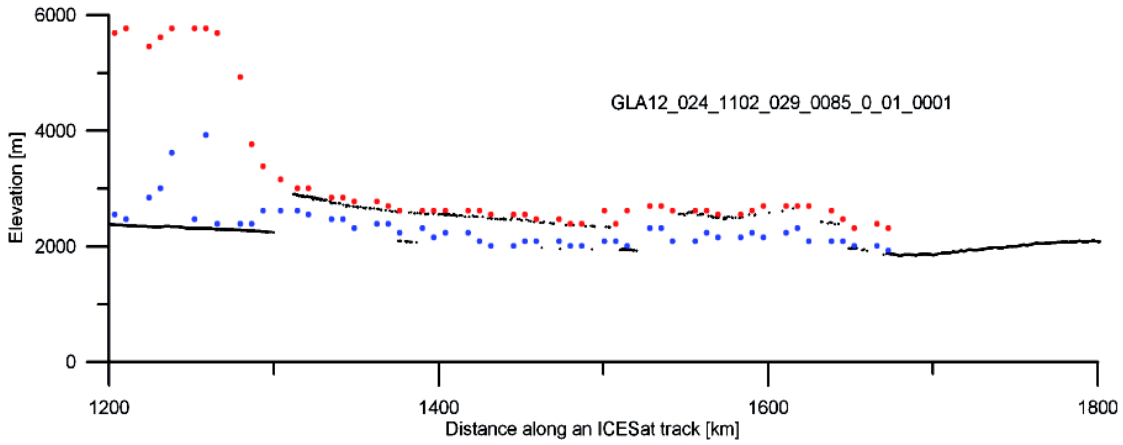

Figure 3.10.: A 2D-profile of a L2a GLA12 release 24 ground track. The black dots represent the elevation above the WGS84 ellipsoid, the red dots are the cloud top and the blue dots are the cloud bottom derived by simultaneous atmospheric measurements with the green laser (532 nm).

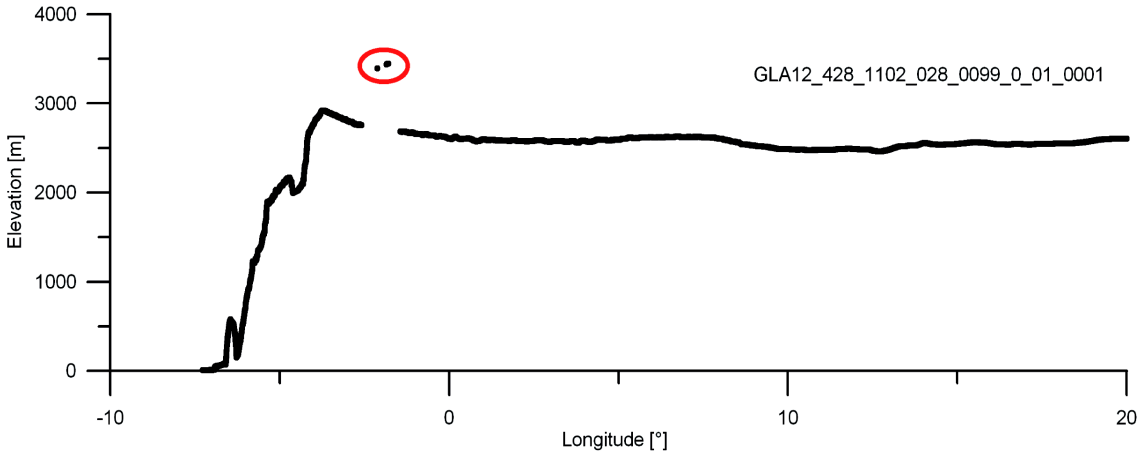

Figure 3.11.: A 2D profile of the Release28 ground track of GLA12. Plotted is the longitude against the elevation of the descending ground track. The red ellipse shows the effect of a cloud.

used tide correction which is based on a less accurate model for Antarctica. A serious error source of the ICESat altimetry data is clouds. The laser is able to penetrate optically thin clouds, but depending on the particle size and height of the cloud, the infrared laser (1064 nm) is reflected from the top of the near surface cloud (Figure 3.10). In release 28 of the GLA12 data, which was used for this investigation, nearly all clouds were removed by the NSIDC. The few remaining data points affected by clouds (Figure 3.11) can still distort interpolation of the GLA12 data. To avoid interpolation errors induced by residuals of clouds, such residuals were removed.

According to different landscapes, the GLA12 data were separated into three main areas: (i) The coastal region north of the (ii) mountain region and (iii) the plateau region. The smaller the area of investigation,

the more precise are statements on accuracies. For the estimation of the GLA12 accuracies, crossover-point analyses within the laser periods and for every single region were performed. The results can be seen in Table 3.3.

Table 3.3.: Absolute mean elevation differences at crossover points in meter of GLA12 data. Numbers in brackets are the counts of crossover points contributing the mean value. The mean presented in the last row is the mean of presented mean elevation differences of the laser periods.

Laser ID	Measurement period	Coastal	Mountainous	Plateau
L1	2003-02-20 to 2003-03-29	0.58 m (10270)	0.79 m (5780)	0.59 m (116006)
L2a	2003-09-24 to 2003-11-18	0.53 m (576)	0.80 m (278)	0.17 m (42310)
L2b	2004-02-17 to 2004-03-21	0.81 m (172)	0.99 m (97)	0.16 m (19837)
L3a	2004-10-03 to 2004-11-08	0.68 m (384)	0.79 m (179)	0.16 m (27999)
L3b	2005-02-17 to 2005-03-24	0.57 m (358)	0.92 m (148)	0.20 m (24312)
L3c	2005-05-20 to 2005-06-23	0.57 m (385)	0.83 m (144)	0.16 m (21518)
L3d	2005-10-21 to 2005-11-24	0.07 m (2935)	0.07 m (2132)	0.14 m (24288)
L3e	2006-02-22 to 2006-03-27	0.70 m (305)	0.65 m (154)	0.15 m (23738)
L3f	2006-05-25 to 2006-06-26	0.90 m (262)	1.18 m (91)	0.16 m (14054)
L3g	2006-10-25 to 2006-11-27	0.73 m (236)	0.84 m (161)	0.16 m (20342)
L3h	2007-03-12 to 2007-04-14	0.68 m (154)	0.82 m (72)	0.14 m (12732)
mean		**0.62 m**	**0.79 m**	**0.20 m**

Table 3.3 summarizes the elevation differences of the GLA12 measurements, which are varying with investigated area and laser period, but the predicted elevation accuracies of 0.15 m (Zwally and others, 2002) cannot be achieved. Only over the flat plateau region (mean slope of 0.16°), the accuracies are close to the predicted value. For the coastal region (mean slope 0.75°) and the mountainous region (mean slope 1°), the mean elevation differences are about three to four times higher. The standard deviations against the laser periods with regard to the three areas (Figure 3.12 A) and the slope (Figure 3.12 B) confirm this. The standard deviations of the crossover elevation differences is largest in the mountainous regions (except for L3e and L3h). The lowest standard deviation can always be found at the plateau, where the mean slope is also lowest. This can be confirmed by Figure 3.12 B, where standard deviations are lowest with slopes between 0 and 0.5°. With increasing slope, the standard deviation of crossover elevation differences also increases, but in a non-uniform way. Aside from this, it is very obvious that the laser periods are very different in accuracy and precision.

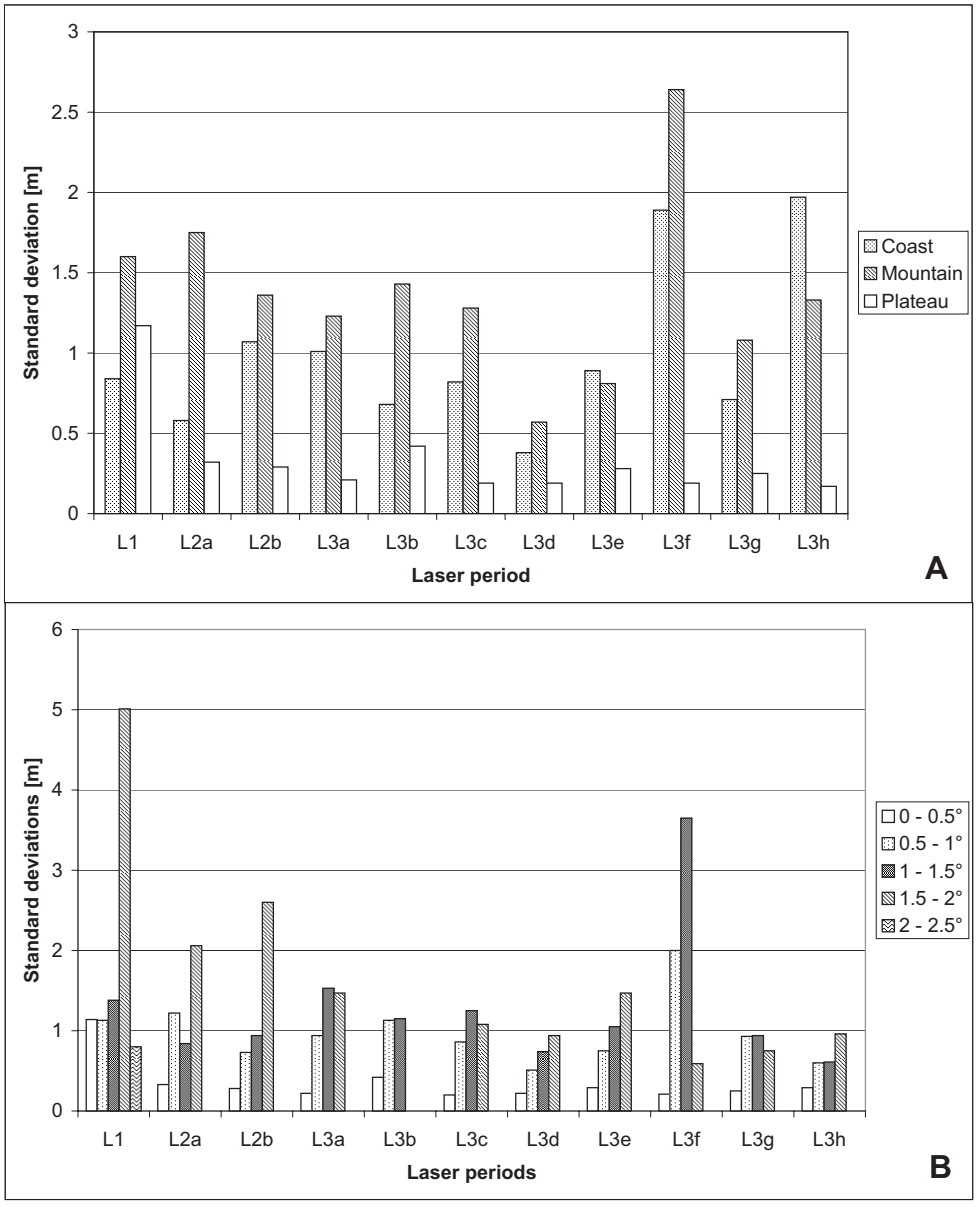

Figure 3.12.: Standard deviations against the elevation differences of GLA12 data at crossover point with regard to the three areas (A) and the different slopes (B).

4. Applications of the Data

In this chapter the applications of the above presented altimetry and GPS data are presented. The annual elevation change was calculated from the GLA12 data presented in Section 3.3. The two latest laser operation periods of the GLA12 data were combined with the airborne altimetry data (ARA and RES) and the ground-based kinematic GPS data to elevation data sets, which were used to generate an improved digital elevation model (DEM) for central Dronning Maud Land (DML). Based on this DEM, the ice divides in the area of investigation were re-located and static GPS data were used to determined a flow and strain field in the vicinity of the Kohnen station. In the following sections, these applications are described and results are presented.

4.1. Annual elevation change

Recent elevation-change studies of Antarctica (Wingham and others, 1998; Davis and Ferguson, 2004; Zwally and others, 2005; Helsen and others, 2008) are based on spaceborne radar-altimetry measurements. Wingham and others (1998) calculated the mean annual elevation change between 1992 and 1996 from ERS-1 and ERS-2 data. Davis and Ferguson (2004) present the mean annual elevation change from 1995 to 2000 from ERS-2 data. Both investigations have data gaps in the coastal regions and south of 81.5°S. Furthermore the firn compaction rate is neglected in both cases. Zwally and others (2005) and Helsen and others (2008) show the elevation changes derived from ERS-1/2 data as well, but pay attention to the firn compaction. These investigations show different elevation changes in DML. Zwally and others (2005) calculate increasing or very slightly decreasing elevation, whereas Helsen and others (2008) show an obvious decreasing elevation in the coastal region of DML and a slightly increasing at the plateau. This shows that firn correction is crucial for the determination of mass balance trends from altimetry and a different firn-correction techniques yield different elevation change results.

In this work, a first approach is presented to estimate the mean annual elevation changes in central DML from 2003 to 2007 based on laser-altimetry data from ICESat. For this purpose, crossover-point analyses between laser periods (Table 3.2) of an annual interval were performed (L1 minus L2b or L2a minus l3a, etc.). The annual interval is chosen to investigate always the same seasonal conditions. The elevation differences at crossover points were then interpolated to a 5 km $\times$ 5 km resolution grid to show annual elevation changes (chapter B, see appendix). Because of the small number of crossover

points containing data of the L1 laser period (about 10% of the other laser periods) L1 measurements were not used for further investigations. To calculate the mean annual elevation change and to minimize the relative errors of this estimation, a crossover-point analysis between L2a and L3h laser periods was made. The results were divided by the time span between the measurements (3.5 years) and interpolated on a 5 km $\times$ 5 km raster. In Figure 4.1 the annual elevation change derived from GLA12 altimetry data are shown. In addition, the standard deviation was calculated from the annual elevation changes presented in the appendix (Figure 4.2).

A few regions in the elevation change map are conspicuous due to elevation decreases at the plateau. Looking at the annual elevation change maps (in the appendix), it is obvious that these locations are characterized by very high elevation change estimations. The high standard deviations (over 10 m) in elevation changes point to measurement errors (e.g. the reflection of the laser signal on snow particles in the air during snow drift) of the GLA12 L2a data in these regions, thus the elevation changes in these areas are not correct.

Detailed information on measured elevation changes in the surrounding of the German Antarctic overwintering station (see section 1.1.1) are presented in Figure 4.3 and 4.4. Evidently, this area is divided into an increasing part, the Halvfarryggen, and a decreasing part, the Søråsen. The main wind direction in this region is from east to west (König-Langlo and others, 1998), hence air masses reach the Halvfarryggen first. Because of the peninsula character of the Halvfarryggen, it builds a barrier for air masses coming from the eastern ice shelf region. The body of humid air will snow first over Halvfarryggen. Because of the closed ice cover of the Ekströmisen, the air masses are not able to restore new humidity on their way westwards to the Søråsen. The mean elevation change for coastal DML is 0.06 ± 0.20 m (min:-1.06 m, max:0.72 m) and for the plateau of central DML -0.02 ± 0.10 m (min:-2.00 m, max:1.41 m). This results in a mass gain of 13.5 Gt a^{-1} at the coast and a mass loss of 19.3 Gt a^{-1} at the plateau (both values were determined with an assumed ice density of 910 kg m^{-3}). Because the laser is reflected at the surface and under the assumption that the firn compaction does not change with time, the firn compaction is neglected here, because the laser signal does not penetrate into the snow surface and thus changes in density do not affect the elevation change estimation. Nevertheless, the elevation accuracy of the GLA12 data at the plateau is 0.20 m, which is only slightly smaller than the elevation changes estimated for this region. The same is true for the coastal region. However, by calculating the mean annual elevation change from different time spans, a trend of the elevation change could be estimated.

An additional estimation of annual elevation change can be given by calculating the differences between the JLB97 DEM and the latest GLA12 data (L3h), to get the longest time span possible. The JLB97 DEM consists of ERS-1 radar altimetry data from the geodetic phase, which provided elevation data between April 1994 and May, 1995. The L3h data were derived between March 12th and April 14th, 2007. Thus, there is a time span of 12 years. The calculated elevation differences between these two data were divided by the time span, to obtain annual elevation change. Afterwards, the annual elevation change

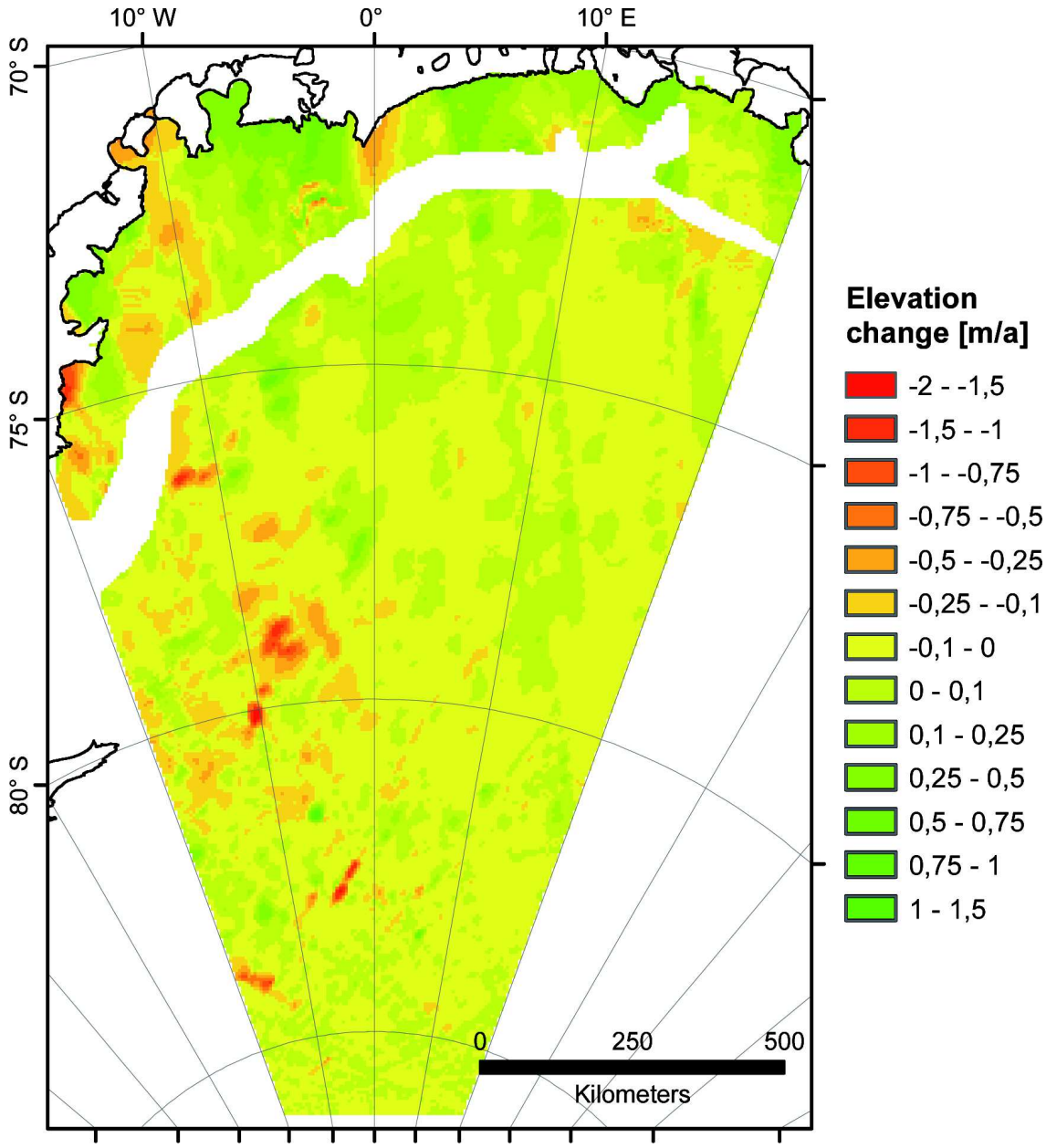

Figure 4.1.: The mean annual elevation change between 2003 and 2007 of the coastal region and the plateau of DML based on GLA12 L2a and L3h ICESat data. The black lines show the grounding line and coast line derived from MOA (Haran and others, 2006).

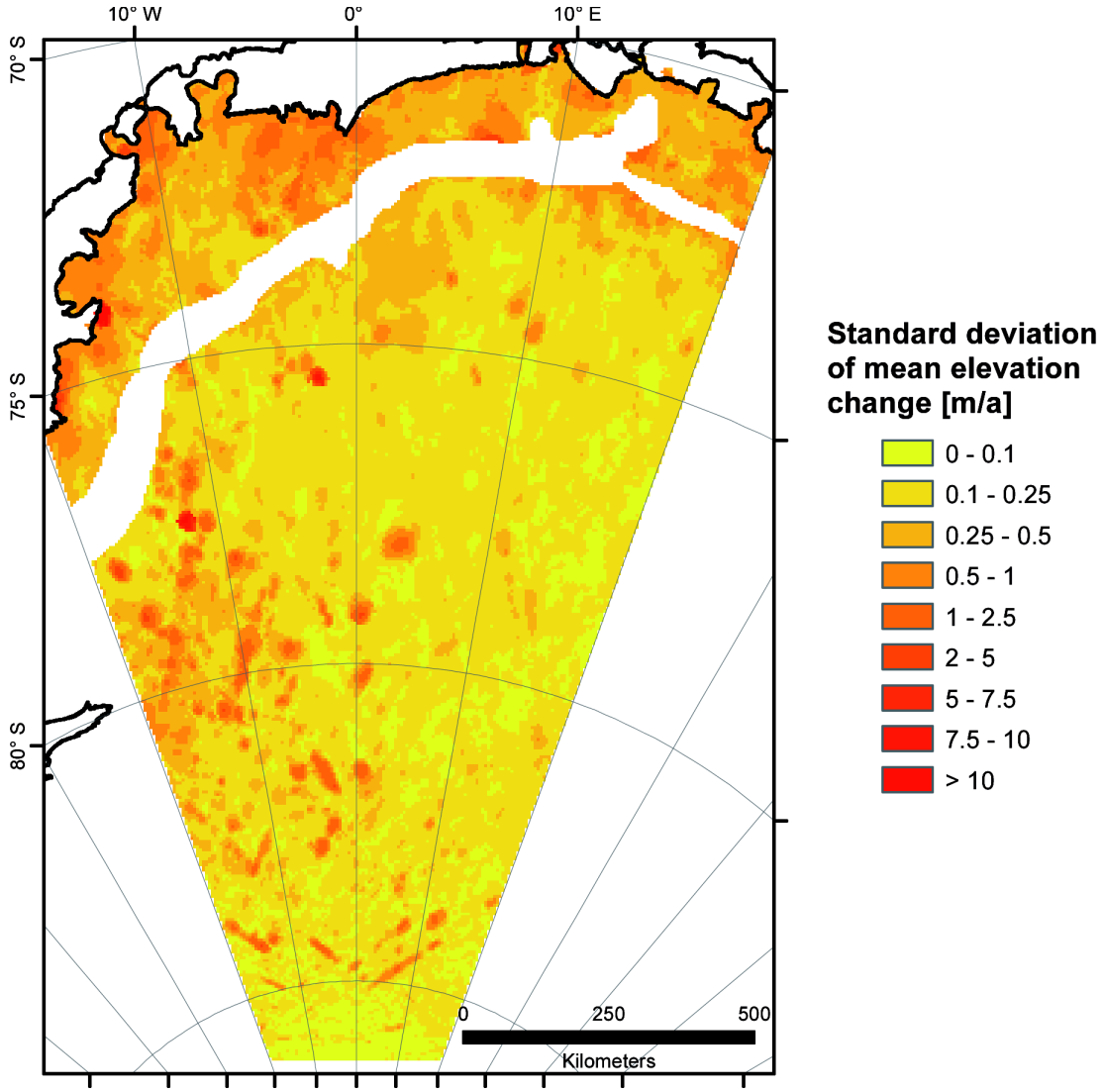

Figure 4.2.: The standard deviation of the mean annual elevation change of the coastal region and the plateau of DML based on GLA12 ICESat data. The black lines show the grounding line and coast line derived from MOA (Haran and others, 2006).

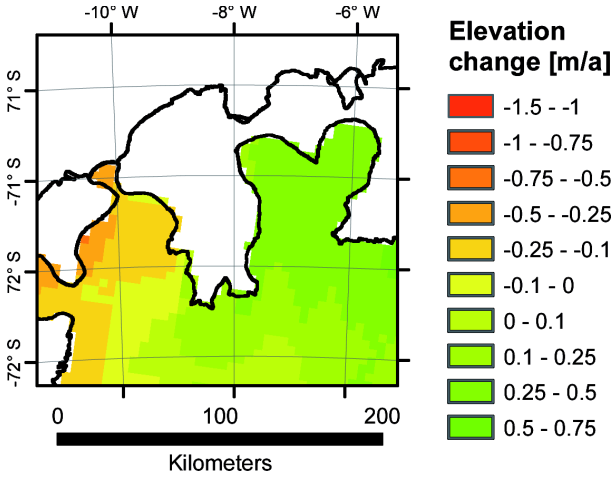

Figure 4.3.: The mean elevation change between 2003 and 2007 of the region surrounding the Ekströmisen ice shelf. The black lines show the grounding line and coast line derived from MOA (Haran and others, 2006).

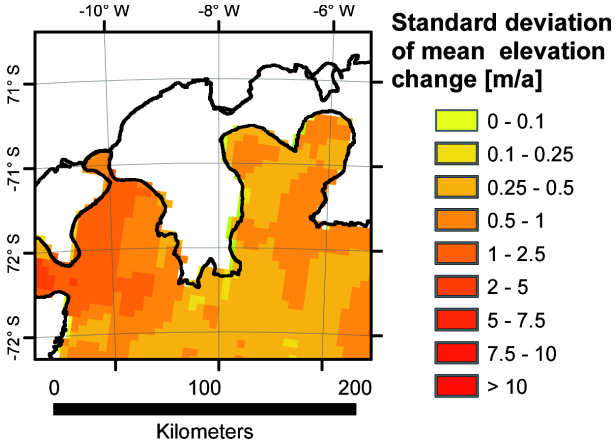

Figure 4.4.: The standard deviation of the mean annual elevation change of the region surrounding the Ekströmisen ice shelf. The black lines show the grounding line and coast line derived from MOA (Haran and others, 2006).

was interpolated to a 5 km × 5 km raster (Figure 4.5).

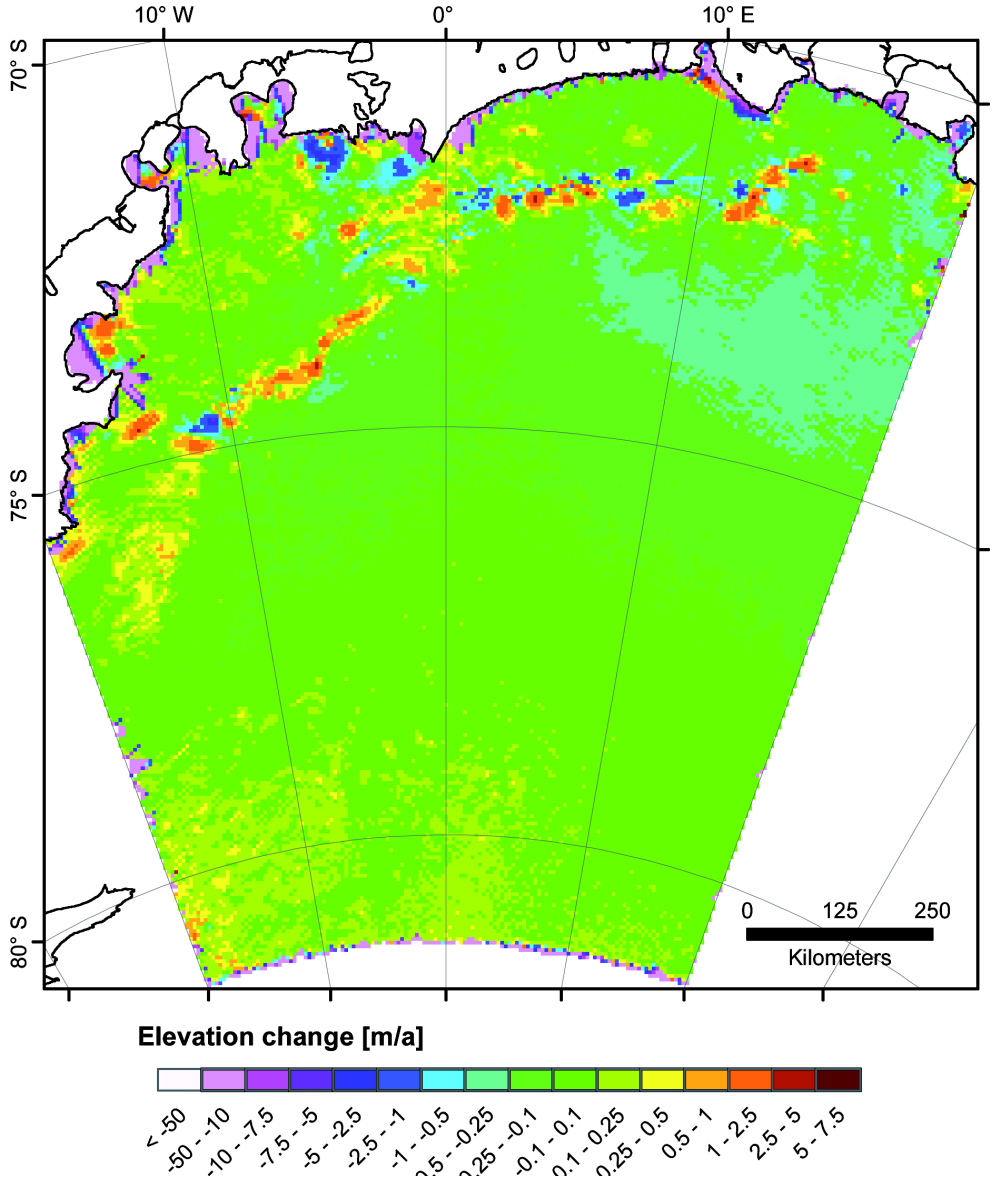

Figure 4.5.: Map of the annual elevation change, derived from the elevation differences between the JLB97 DEM and GLA12 L3h data. The elevation differences are gridded on a 5 km × 5 km raster.

At the plateau region, an obvious trend can be seen. In the north-eastern part shows a decreasing elevation trend of about -0.3 m per year. Further south, the decrease is weakened until in the south-western region of the plateau an increasing elevation of about 0.3 m per year is noticed. Above all, high elevation declines (below -20 m per year) can be seen in the grounding zone, which may be caused by the slope-induced error, which degrade the JLB97 DEM in this region. Neglecting the decreasing elevation below -20 m per year, the mean elevation decrease at the coast is -0.57 m per year and increase is 0.05 m per year at the plateau. Comparing the two approaches of elevation-change estimates

presented here, the mean difference in elevation change is -0.03 m per year at the plateau and -2.06 m per year in the coastal region. This shows that the two approaches are comparable at the plateau, but in the coastal region the elevation differences between JLB97 and GLA12 data are too high to estimate reliable elevation changes per year.

The investigation is only made with the JLB97 DEM, because the exact time of recording the RAMP data is not known.

4.2. Generating a DEM

The final DEM consists of four different data sets. Due to the high accuracy of the ground-based kinematic GPS data, these were assumed to represent the true surface elevations. The area of investigation was divided into three regions (coastal, mountainous, plateau) to investigate their specific accuracies and error sources. The parts of the area of investigation were chosen with a small overlapping area to alleviate the mosaicing process at the end. To get elevations of 2007 when the latest GPS data were recorded, the annual elevation change presented in section 4.1 has to be taken into account. The traverse profile (recorded in December 2005) was shifted by 0.02 m in coastal region and 0.04 m at the plateau and the investigations around Kohnen station (recorded in January and February 2001) were shifted by 0.2 m.

Because the ARA elevation data are unaffected by the weather conditions, e.g. ground fog or near surface snow drift, like GLA12 elevations, these data were used to enlarge the number of crossover points between the ground-based GPS and GLA12. Therefore, the mean penetration depth of the radar signal was calculated by crossover-point analyses between the ground-based kinematic GPS and ARA profiles. The search radius of crossover points was arbitrarily chosen to be 10 m around the ARA data point and yield mean penetration depths of 2.25 m at the plateau. At the coast, the derived penetration depth is 2.28 m. These values were used to shift the ARA data to the highly accurate GPS elevations. By shifting the ARA data to the ground-based GPS, the ARA elevations represent also elevations of 2007.

Only the latest GLA12 laser operation periods (L3g and L3h) recorded shortly before and after the GPS data at the coast, were used. In Table 3.3 the absolute mean difference of these two laser periods are given. The mean absolute elevation difference at the plateau is very good (0.15 m), 0.83 m in the mountainous and 0.70 m coastal region. Crossover point analyses between GPS and GLA12 and corrected ARA and GLA12 result in elevation differences at crossover points below the data set accuracies. Therefore, it is renounced to level the GLA12 data.

The elevation differences between GPS and RES and the corrected ARA, respectively, were also determined by crossover-point analyses. Due to the lower frequency of the RES (150 MHz), the signal penetration depth is larger than for the ARA (4.3 GHz) signal (Rott and others, 1993). The analyses

result in mean penetration depths of 24.02 m (plateau), 25.35 m (mountain range) and 21.97 m (coastal region). These values were also used to shift the RES data to the other data sets.

After adjusting, all elevation data sets were merged to three data sets: one for the plateau, one for the coastal region and one for the mountainous region. With the aid of the ”Geostatistical Analyst” of ArcGIS9.2 the geostatistical interpolation method ”Ordinary Kriging” was used, to obtain three DEMs from the three data sets. The mosaicing of the three single DEMs completed the generation of the final DEM with a 2.5 km $\times$ 2.5 km resolution (Figure 4.6). To get a smooth transition in the overlapping areas during mosaicing process, a blend of the bordering DEMs is used.

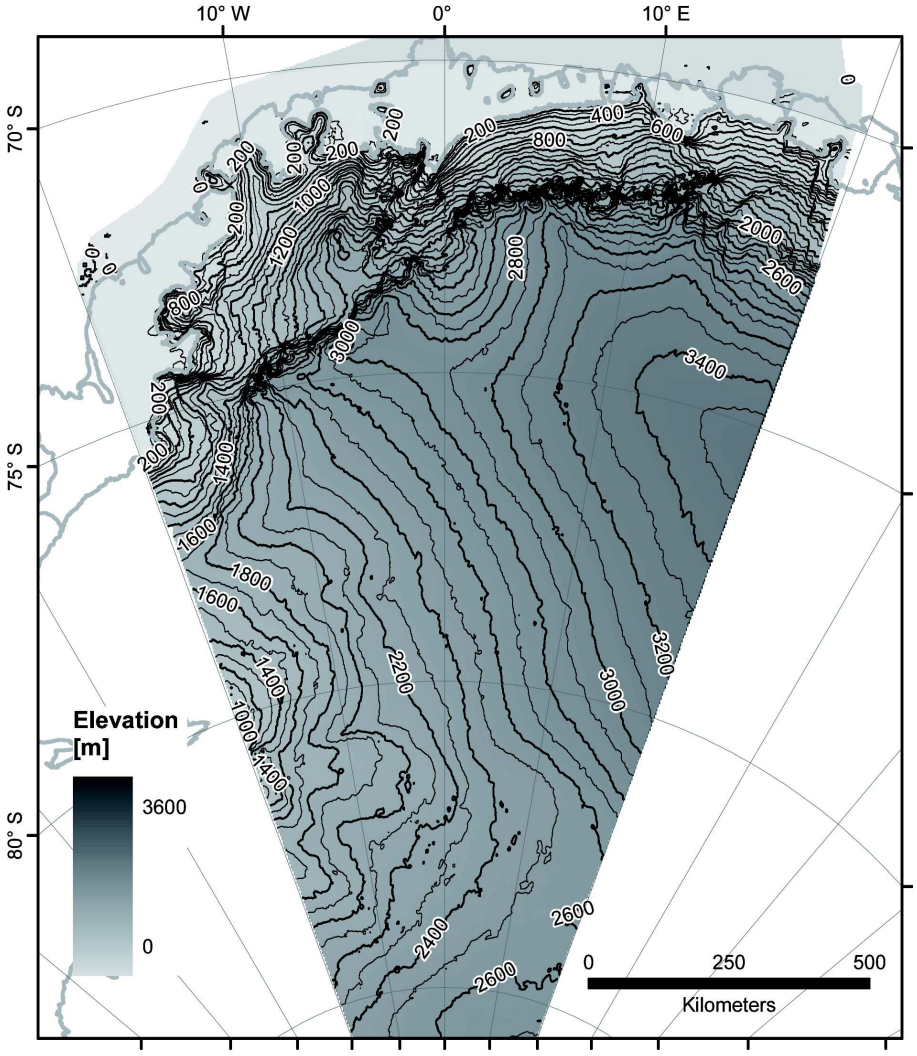

Figure 4.6.: The improved DEM of central DML. The grey line represents the grounding line and coast line derived from MOA (Haran and others, 2006)

The accuracy of the DEM is estimated by the elevation differences between the ground-based kinematic GPS data, processed with local reference stations, and the final DEM grid. For this purpose, the GPS heights within a 2.5 km $\times$ 2.5 km raster cell are averaged to observe the differences at the same scale.

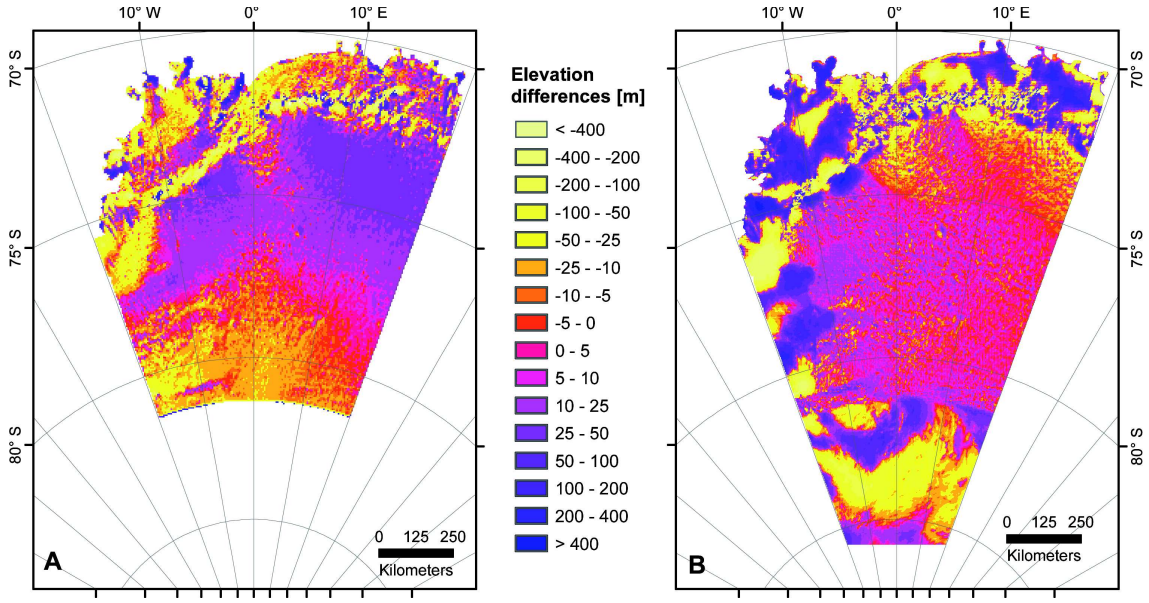

Figure 4.7.: A comparison of the new DEM with JLB97 (A) and the new DEM with RAMP (B). The black lines are showing the grounding and coast line derived from MOA (Haran and others, 2006).

Another investigation was the standard deviation of the GPS heights within a raster cell. In the coastal region, the height of the leaf like profiles on Halvfarryggen and Søråsen were compared with the raster values of the final DEM. On the plateau, the ground-based kinematic GPS profiles in the vicinity of the EDML deep-drilling site were used. In Table 4.1 the results are shown and a detailed description is given in Wesche and others (in review). Because of the insufficient comparative values, the mountainous region is neglected in this investigation.

Table 4.1.: The accuracy of the improved DEM determined by height comparison with highly accurate ground-based GPS data.

Region	Mean difference [m]	Standard deviation [m]	Minimum [m]	Maximum [m]
Coast	-2.66	4.45	-33.49	58.29
Plateau	-0.65	0.26	-1.77	0.11

A comparison of the new generated with the currently available DEMs presented in section 1.2 was done by subtracting the JLB97 or RAMP DEM from the new DEM presented here. The results are shown in Figure 4.7 A and B.

The elevation differences on the plateau north of 81.5°S are small in comparison to the coastal or mountainous region. However, both commonly used DEMs consist of ERS-1 altimetry data in this region, but in the north-eastern part, the elevation differences between the improved DEM and JLB97 are larger than between the improved DEM and RAMP. South of 81.5°S and in the coastal region the RAMP DEM

consists of ADD data (Liu and others, 1999, 2001). There are larger positive and negative heights than determined in the improved DEM. In the JLB97 DEM, the variations in lower and higher surface elevation than the improved DEM are not as large. For more details see Wesche and others (in review).

4.3. Re-location of the ice divides

Ice divides, i.e. ice ridges separating catchment areas, are next to the domes preferred drilling locations, because the interpretation of paleoclimatic records is simplified by the known origin of the ice (Paterson, 1994). In DML several ice divides are known from former investigations using the DEM of Bamber and Huybrechts (1996). One distinguishes between two types of ice divides: (i) symmetric or topographic ice divide and (ii) asymmetric or flow ice divide. The topographic ice divide can be determined by the surface topography and is located at the highest surface elevation along a cross section of the DEM, while the asymmetric ice divide is not necessarily at the highest surface elevation. The ice flow near the topographic ice divide is characterized by a slow flow parallel to the course of the ice divide in-between a buffer of three to five times the ice thickness around the ice divide (Raymond, 1983; van der Veen, 1999). Apart from this region, the flow velocity becomes faster and more divergent to the course of the ice divide. The flow ice divide is characterized by a divergent flow at the border of two adjoined catchment areas. This type of ice divide is not necessarily at the top of the surface topography (Paterson, 1994). The focus of this work lies on the topographic ice divides. ArcGIS offers several investigation methods, which help to obtain the location of the ice divides in DML. Based on the calculated aspect of the surface topography in DML, the inclination of the slopes is illustrated (see appendix, Figure C.2). The aspect of the topography was mainly used for the localization of the ice divides. Additionally, the theoretical ice flow direction and the catchment basins were determined also with the ArcGISToolBox. The result is a new map of ice divides in central DML (Figure 4.8). In most regions the course of the ice divide is only a few kilometers away from the ones derived from the DEM of Bamber and Bindschadler (1997). Due to the higher resolution of the improved DEM, it was possible to derive new ice divides, e.g. at the coast on Halvfarryggen and Kapp Norvegia (see Figure 4.8). The course of the ice divide in the east of the region of interest could not be confirmed, but a completely new one at $\sim$12°E was identified. Two ice divides end at the mountain range, their course through the mountains could not be reliably identified.
The biggest outlet glacier in central DML is the Jutulstraumen. The outlet glacier is fed by ice masses flowing from the plateau through a deep valley glacier between Kirwanveggen and Mühlig-Hofmann Gebirge. The Jutulstraumen flows to the north into the Fimbulisen ice shelf. Another big outlet glacier is the Veststraumen, which is fed by ice masses flowing from the Heimefrontfjiella to the north-west and ice masses from the Ritscherflya flowing to the west. The Veststraumen drains to the west into the Riiser-Larsen ice shelf. There are some smaller catchment areas between the Jutulstraumen and the Veststraumen. They are all draining to the north into small ice shelves. The southern part of central

DML is draining to the south-west and the western part to the north. Of particular interest is the change of the ice divide location in the vicinity of the EDML deep-drilling site (see small map in Figure 4.8). This ice divide is forking in the east of EDML. The southern ice divide based on the DEM is about 12 km north compared to the one determined with JLB97. The location of the northern ice divide is nearly unchanged. That means EDML lies directly within two ice divides, only 3 km (southern ice divide) and 4 km (northern ice divide) apart from the location of the ice divides. A more detailed investigation of the ice divides around EDML is given in Wesche and others (in review).

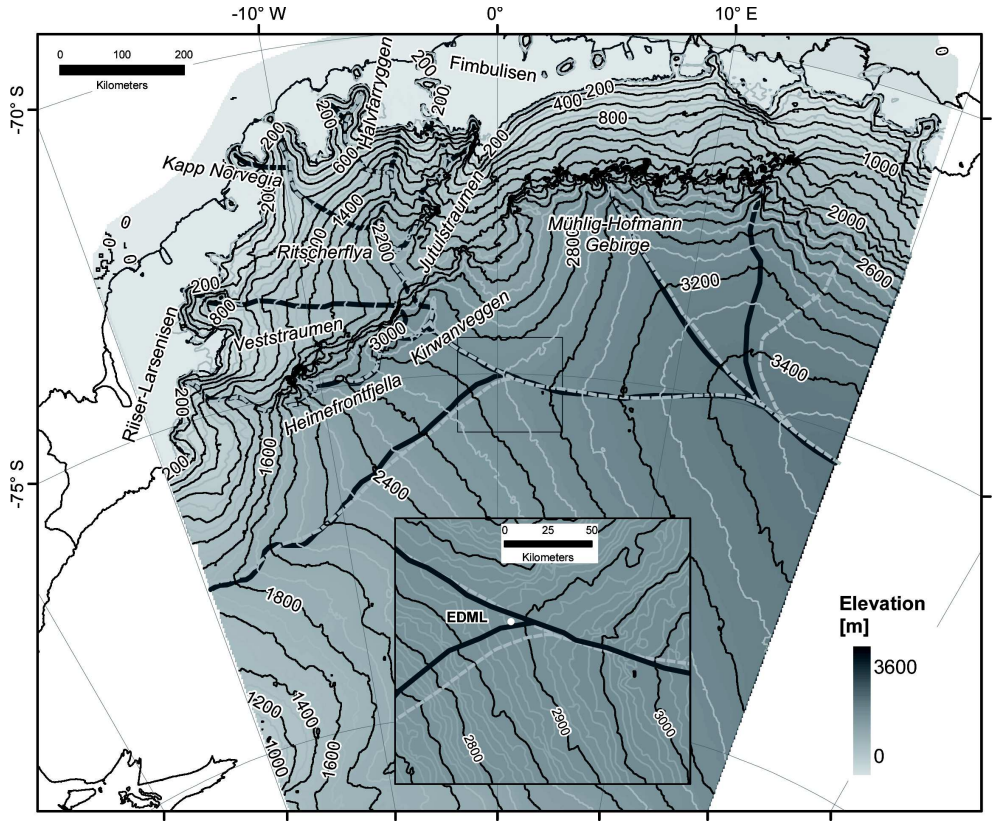

Figure 4.8.: A map showing the courses of the ice divides in DML. The dark grey lines show the ice divides derived from the new DEM and for comparison, the light grey dashed line the ice divides derived from JLB97. The contour lines are from the new DEM, the black lines representing a contour interval of 200 m and the grey 100 m. The black lines are showing the grounding and coast line derived from MOA (Haran and others, 2006). In the inset map, the region around the EDML drilling site (white dot) is shown. The contour lines intervals are 10 m (grey) and 50 m (black).

4.4. Determining ice flow and strain rates

The ice flow in central DML is calculated from 18 static GPS measurements. The mean annual surface velocity is calculated by averaging the flow velocities of different time periods. The results are shown

in Table 4.2. The accuracy of the velocity measurements is calculated by the propagation of errors and has a maximum of 0.06 m a^{-1}. A detailed description of the calculation of the precision of the velocity is given in Wesche and others (2007).

Table 4.2.: The flow velocities of various point measurements on the Antarctic plateau.

Name	Longitude	Latitude	Flow [m a^{-1}]	Flow direction [°]	Period of averaging
DML01	2.5493° E	74.8564° S	0.54	293.2	Jan. 1997 - Jan. 1999
DML02	3.9185° E	74.9683° S	3.18	153.5	Jan. 1997 - Jan. 1999
DML03	1.9609° E	74.4995° S	7.40	128.9	Jan. 1997 - Jan. 1999
DML05	0.0072° E	75.0024° S	0.66	270.4	Jan. 2001 - Dec. 2005
DML07	3.4306° W	75.5816° S	4.28	229.6	Jan. 1997 - Jan. 2001
DML19	0.9951° W	75.1674° S	1.87	213.3	Jan. 1999 - Jan. 2001
DML25	0.0818° E	75.0060° S	0.83	274.2	Jan. 2004 - Dec. 2005
DML26	0.0099° E	74.8393° S	1.07	335.9	Jan. 2001 - Dec. 2005
DML27	0.7040° E	75.0560° S	0.96	287.5	Feb. 2003 - Dec. 2005
BA01	0.0678° E	75.0017° S	0.68	272.6	Jan. 2003 - Dec. 2005
HM01	0.0078° E	74.9939° S	0.64	273.7	Jan. 2000 - Dec. 2005
HM02	0.0394° E	75.0069° S	0.68	270.0	Jan. 2000 - Dec. 2005
HM03	0.0229° W	75.0074° S	0.67	266.6	Jan. 2000 - Dec. 2005
PEN1	0.0819° E	74.9654° S	0.64	291.3	Jan. 2000 - Dec. 2005
PEN2	0.2296° E	74.9945° S	0.77	282.9	Jan. 2000 - Dec. 2005
PEN3	0.1728° E	75.0393° S	0.86	265.9	Jan. 2000 - Dec. 2005
PEN4	0.0121° W	75.0388° S	0.84	257.9	Jan. 2000 - Dec. 2005
PEN5	0.0659° W	74.9937° S	0.62	269.8	Jan. 2000 - Dec. 2005

Strain is a dimensionless parameter of deformation and the strain rate is a time dependent deformation of a material. Deformation is caused by stresses acting on e.g. ice masses (Paterson, 1994). The flow of ice masses causes such stresses and therefore the surface velocities calculated from static GPS measurements were used for the determination of the strain rates. Of particular interest is the deformation rate around the EDML deep-drilling site. Therefore, five aluminium stakes (PEN1-5) in shape of a pentagon network around the drilling site were fixed in the snow surface in January 2000. Since then, the stakes were observed in several austral summer campaigns. Simultaneously, a sixth aluminium stake in the center of the pentagon was observed (BA01). The strain field is shown in Figure 4.9 and a detailed description is given in Wesche and others (2007) (Paper I).

Because the center point of the pentagon-shaped network is only 93 m north-east to the drilling location of the EDML ice core, the determined weighted mean strain rates ($\dot{\varepsilon}_x = -1.54 \times 10^{-5}\, a^{-1}$ - strain rate in north direction, $\dot{\varepsilon}_y = -5.64 \times 10^{-5}\, a^{-1}$ - strain rate in east direction and $\dot{\varepsilon}_z = 1.09 \times 10^{-4}\, a^{-1}$ - vertical

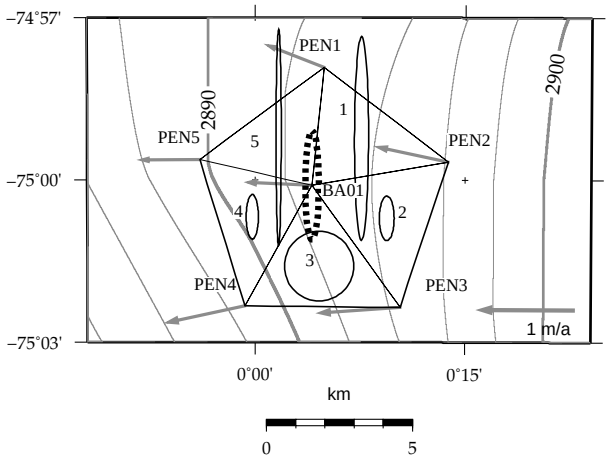

Figure 4.9.: The strain field and velocity vectors around the EDML deep-drilling site taken from Wesche and others (2007). The thin black ellipses are the strain ellipses for the strain triangles 1-5. The dotted ellipse represents the weighted mean strain rates for BA01, which is 93 m north-east of Kohnen station.

strain rate) are representative for the strain rates for the ice core. The results show layer thinning in the EDML ice core, which has to be taken into account for yielding a correct interpretation of the ice-core data.

5. Summary and Outlook

The evaluation of annual elevation changes between 2003 and 2007, derived from crossover-point analyses between different laser periods of the GLA12 is a first approach for estimating annual changes of the elevation. By calculating the mean annual elevation change from seven different time spans, a trend could be determined. However, the GLA12 accuracy is only slightly below the elevation changes and therefore it is necessary to use longer time spans to minimize the relative errors of elevation change determination. Nevertheless, the preliminary estimation of annual elevation change shows interesting results. In coastal DML, the mean elevation change is positive with 0.06 m with a standard deviation of 0.20 m. Looking at the area of the Ekströmisen, one can see that the elevation change varies over this small area. The Halvfarryggen near the Neumayer station shows an increasing surface elevation, while the Søråsen, located in the west of the Halvfarryggen, shows decreasing elevations. Because the main wind direction in the coastal region near Neumayer station is east, the Halvfarryggen can be seen as a barrier for humid air masses. On the plateau, the mean annual elevation change is negative by -0.02 m ± 0.10 m, which is contrary to the investigations of Zwally and others (2005) and Helsen and others (2008). The trend analysis of mean annual elevation change results in a mass loss for the plateau region of -19.3 Gt a^{-1} and a mass gain of 13.5 Gt a^{-1} for the coastal region.

Other elevation change investigations are predicting an increasing elevation on the plateau and a contrary evolution at the coast. Similar results are obtained by investigating JLB97 and GLA12 L3h data, but the values of elevation change are nearly the same for the plateau region. However, the mean annual elevation change in the coastal region is dependent on the elevation accuracy of the JLB97 DEM. Firn compaction is also a factor of high uncertainty in the calculation of elevation change using radar altimetry as shown in the different results of Zwally and others (2005) and Helsen and others (2008). Therefore, the comparison of two different altimetry data sets in terms of calculating the annual elevation change is limited. In regions with relatively constant firn compaction and thus penetration of the radar signal the results are very good, but in highly variable regions, the annual elevation change should be calculated with identical sensors.

The improved DEM for central DML presented in this work was derived from a combination of ground-based kinematic GPS, two types of airborne radar altimetry, and spaceborne laser altimetry. To achieve the best possible data accuracy and density, the different elevation data were compared to each other, corrected and combined. Because the ground-based kinematic GPS data are not affected by clouds

(as laser altimetry) or signal penetration into the snow surface (as radar altimetry) and their high vertical accuracy of 0.03 m, these heights are used as a reference elevation for the remotely sensed altimetry data.

With regard to the very different surface topography and to obtain a good interpolation result, the area of investigation was divided into three parts: (i) the coastal region north of the mountain range with its varying topography, (ii) the mountain range with the steep slopes and outcrops, and (iii) the plateau with its wide flat topography. Based on several crossover-point analyses, the remotely sensed elevation data were investigated with regard to the elevation differences to the ground-based kinematic GPS elevations. Because the ground-based data are spatially limited, the ARA data were used to enlarge the number of crossover points to the other altimetry data. The ARA data were leveled to the GPS data by the mean penetration depth. Afterwards, the GLA12 elevation data were investigated with regard to the height differences to the GPS and ARA data. These differences are below the accuracy of the data set and thus, the GLA12 data do not need to be shifted to the other data. The RES signal has a higher penetration depth than the ARA, therefore a crossover-point analysis between the ARA profiles and the RES data was performed. The obtained elevation differences were used to shift the RES data to the ARA data. After leveling the remotely sensed data to the ground-based GPS data, the data were merged into elevation data sets for the coastal, mountainous and plateau region. The geostatistical interpolation technique "Ordinary Kriging" was used to interpolate the heights to a 2.5 km $\times$ 2.5 km raster for the three investigation areas. Afterwards, a mosaic of the three separated DEMs was generated. The accuracy of the improved DEM is checked by the elevation differences between the ground-based GPS profiles and the DEM grid. The mean elevation differences are -0.65 m at the plateau and -2.66 m in the coastal region. The accuracy of this DEM could be further improved by using more ground-based kinematic GPS data which should be equally distributed over the whole area of investigation. Especially in the coastal region, where the penetration depth of the radar signal varies, ground-based measurement are needed to estimate such variations and to improve the radar altimeter data. But the advancement in accuracy of this DEM compared to the commonly used DEMs is obvious, due to use of highly accurate ground-based kinematic GPS data (even if they are spatially limited) contributing significantly to the quality of the DEM.

Elevation difference estimations between the new DEM presented here and the DEMs commonly used for modeling, JLB97 and RAMP, show very high spatial variations. On the plateau north of 81.5°S, the elevation differences are within a few meters. North of this region, the elevation differences are increasing very fast up to several hundred meters. Especially in the coastal region, where the elevation of large parts was underestimated in earlier DEMs, the improved DEM is a definite advance for numerical modeling of ice dynamic and mass balance.

Because the new DEM has a higher resolution, the location of ice divides can be determined more accurately. The location of the ice divides in DML has been calculated from investigations based on the

DEM of Bamber and Huybrechts (1996). A comparison between the improved and the old ice divides shows variations mostly within very few kilometers. In the coastal region, the courses of old the ice divides are complemented by some new ice divides. Altogether, only small changes in the courses of the ice divides were found. Nevertheless, the knowledge of the ice-divide locations in the area of investigation is improved by the new DEM.

As presented in Wesche and others (2007), static GPS measurements were not only used for local reference stations, but also for the calculation of surface velocities. These velocities were used to determine the strain field in the surrounding of the EDML deep-drilling site, which has to be accounted for to yield a correct interpretation of ice-core data. During the International Partnerships on Ice Core Science (IPICS) pre-site survey in the beginning of 2007, four pentagon-shaped deformation figures were established around possible coastal drilling sites. These deformation figures will be re-surveyed during the next austral summer campaign in Antarctica. The new positions will be used to determine surface strain fields around these possible drilling sites. In addition to the accurate DEM presented here, ground penetrating radar measurements and shallow ice and firn cores, as well as the deformation studies will give an advice to select a suitable drilling site for a deep coastal ice core.

With the launch of the CryoSat-2, planned for November 2009, a new era of satellite radar altimetry over ice sheets will begin. The onboard Synthetic-Apertur Interferometric Radaraltimeter (SIRAL) is specially designed for the measurement above ice sheets. Due to the small footprint of 250 m (16 - 20 km ERS - http://earth.esa.int/object/index.cfm?fobjectid=3999), the elevation radar-altimeter measurements of elevation will be improved. The footprint of the GLAS on board the ICESat is even smaller (70 m), but the laser is not able to penetrate clouds. The independence from weather conditions and the (for a spaceborne radar altimeter) small footprint are the big advantages of the CryoSat-2. However, the SIRAL will also be affected by the slope-induced error and the penetration of the radar signal into the snow surface. Therefore, it will be essential to validate the CryoSat-2 altimetry data with ground-based measurements. This improved DEM provides a suitable data set to validate the CryoSat-2 altimetry products.

Bibliography

Alley, R. B., P. U. Clark, P. Huybrechts and I. Joughin, 2005. Ice-sheet and sea level changes, *Science*, **310**, 456–460.

Alley, R. B., M. K. Spencer and S. Anandakrishnan, 2007. Ice-sheet mass balance: assessment, attribution and prognosis, *Annals of Glaciology*, **46**, 1–7.

Arthern, R. J. and R. C. A. Hindmarsch, 2006. Determining the contribution of Antarctica to sea-level rise using data assimilation methods, *Royal Society of London Transactions Series A*, **364**(1844), 1841–1865.

Bamber, J. L. and R. A. Bindschadler, 1997. An improved elevation dataset for climate and ice-sheet modelling: validation with satellite imagery, *Annals of Glaciology*, **25**, 439–444.

Bamber, J. L. and J. L. Gomez-Dans, 2005. The accuracy of digital elevation models of the Antarctic continent, *Earth and Planetary Science Letters*, **237**, 516–523.

Bamber, J. L. and P. Huybrechts, 1996. Geometric boundary conditions for modelling the velocity field of the Antarctic ice sheet, *Annals of Glaciology*, **23**, 364–373.

Brenner, A. C., R. A. Bindschadler, R. H. Thomas and H. J. Zwally, 1983. Slope-induced errors in radar altimetry over continental ice sheets, *Journal of Geophysical Research*, **88**(C3), 1617–1623.

Brenner, A. C., H. J. Zwally, C. R. Bentley, B. M. Csatho, D. J. Harding, M. A. Hofton, J.-B. Minster, A. Roberts, Saba J. L., R. H. Thomas and D. Yi, 2003. Derivation of range and range distribution from laser pulse waveform analysis for surface elevations, roughness, slope, and vegetation heights, *GLAS Algorithm Theoretical Basis Document Version 4.1*, **Greenbelt, MD**, Goddard Space Flight Center.

van den Broeke, M., W. J. van de Berg and E. van Meijgaard, 2006. Snowfall in coastal West Antarctica much greater than previously assumed, *Geophysical Research Letters*, **33**(L02505), 1–4.

Davis, C. H. and A. C. Ferguson, 2004. Elevation Change of the Antarctic Ice Sheet, 1995-2000, From ERS-2 Satellite Radar Altimetry, *IEEE Transactions on Geoscience and Remote Sensing*, **42**(11), 2437–2445.

Drews, R., W. Rack, C. Wesche and V. Helm, accepted. A spatially adjusted elevation model in Dronning Maud Land, Antarctica, based on differential SAR Interferometry, *IEEE Transactions on Geoschience and Remote Sensing*.

EPICA Community Members, 2006. One-to-one coupling of glacial climate variability in Greenland and Antarctica, *Nature*, **444**(7116), 195–198.

Fricker, H. A., A. Borsa, B. Minster, C. Carabajal, K. Quinn and B. Bills, 2005. Assessment of ICESat performance at the salar de Uyuni, Bolivia, *Geophysical Research Letters*, **32**(L21S06).

Haran, T., J. Bohland, T. Scambos, T. Painter and M. Fahnestock, 2006. MODIS mosaic of Antarctica (MOA) image map, *Boulder, Colorado*, **National Snow and Ice Data Center**, Digital media.

Helsen, M. M., M. R. van den Broeke, R. S. W. van de Wal, W. J. van de Berg, E. van Meijgaard, C. H. Davis, Y. Li and I. Goodwin, 2008. Elevation changes in Antarctica mainly determined by accumulation variability, *Science*, **320**, 1626–1629.

Hofmann-Wellenhof, B., H. Lichtenegger and E. Wasle, 2008. GNSS - Global Navigations Satellite System: GPS, GLONASS, Galileo & more, Springer Wien New York.

Honeywell AA-300 Manual, 1998. System description and installation manual - AA-300 Radion Altimeter System.

Huybrechts, P., 2003. Antarctica: modelling, In: Mass Balance of the Cryosphere: Observations and Modeling of Contemporary and Furture Changes, eds. Bamber. J. L. and A. J. Payne, Cambrigde University Press, chap. 13, 491–524.

Huybrechts, P., D. Steinhage, F. Wilhelms and J. Bamber, 2000. Balance velocities and measured properties of the Antarctic ice sheet from a new compilation of gridded data for modeling, *Annals of Glaciology*, **30**, 52–60.

Intergovernmental Panel on Climate Change (IPCC), 2007. Climate Change 2007: Synthesis Report.

King, M., 2004. Rigorous GPS data-processing strategies for glaciological applications, *Journal of Glaciology*, **50**(171), 601–607.

King, M. and L. Padmann, 2005. Accuracy assessment of ocean tide models around Antarctica, *Geophysical Research Letters*, **32**(L23608).

König-Langlo, G., J. C. King and P. Pettre, 1998. Climatology of the three coastal Antarctic stations Dumont d'Urville, Neumayer, and Halley, *Journal of Geophysical Research*, **103**(D9), 10935–10946.

Krinner, G., O. Magand, I. Simmonds, C. Genthon and J.-L. Dufresne, 2007. Simulated Antarctic precipitation and surface mass balance at the end of the twentieth and twenty-first centuries, *Climate Dynamics*, **28**, 215–230.

Legresy, B. and F. Remy, 1998. Using the temporal variability of satellite radar altimetric observations to map surface properties of the Antarctic ice sheet, *Journal of Glaciology*, **44**(147), 197–206.

Liu, H., K. C. Jezek and B. Li, 1999. Development of an Antarctic digital elevation model by integrating cartographic and remotely sensed data: A geographic information system based approach, *Journal of Geophysical Research*, **104**(B10), 23199–23213.

Liu, H., K. C. Jezek, B. Li and Z. Zhao, 2001. Radarsat Antarctic Mapping Project digital elevation model version 2, *Boulder CO*, **National Snow and Ice Data Center**, Digital media.

Massom, R. and D. Lubin, 2006. Polar Remote Sensing, vol. II Ice Sheets, Springer Verlag, Berlin Heidelberg New York.

Nixdorf, U., D. Steinhage, U. Meyer, L. Hempel, M. Jenett, P. Wachs and H. Miller, 1999. The newly developed airborne radio-echo sounding system of the AWI as a glaciological tool, *Annals of Glaciology*, **29**, 231–238.

Paterson, W.S.B., 1994. The physics of glaciers, Butterworth Heinemann, Oxford, UK, 3 ed.

Raymond, C.F., 1983. Deformation in the vicinity of ice divides, *Journal of Glaciology*, **29**(103), 357–373.

Riedel, B., 2003. The elastic behaviour of Ekstroemisen grounding zone, *FRISP Report*, (14), 1–5.

Rignot, E. and R. H. Thomas, 2002. Mass balance of polar ice sheets, *Science*, **297**, 1502–1506.

Rott, H., K. Sturm and H. Miller, 1993. Active and passive microwave signatures of Antarctica firn by means of field measurements and satellite data, *Annals of Glaciology*, **17**, 337–343.

Ruth, U., J.-M. Barnola, J. Beer, M. Bigler, T. Blunier, E. Castellano, H. Fischer, F. Fundel, P. Huybrechts, P. Kaufmann, S. Kipfstuhl, A. Lambrecht, A. Morganti, H. Oerter, F. Parrenin, O. Rybak, M. Severi, R. Udisti, F. Wilhelms and E.Wolff, 2007. EDML1: a chronology for the EPICA deep ice core from Dronning Maud Land, Antarctica, over the last 150 000 years, *Climate of the Past*, **3**, 475–484.

Schutz, B. E., 2002. Laser footprint location (geolocation) and surface profiles, *GLAS Algorithm Theoretical Basis Document version 3.0*, **Austin, TX: Center of Space Research**, University of Texas at Austin.

Seeber, G., 2003. Satellite Geodesy, de Gruyter, 2nd ed.

Steinhage, D., U. Nixdorf, U. Meyer and H. Miller, 1999. New maps of the ice thickness and subglacial topography in Dronning Maud Land, Antarctica, determined by means of airborne radio echo sounding, *Annals of Glaciology*, **29**, 267–272.

van der Veen, C. J., 1999. Fundamentals of Glacier Dynamics, Balkema, Rotterdam u.a.

Wesche, C., O. Eisen, H. Oerter, D. Schulte and D. Steinhage, 2007. Surface topography and ice flow in the vicinity of the EDML deep-drilling site, Antarctica, *Journal of Glaciology*, **53**(182), 442–448.

Wesche, C., S. Riedel, O. Eisen, H. Oerter, D. Schulte and D. Steinhage, in review. An improved DEM and refined ice divides for central Dronning Maud Land, Antarctica, *Journal of Glaciology*.

Wesche, C., S. Riedel and D. Steinhage, accepted. Precise surface topography of the grounded ice tongues at the Ekströmisen, Antarctica, based on several geophysical data sets, *ISPRS Journal of Photogrammetry and Remote Sensing*.

Wingham, D.J., A.J. Ridcout, R. Scharroo, R.J. Arthern and C.K. Shum, 1998. Antarctic elevation change from 1992 to 1996, *Science*, **282**, 456–458.

Zwally, H.J., B. Schutz, W. Abdalati, J. Abshire, C. Bentley, A. Brenner, J. Bufton, J. Dezio, D. Hancock, D. Harding, T. Herring, B. Minster, K. Quinn, S. Palm, J. Spinhirne and R. Thomas, 2002. ICESat's laser measurements of polar ice, atmosphere, ocean, and land, *Journal of Geodynamics*, **34**, 405–445.

Zwally, H. J., M. B. Giovinetto, J. Li, H. G. Cornejo, M. A. Beckley, A. C. Brenner, J. L. Saba and D. Yi, 2005. Mass changes of the Greenland and Antarctic ice sheets and shelves and contributions to sea-level rise: 1992-2002, *Journal of Glaciology*, **51**(175), 509–527.

Zwally, H. J., R. Schutz, C. Bentley, T. Bufton, T. Herring, J. Minster, J. Spinhirne and R. Thomas, 2007. GLAS/ICESat L2 Antarctic and Greenland Ice Sheet Altimetry Data V028, *Boulder, CO*, **National Snow and Ice Data Center**, Digital media.

Danksagung

Mein erster Dank gilt Herr Prof. Dr. Heinrich Miller für die Betreuung und die Begutachtung dieser Arbeit, sowie Prof. Dr. Katrin Huhn für die Übernahme des Zweitgutachtens und die motivierenden Gespräche. Ein besonderer Dank geht an Dr. Daniel Steinhage, der sich mehrfach durch die Arbeit gekämpft hat, mir immer mit Rat und Tat zur Seite stand und mir eine tolle Expedition ermöglichte. Weiterhin gilt mein Dank Dr. Olaf Eisen, der mir gerade das Schreiben der Veröffentlichungen erleichtert hat und ebenfalls in der Endphase dieser Arbeit immer bereit war mir zu helfen. Dr. Helgard Anschütz danke ich für die Unterstützung während der Endphase und Daniela Jansen danke ich für die Therapiesitzungen bei Kaffee und Kuchen. Weiterhin möchte ich mich bei der gesamten Arbeitsgruppe Glaziologie bedanken, besonders bei Maria, die immer ein offenes Ohr hatte. Natürlich darf ich meine Freunde in Nah und Fern nicht vergessen, die für die nötige Abwechslung gesorgt haben. Zum Schluss möchte ich mich auch noch bei meiner Familie bedanken. Meinen Eltern danke ich für die moralische Unterstützung und das Interesse an meiner Arbeit, Anne und Pete für die Aufmunterungen und netten Abende bei Werner und last but not least Melanie, danke für alles!

A. Reference stations

Table A.1.: Table of the permanent GPS reference stations, which were described in section 3.1.3. The coordinates are taken from the Scripps Orbit and Permanent Array Center (SOPAC - http://sopac.ucsd.edu/)

Station	IGS site code	Longitude	Latitude	Elevation
O'Higgins	ohi2	57.90133° W	63.32108° S	32.55 m
Palmer	palm	64.05112° W	64.77509° S	31.06 m
Sanae IV	vesl	2.84178° W	71.67380° S	862.36 m
Syowa	syog	39.58374° E	69.00696° S	50.00 m
Mawson	maw1	62.87071° E	67.60477° S	59.13 m
Davis	dav1	77.97261° E	68.57732° S	44.39 m
Amundsen/Scott	amun	139.19009° E	89.99780° S	2816.26 m

Table A.2.: Table of the non-permanent GPS reference stations, which were described in section 3.1.3.

Station	Longitude	Latitude	Elevation
Aboa[a]	13.40714° W	73.04377° S	468.64 m
Troll[b]	2.53808° E	72.01203° S	1313,53 m
Forster[c]	11.82506° E	70.77794° S	125.93 m

[a] Finnish Station, data provided by Hannu Koivula of the Finnish Geodetic Institute

[b] Norwegian Station, data provided by Axel Rülke of the Technical University Dresden

[c] survey point next to the former overwintering base Forster, data collected by the Technical University of Dresden and provided by Axel Rülke

Table A.3.: Static GPS points in DML. KRS is the Kohnen Reference Station near the EDML deep-drilling site. The sixth column shows the person in charge of the data processing.

Name	Longitude	Latitude	Elevation	Observation period	
KRS	0.0667° E	75.0018° S	2897.8 m	Jan. 2000 - Dec. 2005	D. Schulte[a], Ch. Wesche
DML01	2.5493° E	74.8564° S	2831.1 m	Jan. 1997 - Jan. 1999	B. Riedel[b], Ch. Wesche
DML02	3.9185° E	74.9683° S	3027.3 m	Jan. 1997 - Jan. 1999	B. Riedel, Ch. Wesche
DML03	1.9609° E	74.4995° S	2855.4 m	Jan. 1997 - Jan. 1999	B. Riedel, Ch. Wesche
DML05	0.0072° E	75.0024° S	2890.2 m	Jan. 2001 - Dec. 2005	Ch. Wesche
DML07	3.4306° W	75.5816° S	2680.1 m	Jan. 1997 - Jan. 1999	B. Riedel, Ch. Wesche
DML19	0.9951° W	75.1674° S	2849.5 m	Jan. 1999 - Jan. 2001	Ch. Wesche
DML25	0.0818° E	75.0060° S	2889.2 m	Jan. 2004 - Dec. 2005	Ch. Wesche
DML26	0.0099° E	74.8393° S	2881.9 m	Jan. 2001 - Dec. 2005	Ch. Wesche
DML27	0.7040° E	75.0560° S	2909.0 m	Feb. 2003 - Dec. 2005	Ch. Wesche
DML94	6.6989° W	71.1621° S	690.4 m	Jan. 2007	Ch. Wesche
DML95	6.6670° W	71.5680° S	538.8 m	Jan. 2007	Ch. Wesche
DML96	9.9167° W	71.4083° S	654.6 m	Jan. 2007	Ch. Wesche
DML97	9.5583° W	72.0640° S	760.2 m	Feb. 2007	Ch. Wesche
BA01	0.0678° E	75.0017° S	2891.1 m	Jan. 2003 - Dec. 2005	Ch. Wesche
HM01	0.0078° E	74.9939° S	2889.6 m	Jan. 2000 - Dec. 2005	Ch. Wesche
HM02	0.0394° E	75.0069° S	2889.6 m	Jan. 2000 - Dec. 2005	Ch. Wesche
HM03	0.0229° W	75.0074° S	2889.4 m	Jan. 2000 - Dec. 2005	Ch. Wesche
PEN1	0.0819° E	74.9654° S	2891.4 m	Jan. 2000 - Dec. 2005	Ch. Wesche
PEN2	0.2296° E	74.9945° S	2894.8 m	Jan. 2000 - Dec. 2005	Ch. Wesche
PEN3	0.1728° E	75.0393° S	2892.5 m	Jan. 2000 - Dec. 2005	Ch. Wesche
PEN4	0.0121° W	75.0388° S	2887.8 m	Jan. 2000 - Dec. 2005	Ch. Wesche
PEN5	0.0659° W	74.9937° S	2888.7 m	Jan. 2000 - Dec. 2005	Ch. Wesche

[a] Alfred Wegener Institute for Polar and Marine Research
[b] Technical University of Braunschweig

B. Elevation changes

B.1. Coast

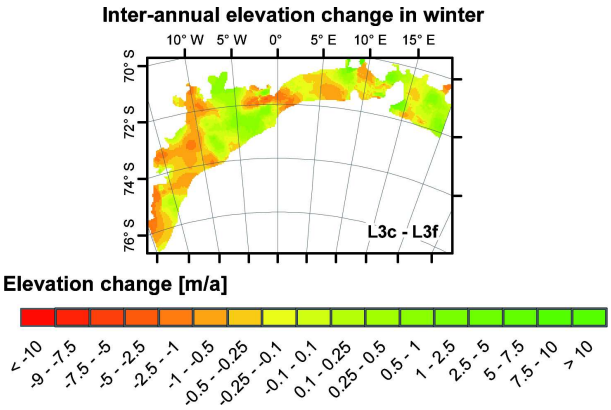

Figure B.1.: Annual elevation differences from GLA12 data, recorded in May and June 2005 and 2006.

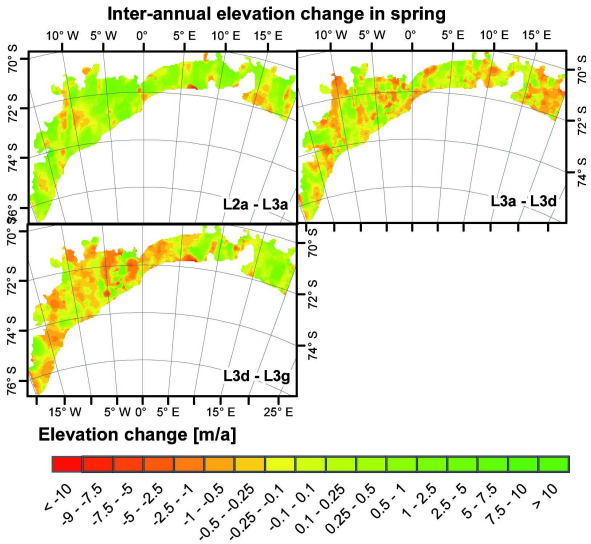

Figure B.2.: Annual elevation differences from GLA12 data, recorded between September and November in 2003 to 2006.

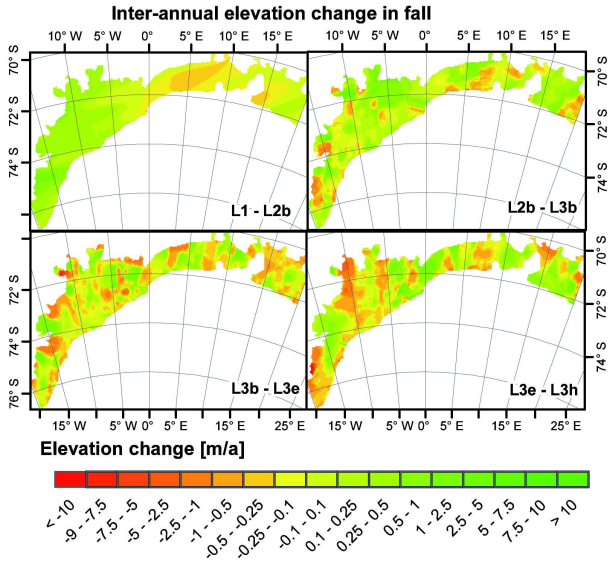

Figure B.3.: Annual elevation differences from GLA12 data, recorded between February and April in 2003 to 2007.

B.2. Plateau

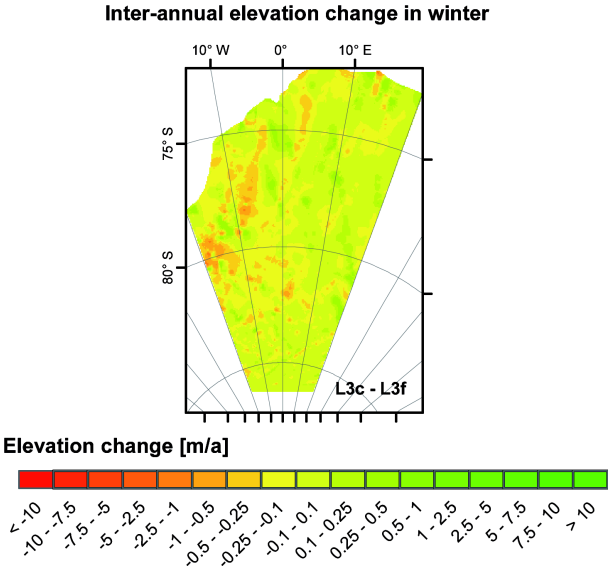

Figure B.4.: Annual elevation differences from GLA12 data, recorded in May and June 2005 and 2006.

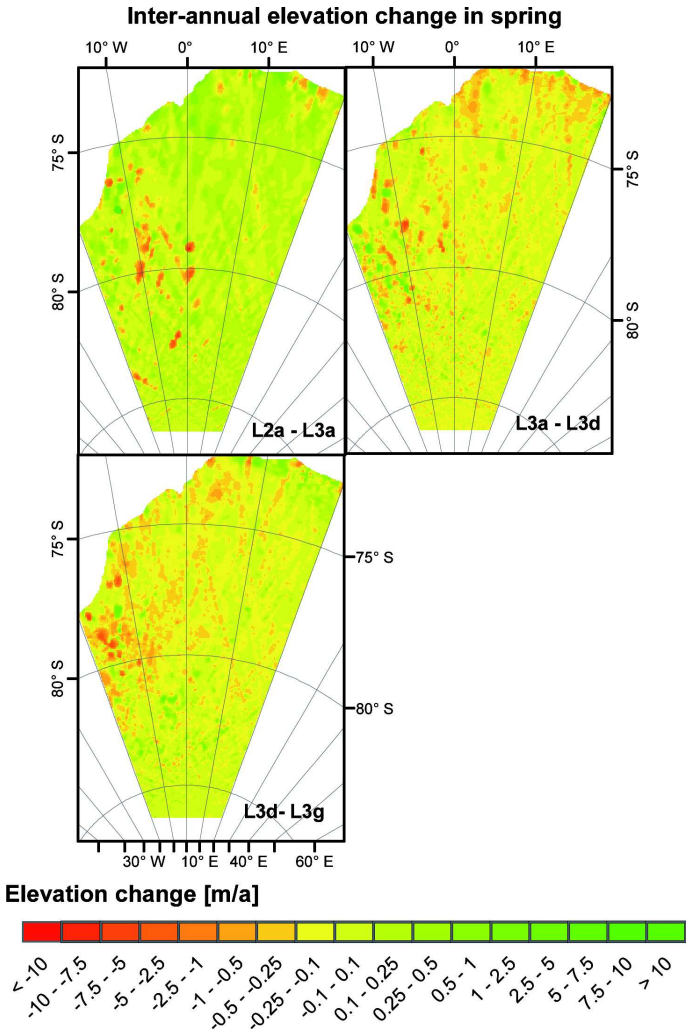

Figure B.5.: Annual elevation differences from GLA12 data, recorded between September and November in 2003 to 2006.

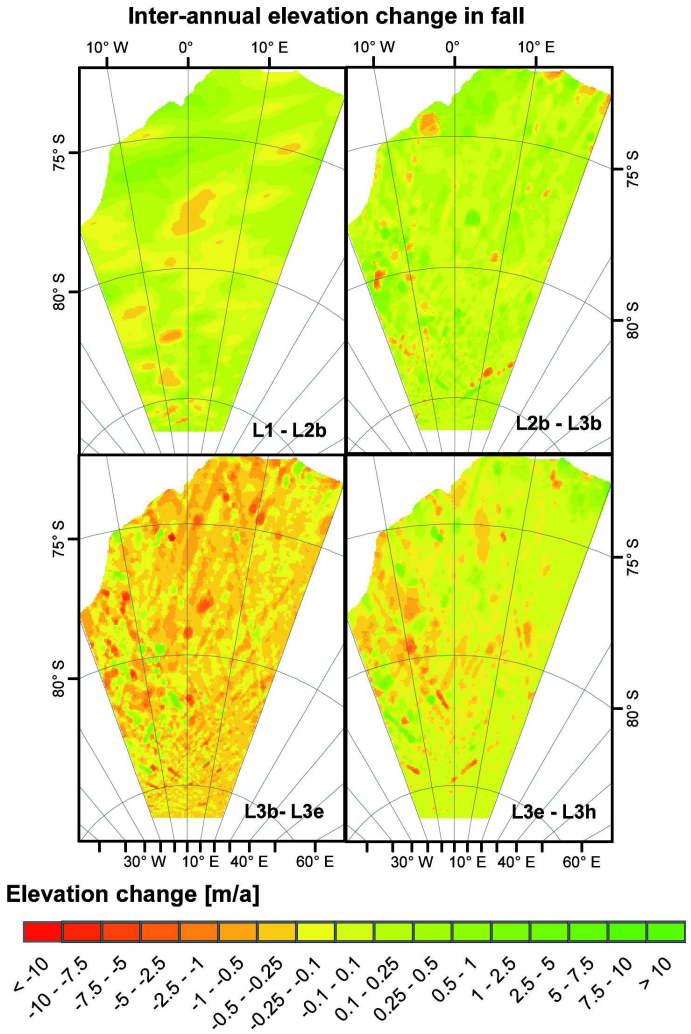

Figure B.6.: Annual elevation differences from GLA12 data, recorded between February and April in 2003 to 2007.

C. Maps of DML

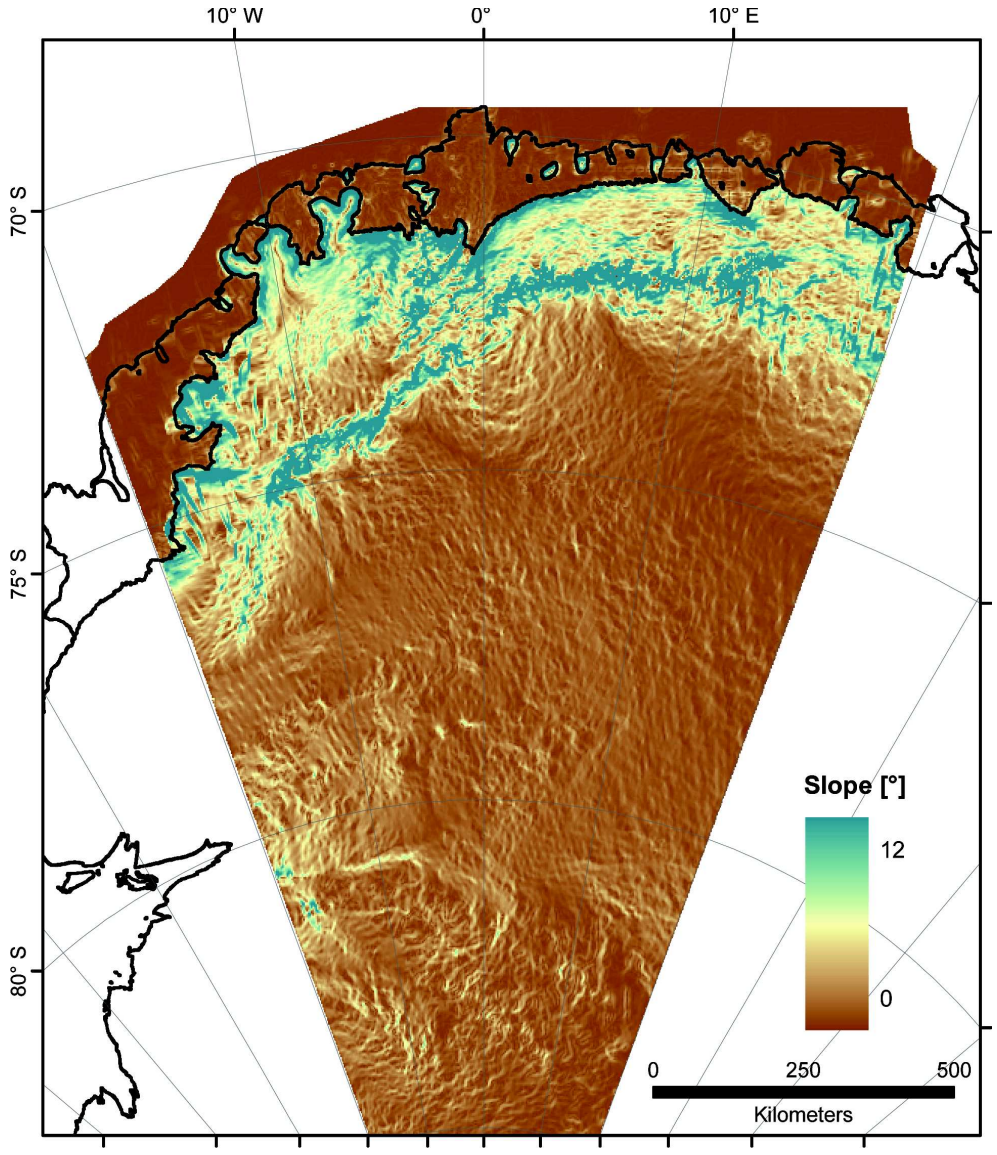

Figure C.1.: The surface slopes in DML based on the improved DEM.

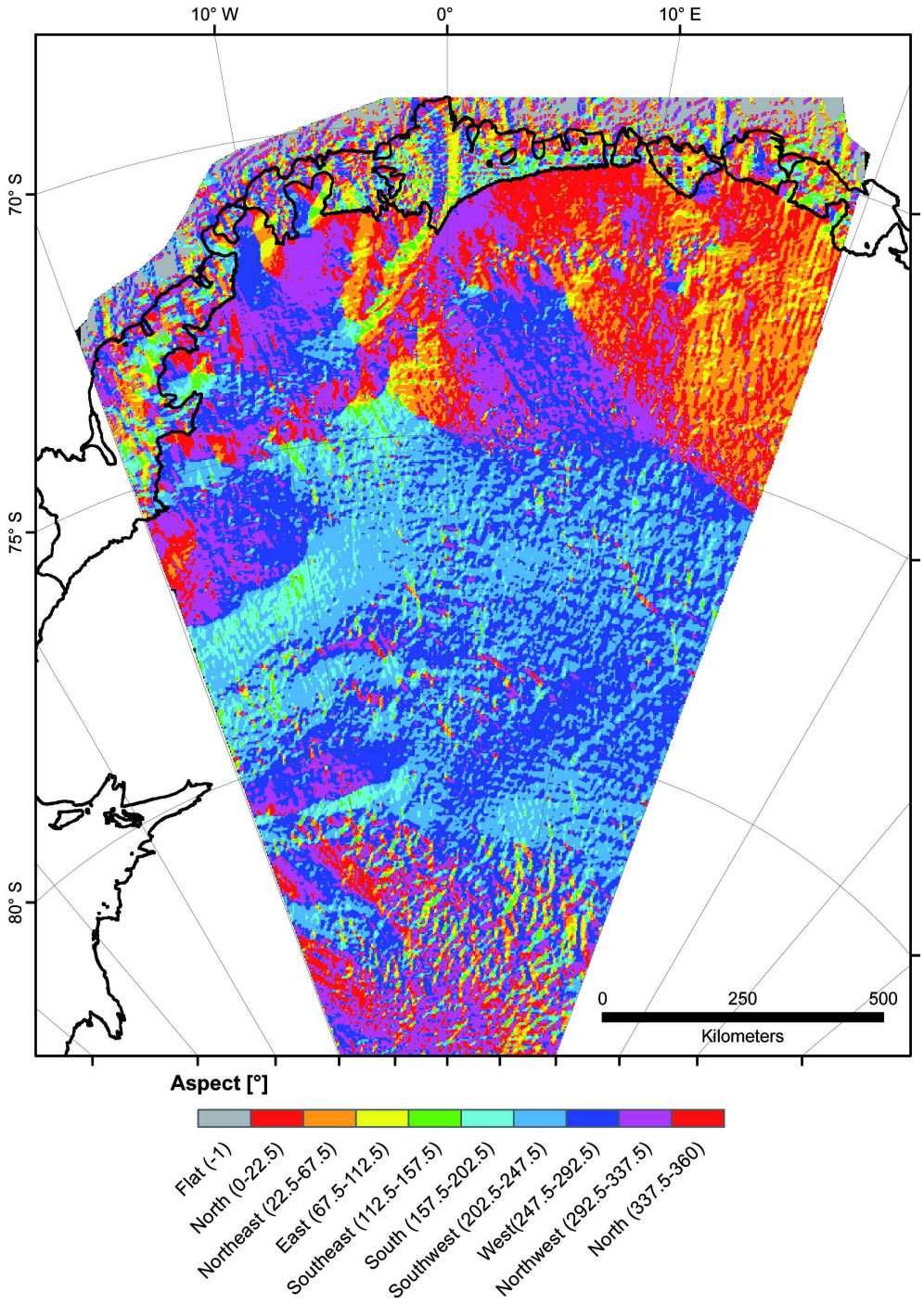

Figure C.2.: Aspect based on the improved DEM.

D. Publications

PAPER I

Surface topography and ice flow in the vicinity of the EDML deep-drilling site, Antarctica

Published in Journal of Glaciology 2007, Vol. 153, No. 182, pages 442-448

Surface topography and ice flow in the vicinity of the EDML deep-drilling site, Antarctica

Christine WESCHE,[1] Olaf EISEN,[1,2] Hans OERTER,[1] Daniel SCHULTE,[1] Daniel STEINHAGE[1]

[1]*Alfred Wegener Institute for Polar and Marine Research, PO Box 120161, D-27515 Bremerhaven, Germany*
E-mail: christine.wesche@awi.de
[2]*Laboratory of Hydraulics, Hydrology and Glaciology (VAW), ETH Zürich, CH-8092 Zürich, Switzerland*

ABSTRACT. Interpretation of ice-core records requires accurate knowledge of the past and present surface topography and stress–strain fields. The European Project for Ice Coring in Antarctica (EPICA) drilling site (75.0025° S, 0.0684° E; 2891.7 m) in Dronning Maud Land, Antarctica, is located in the immediate vicinity of a transient and forking ice divide. A digital elevation model is determined from the combination of kinematic GPS measurements with the GLAS12 datasets from the ICESat. Based on a network of stakes, surveyed with static GPS, the velocity field around the drilling site is calculated. The annual mean velocity magnitude of 12 survey points amounts to 0.74 m a^{-1}. Flow directions mainly vary according to their distance from the ice divide. Surface strain rates are determined from a pentagon-shaped stake network with one center point close to the drilling site. The strain field is characterized by along-flow compression, lateral dilatation and vertical layer thinning.

INTRODUCTION

Within the framework of the European Project for Ice Coring in Antarctica (EPICA) a deep ice core (EDML) was drilled in Dronning Maud Land (DML), Antarctica, near the German summer station, Kohnen (EPICA Community Members, 2006). To obtain high-resolution climate information of the last glacial cycle, a drilling site was chosen that provides comparatively high accumulation rates, large ice thickness and nearly undisturbed layering of the ice. The EDML drilling site (75.0025° S, 0.0684° E; 2891.7 m above the World Geodetic System 1984 (WGS84) ellipsoid) is located in the Atlantic sector of Antarctica (Fig. 1) and is used to investigate the connection between Northern and Southern Hemisphere climate variability in the past. The area surrounding the EDML drilling site is situated between two transient ice divides which fork at approximately 75.1° S, 1° E, according to the elevation model of Bamber and Bindschadler (1997). The deep ice-core drilling was carried out in the austral summer seasons 2000/01 to 2005/06. The ice thickness in this region is 2782 ± 5 m, as measured by airborne radio-echo sounding, and the total recovered core length was 2774.15 m (personal communication from F. Wilhelms, 2006). The drilling finished when subglacial water entered the borehole. The recent accumulation rate in the surroundings of the EDML drilling site is 64 kg m^{-2} a^{-1} (Eisen and others, 2005), with small-scale spatial variability of ~10%.

Accurate interpretation of the EDML ice-core data (e.g. past accumulation from annual layer thicknesses) requires knowledge of the complete strain field to correct for dynamic layer thickness variation. In this paper, we determine the topography, flow and strain field in the wider surroundings of the drilling site. Similar investigations were previously made at several drilling sites in Antarctica and Greenland. For example, Vittuari and others (2004) present a velocity field at Dome C (the first EPICA deep-drilling site (EPICA Community Members, 2004)) in the Indo-Pacific sector of the Antarctic ice sheet. In Greenland, Hvidberg and others (2002) investigated the ice flow at NorthGRIP, a drilling site that is also located in the vicinity of a transient ice divide. For the EDML site, a digital elevation model (DEM) is derived from the combination of ground-based kinematic GPS (global positioning system) and ICESat (Ice, Cloud and land Elevation Satellite) laser altimetry, providing highly accurate surface topography in the region of interest. This forms, together with ice velocity data, the basis for estimating and interpreting deformation in the upper part of the ice sheet.

DATA AND METHODS

Static and kinematic GPS measurements were used for our investigation. The elevation data derived from the kinematic GPS data were complemented by NASA's ICESat satellite laser altimetry data (US National Snow and Ice Data Center (NSIDC) http://nsidc.org/data/icesat/).

Kohnen Reference Station (KRS)

Kohnen Reference Station (KRS), which is located at the German summer station Kohnen (75.0018° S, 0.0667° E), is used for processing our GPS measurements. This is a non-permanent GPS station, providing data at 1 s intervals only during the drilling campaigns 2000/01 to 2005/06 (with interruptions in the season 2004/05). The KRS GPS antenna was mounted on the northern corner of the Kohnen station. With the aid of the International Global Navigation Satellite Systems Service (IGS) network, the daily position of KRS was determined using the GPS stations Mawson, Sanae IV, Syowa, Davis, Casey and O'Higgins (Fig. 1). The KRS positions were determined with the post-processing software GAMIT, assuming motion of the site was negligible during the processing window (Scripps Institution of Oceanography, http://sopac.ucsd.edu/processing/gamit/).

Surface profiles from kinematic GPS measurements

Kinematic GPS measurements combined with ground-penetrating radar (GPR) recorded during the 2000/01 field campaign (Eisen and others, 2005) form the basis for generating a DEM with a higher accuracy and resolution

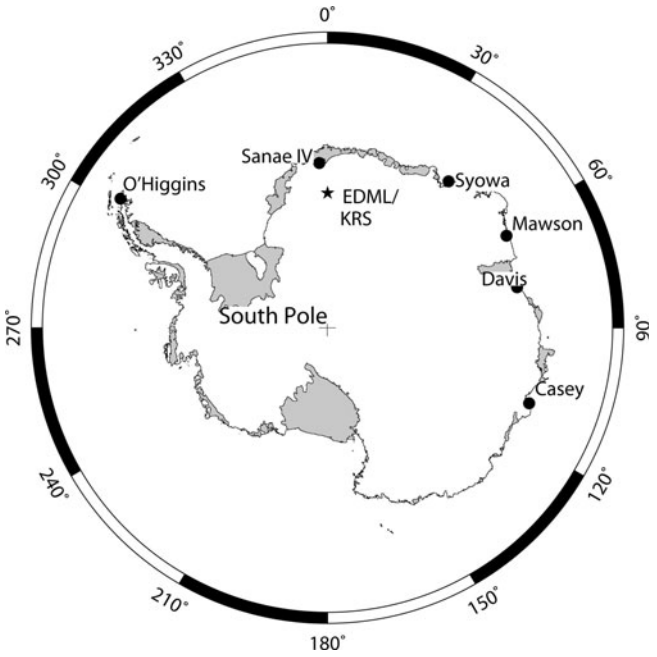

Fig. 1. Location map of the EDML drilling site in Antarctica, marked with a star. Six International Global Navigation Satellite Systems Service (IGS) reference stations are indicated with filled circles. They were used for determining the position of the local reference point Kohnen Reference Station (KRS) adjacent to the EDML drilling site.

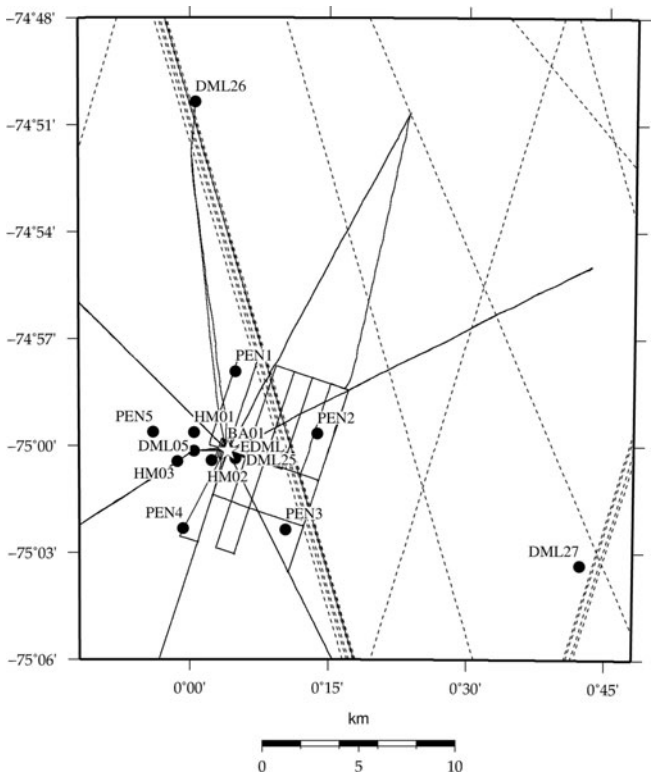

Fig. 2. Data coverage for the DEM derived in the present study. The solid lines present the kinematic GPS profiles, and the dotted lines the ICESat GLAS12 ground tracks. Sites used for static GPS measurements are marked with filled circles; the star marks the EDML drilling site.

than former DEMs in the surroundings of the EDML drilling site. A Trimble SSI 4000 GPS receiver was mounted on a snowmobile which was navigated at a velocity of about 10 km h^{-1} along predefined tracks (Fig. 2, solid lines) in the area of investigation (74.8–75.1° S, 0.2° W–0.8° E). There are two networks of kinematic GPS profiles, both centered on the EDML drilling site. The length of the edges of the first grid is 10 km with a profile spacing of 1–3 km. The second grid is a star-like pattern, which consists of seven 20–25 km legs. The kinematic GPS data were processed with Trimble Geomatics Office™ (TGO™), including precise ephemeris and ionosphere-free solution.

Flow and strain networks using static GPS measurements

In order to determine horizontal velocities and strain rates, static GPS measurements around the EDML drilling site were carried out with Ashtech Z-12 and Trimble SSI 4000 GPS receivers in the austral summer seasons between 1999/2000 and 2005/06. For the velocity network 13 points in the surroundings of the EDML drilling site were used (Fig. 2). These points are marked with aluminium stakes and were surveyed for approximately 1 hour per season to find their positions. The static GPS data were also processed with TGO™. All determined positions are available in the PANGAEA database (doi: 10.1594/PANGAEA.611331).

Surface profiles from satellite altimetry

The Geoscience Laser Altimeter System (GLAS) on board NASA's ICESat provides global altimetry data with a wavelength of 1064 nm up to 86° N and 86° S. The laser footprint has a diameter of 60 m, and the along-track distance between the footprints is 172 m. The positioning error is 35 m (Zwally and others, 2002). In this paper, GLAS12 altimetry data for the periods L1a (20 February to 20 March 2003) and L2a (25 September to 18 November 2003) are used to determine the surface elevation model of the investigated area. The ground tracks of these measurements across the investigated area are plotted in Figure 2 as dotted lines. The GLAS12 satellite laser altimetry data and the corresponding NSIDC GLAS Altimetry elevation extractor Tool (NGAT) are provided by NSIDC (http://nsidc.org/data/icesat/).

DATA ACCURACY

Knowledge of potential errors is essential for determining the quality of the kinematic and static GPS data. The general GPS errors and those of our solutions are presented in this section. The distance between the reference station and the survey point or profile is the principal factor affecting the accuracy of the position to be determined.

GPS errors

GPS observations at high latitudes are affected by the relatively weak satellite geometry, and hence formal errors are larger here than at other latitudes. Ionospheric and tropospheric effects were minimized by adopting the ionosphere-free linear combination and applying a tropospheric model. Further error reduction occurs through the double-differencing approach used in TGO™ and the relatively short baselines.

Kinematic GPS measurements

Since we used KRS, located in the center of the kinematic GPS profiles, systematic positioning errors are negligible. The accuracy of the kinematic GPS measurements is

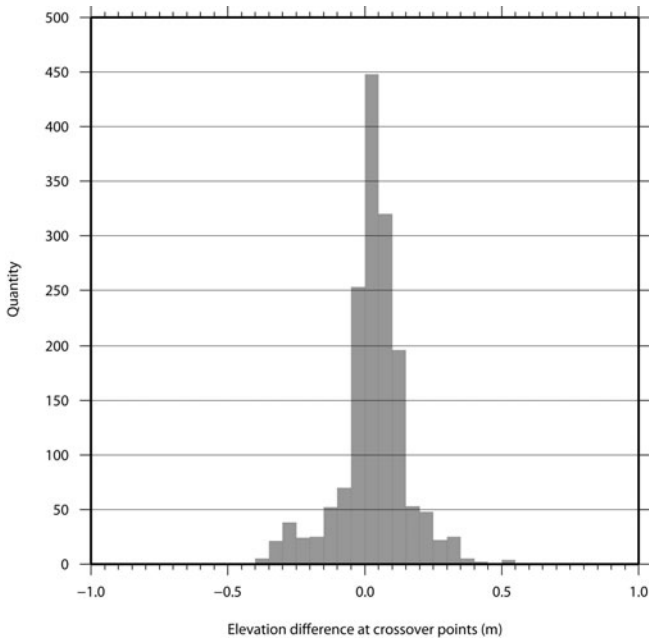

Fig. 3. Histogram of elevation differences at 1615 crossover points of the surveyed kinematic GPS profiles.

estimated by a crossover-point analysis. The histogram in Figure 3 shows the elevation differences at the 1615 crossover points. The mean elevation difference is 0.03 m with a standard deviation of 0.12 m.

Static GPS measurements

All stakes (Fig. 2) were occupied for an observation period of ~1 hour in several campaigns. The length of the baselines to KRS varied between 0.03 km (BA01) and 19.4 km (DML27). The positions of all stakes were computed using TGO™, and the formal horizontal and vertical errors (Table 1) were derived for every point in a processing report. The formal errors issued by GPS software are usually over-optimistic. Experience shows that these errors need to be scaled by a factor of 5–20, to be closer to the true uncertainty of the static GPS (personal communication from M. King, 2007). We take a factor of 20 as a conservative estimate of the precision of the GPS positions. As the accuracy depends on the baseline length, we use the points BA01 and DML27 to estimate the accuracy of the static GPS measurements.

The positions of these two points were calculated against KRS for two campaigns. They have quite different horizontal and vertical errors, which can be attributed to the longer baseline length between KRS and DML27. However, there are also significant differences between campaigns for the same point. For DML27, the horizontal and vertical errors in 2002/03 are almost an order of magnitude larger than in 2005/06. This may stem from the high sunspot activity in 2002/03 (http://solarscience.msfc.nasa.gov/SunspotCycle.shtml) in combination with the baseline length, despite using the ionosphere-free solution of TGO™. We assume that the maximum horizontal and vertical errors for our solutions are given by the values for DML27 of 0.30 m and 0.82 m, respectively, from the campaign in 2002/03.

Table 1. Error estimates for BA01 and DML27

Point	Campaign	Horizontal $1-\sigma$ error*	Vertical $1-\sigma$ error*	Baseline length
		m	m	m
BA01	2002/03	0.01	0.04	29.4
BA01	2005/06	0.01	0.02	29.7
DML27	2002/03	0.30	0.82	19 359.7
DML27	2005/06	0.04	0.10	19 358.9

*Based on formal errors issued by the GPS software, TGO™, scaled by a factor of 20.

Table 2. Calculated mean annual horizontal ice-flow velocities

Point	Magnitude	Direction	Period of averaging
	$m\,a^{-1}$	°	
BA01	0.682	272.6	Jan. 2003–Dec. 2005
DML05	0.660	270.4	Jan. 2001–Dec. 2005
DML25	0.830	274.2	Jan. 2004–Dec. 2005
DML26	1.066	335.9	Jan. 2001–Dec. 2005
DML27	0.963	287.5	Feb. 2003–Dec. 2005
HM01	0.642	273.7	Jan. 2000–Dec. 2005
HM02	0.684	270.0	Jan. 2000–Dec. 2005
HM03	0.674	266.6	Jan. 2000–Dec. 2005
PEN1	0.643	291.3	Jan. 2000–Dec. 2005
PEN2	0.767	282.9	Jan. 2000–Dec. 2005
PEN3	0.859	265.9	Jan. 2000–Dec. 2005
PEN4	0.841	257.9	Jan. 2000–Dec. 2005
PEN5	0.624	269.8	Jan. 2000–Dec. 2005

GLAS data

ICESat's positioning precision is stated as 35 m and the predicted elevation data accuracy is 0.15 m (Zwally and others, 2002). Shuman and others (2006) presented a new elevation accuracy assessment of ~0.02 m for low-slope and clear-sky conditions. Our area of investigation is a low-slope region, but clouds during the observation period cannot be excluded over the whole period. The elevation measurements of the ICESat laser altimeter refer to the TOPEX/Poseidon ellipsoid. Differences in elevation between the TOPEX/Poseidon ellipsoid and the WGS84 ellipsoid are approximately 0.71 m in the region of interest (personal communication from T. Haran, 2005). When transforming to the WGS84 ellipsoid we subtract this value from all GLAS12 elevation data.

RESULTS

Surface topography

The derived surface topography in the area of investigation refers to the WGS84 ellipsoid and is a combination of the GPS and the GLAS12 datasets (Fig. 4, contours). A crossover-point analysis was performed before combining the datasets to identify systematic offsets and to estimate the uncertainties. As crossover points for the GPS data we use the average of all GPS measurements within the diameter of the GLAS footprint of about 60 m. Considering all crossover points, the GLAS12 data (transformed to the WGS84 ellipsoid) are found to be 0.119 m lower than the GPS data, on average. This elevation difference was added to the GLAS12 data, i.e. we corrected the elevations to the GPS

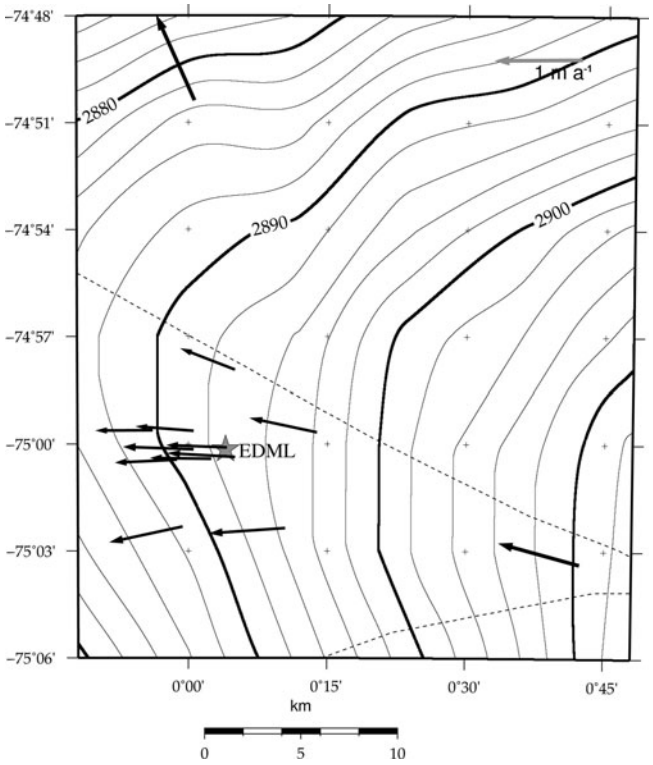

Fig. 4. Surface flow-velocity vectors in the area of interest, plotted on the contour map of the combined and gridded (5 km × 5 km) GPS/GLAS12 elevation model. The contour interval is 2 m. The dotted curves indicate the ice divide corresponding to the DEM of Bamber and Bindschadler (1997).

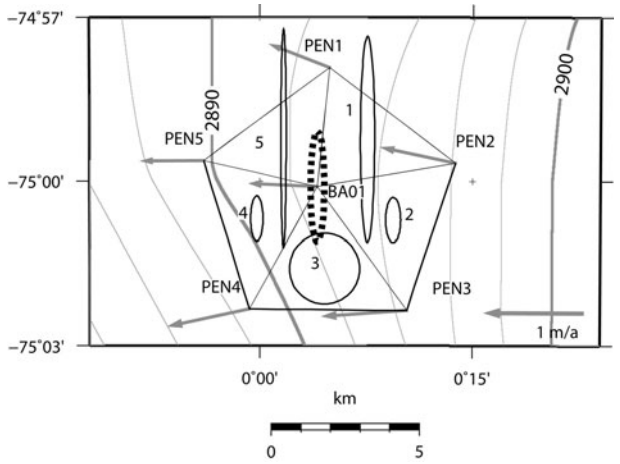

Fig. 5. Velocity vectors of the pentagon-shaped network (PEN1–PEN5) and BA01. Strain ellipses are plotted for the five strain triangles, indicated by numbers 1–5. The mean strain ellipse (dotted) is centered on BA01. See text for the calculation of the mean strain ellipse. The elevation contour interval is 2 m.

profiles. To get sufficient spatial coverage of elevation data over the whole area of investigation, we interpolated the combined dataset with a minimum-curvature algorithm (Wessel and Smith, 1991) on a 5 km × 5 km grid (Fig. 4). With this grid size, at least one data point was available for each gridcell, even several tens of kilometers away from the drilling site.

Surface velocity

The velocity magnitude at the survey points between the two ice divides varies between 0.62 m a^{-1} (PEN5) and 0.96 m a^{-1} (DML27). The flow direction varies between 257.9° (PEN4) and 291.3° (PEN1). The flow velocity of DML26, north of the divide, is outside this range, moving in a direction of 335.9° with a magnitude of 1.07 m a^{-1} (Table 2; Fig. 4).

The location of the EDML drilling site was surveyed on 10 January 2001, before the drilling operation started, yielding 75.0025° S, 0.068° E and 2891.7 m at the snow surface. As excavation of the drill trench does not allow accurate remeasurements, we use the mean velocities of the points next to it, DML25 and BA01. We thus obtain a value of 0.756 m a^{-1} in the direction of 273.4° for the ice velocity at the drilling site. The precision of the velocity measurements differs, depending on the period and data used (see Table 1). We therefore perform a propagation of errors by

$$\delta v^2 = \left(\frac{v}{s}\,\delta s_\mathrm{m}\right)^2 + \left(\frac{v}{t}\,\delta t\right)^2. \qquad (1)$$

Only the horizontal errors are used; the vertical errors are neglected for calculating the propagated error (δv) of the annual movement. Here, v is the velocity magnitude and s the horizontal offset of the survey point over the measurement interval (t). The term δs_m is the mean of the horizontal errors for the survey point of the two campaigns used for the determination of the velocities. The time error, δt, is assumed to be a constant of 1 day (1/365.25 years), because the start and end time is rounded by the day. The resulting errors for sites DML27 and BA01 are 0.059 and 0.003 m a^{-1}, respectively. As discussed above, we take the error at DML27 as the maximum error of the velocity determination, as it has the longest baseline.

Surface strain rates

Strain rates were determined from a pentagon-shaped network (PEN1–PEN5) with BA01 as the center reference pole (Fig. 5). Using the horizontal surface velocities in Table 2, with the geodetical nomenclature of y as the eastward and x as the northward components, we determine the strain-rate components from (Paterson, 1994)

$$\dot{\varepsilon}_x = \frac{\Delta v_x}{\Delta x}, \qquad \dot{\varepsilon}_y = \frac{\Delta v_y}{\Delta y}, \qquad (2)$$

and the combined strain rate as

$$\dot{\varepsilon}_{xy} = \frac{1}{2}\left(\frac{\Delta v_x}{\Delta y} + \frac{\Delta v_y}{\Delta x}\right), \qquad (3)$$

where Δv_x and Δv_y are the differences of the x and y velocity components of the considered pair of survey points, and Δx and Δy are the distances between the stakes in the x and y directions. Distances from the reference pole to each pentagon point vary between 3961.85 m (BA01–PEN5) and 5173.28 m (BA01–PEN3). Using Equation (3) the combined surface strain rate is calculated for every pair of neighboring points (west–east and south–north), yielding ten values (Table 3).

To determine the strain rates, we divide the pentagon into five strain triangles (Fig. 5) and assume the strain is constant over the area of the triangle. We calculate the average of the strain for each triangle (e.g. the mean of BA01/PEN1, BA01/PEN2 and PEN1/PEN2 for the northeastern triangle, numbered 1). The principal components are calculated using the

Table 3. Strain rates for pairs of survey points

Pair of points	$\dot{\varepsilon}_{xy}$	$\dot{\varepsilon}_x$	$\delta\dot{\varepsilon}_x$	$\dot{\varepsilon}_y$	$\delta\dot{\varepsilon}_y$	Δv_x	Δv_y
	a^{-1}	a^{-1}	a^{-1}	a^{-1}	a^{-1}	$m\,a^{-1}$	$m\,a^{-1}$
BA01/PEN1	-2.20×10^{-4}	-2.02×10^{-5}	1.47×10^{-5}	-9.61×10^{-4}	2.85×10^{-4}	–0.08	–0.20
BA01/PEN2	-5.44×10^{-5}	6.73×10^{-5}	5.83×10^{-5}	-2.74×10^{-5}	1.29×10^{-5}	0.07	–0.13
BA01/PEN3	-1.57×10^{-5}	-4.35×10^{-5}	1.49×10^{-5}	2.86×10^{-5}	1.86×10^{-5}	–0.18	0.09
BA01/PEN4	-5.81×10^{-5}	-3.32×10^{-5}	1.41×10^{-5}	-9.90×10^{-5}	2.87×10^{-5}	–0.14	–0.21
BA01/PEN5	-3.12×10^{-5}	-8.24×10^{-5}	8.63×10^{-5}	-8.49×10^{-5}	1.54×10^{-5}	–0.06	–0.03
PEN1/PEN2	-4.73×10^{-5}	-4.97×10^{-5}	1.97×10^{-5}	1.70×10^{-5}	1.36×10^{-5}	–0.15	0.08
PEN1/PEN5	-3.79×10^{-5}	-7.38×10^{-6}	1.78×10^{-5}	-5.73×10^{-5}	1.46×10^{-5}	–0.02	–0.24
PEN2/PEN3	-5.96×10^{-5}	-2.10×10^{-5}	1.18×10^{-5}	-1.57×10^{-4}	4.28×10^{-5}	–0.11	–0.22
PEN3/PEN4	-2.71×10^{-4}	1.65×10^{-4}	2.87×10^{-4}	-2.16×10^{-5}	1.13×10^{-5}	0.03	–0.11
PEN4/PEN5	-3.72×10^{-5}	-4.01×10^{-5}	1.21×10^{-5}	9.63×10^{-5}	3.32×10^{-5}	–0.20	0.17

Note: Combined ($\dot{\varepsilon}_{xy}$) and directional ($\dot{\varepsilon}_x$ and $\dot{\varepsilon}_y$) strain rates with conservative error estimates ($\delta\dot{\varepsilon}_x$ and $\delta\dot{\varepsilon}_y$); differences of the velocity components in north–south (Δv_x) and east–west (Δv_y) direction for BA01 and PEN1–PEN5. In this work, the differences of the velocity components were calculated by west minus east values, and south minus north values. Negative strain rates thus correspond to compression, and positive strain rates to extension.

rotation, θ, of the x and y axes

$$\tan 2\theta = \frac{2\dot{\varepsilon}_{xy}}{\dot{\varepsilon}_x - \dot{\varepsilon}_y}. \quad (4)$$

This provides one of two values for θ, which are 90° apart. One gives the direction of the maximum strain rate, $\dot{\varepsilon}_{max}$, the other of minimum strain rate, $\dot{\varepsilon}_{min}$. The strain-rate magnitudes along these directions follow from

$$\dot{\varepsilon}_{max,\,min} = \dot{\varepsilon}_x \cos^2\theta_{max,\,min} + \dot{\varepsilon}_y \sin^2\theta_{max,\,min} + 2\dot{\varepsilon}_{xy} \sin\theta_{max,\,min} \cos\theta_{max,\,min}. \quad (5)$$

This calculation is repeated for every strain triangle. The direction of maximum strain rate varies between 30.1° and 75.0°. Using the incompressibility condition (Paterson, 1994)

$$\dot{\varepsilon}_x + \dot{\varepsilon}_y + \dot{\varepsilon}_z = 0, \quad (6)$$

we estimate the flow-induced vertical strain rate $\dot{\varepsilon}_z$. It varies between 1.31×10^{-6} and $3.79\times10^{-4}\,a^{-1}$ (Table 4), with a standard variation of $6.49\times10^{-5}\,a^{-1}$. To estimate a strain rate representative of the EDML drilling site, we determine the average horizontal deformation and its direction at BA01. For this purpose, the arithmetic means of $\dot{\varepsilon}_{xy}$, $\dot{\varepsilon}_x$ and $\dot{\varepsilon}_y$ from the strain triangles are calculated and used in Equations (4) and (5) (Table 4). The maximum rate is $-1.85\times10^{-4}\,a^{-1}$, acting in the direction of 65.8°. The minimum rate, $2.32\times10^{-5}\,a^{-1}$, acts in the direction of 155.8°. In addition to the arithmetic mean, we determine the weighted mean for the directional and vertical strain-rate components ($\dot{\varepsilon}_{x,\,y,\,z}$), using the strain-rate error weights (Table 4). The arithmetic mean of the vertical strain rate, $\dot{\varepsilon}_z$, is $(1.62\pm1.25)\times10^{-4}\,a^{-1}$, and the weighted mean is $(1.09\pm1.25)\times10^{-4}\,a^{-1}$.

DISCUSSION

The DEM presented here is compared with the DEM generated by Bamber and Bindschadler (1997) from European Remote-sensing Satellite-1 (ERS-1) radar altimetry, which is also available on a 5 km × 5 km grid. For comparison, we subtract the Bamber and Bindschadler (1997) DEM from our combined GPS/GLAS12 DEM. The northeastern edge of the area of investigation is striking, where the elevations of the Bamber and Bindschadler (1997) DEM are about 2 m higher than those in our DEM (Fig. 6). Calculating the mean difference between the combined GPS/GLAS12 DEM and the Bamber and Bindschadler (1997) DEM for every 5 km × 5 km gridcell, we determine a mean elevation difference of –0.33 m. That is, the DEM of Bamber and

Table 4. Strain rates for the strain triangles

Strain triangle	$\dot{\varepsilon}_{xy}$	$\dot{\varepsilon}_x$	$\delta\dot{\varepsilon}_x$	$\dot{\varepsilon}_y$	$\delta\dot{\varepsilon}_y$	$\dot{\varepsilon}_z$	$\delta\dot{\varepsilon}_z$	$\dot{\varepsilon}_{max}$	θ_{max}	$\dot{\varepsilon}_{min}$	θ_{min}
	a^{-1}	a^{-1}	a^{-1}	a^{-1}	a^{-1}	a^{-1}	a^{-1}	a^{-1}	°	a^{-1}	°
1	-9.30×10^{-5}	-8.70×10^{-7}	3.66×10^{-5}	-3.24×10^{-4}	1.65×10^{-4}	3.25×10^{-4}	1.69×10^{-4}	-3.49×10^{-4}	75.03	2.40×10^{-5}	165.03
2	-4.32×10^{-5}	9.60×10^{-7}	3.54×10^{-5}	-5.18×10^{-5}	2.80×10^{-5}	5.09×10^{-5}	4.51×10^{-5}	-7.61×10^{-5}	60.71	2.52×10^{-5}	150.71
3	-1.15×10^{-4}	2.94×10^{-5}	1.66×10^{-4}	-3.07×10^{-5}	2.08×10^{-5}	1.31×10^{-6}	1.67×10^{-4}	-1.20×10^{-4}	52.32	1.18×10^{-4}	142.32
4	-4.22×10^{-5}	-5.19×10^{-5}	5.10×10^{-5}	-3.74×10^{-6}	2.68×10^{-5}	5.56×10^{-5}	5.76×10^{-5}	-7.64×10^{-5}	30.13	2.07×10^{-5}	120.13
5	-9.63×10^{-5}	-3.67×10^{-5}	5.18×10^{-5}	-3.42×10^{-4}	1.65×10^{-4}	3.79×10^{-4}	1.73×10^{-4}	-3.70×10^{-4}	73.89	-8.83×10^{-6}	163.89
Arithmetic mean	-7.80×10^{-5}	-1.18×10^{-5}	3.76×10^{-5}	-1.50×10^{-4}	4.74×10^{-5}	1.62×10^{-4}	6.05×10^{-5}	-1.85×10^{-4}	65.83	2.32×10^{-5}	155.83
Weighted mean		-1.54×10^{-5}		-5.64×10^{-5}		1.09×10^{-4}					

Note: Combined ($\dot{\varepsilon}_{xy}$), directional ($\dot{\varepsilon}_x$ and $\dot{\varepsilon}_y$), vertical strain rate ($\dot{\varepsilon}_z$), maximum and minimum strain rate ($\dot{\varepsilon}_{max}$ and $\dot{\varepsilon}_{min}$) and the direction of maximum and minimum strain rate (θ_{max} and θ_{min}). The conservative error estimates for the directional and vertical strain rates for the five triangles are denoted by $\delta\dot{\varepsilon}_{(x,y,z)}$. Weighted mean refers to the weighting by corresponding errors. See text for the calculation of the arithmetic and weighted means.

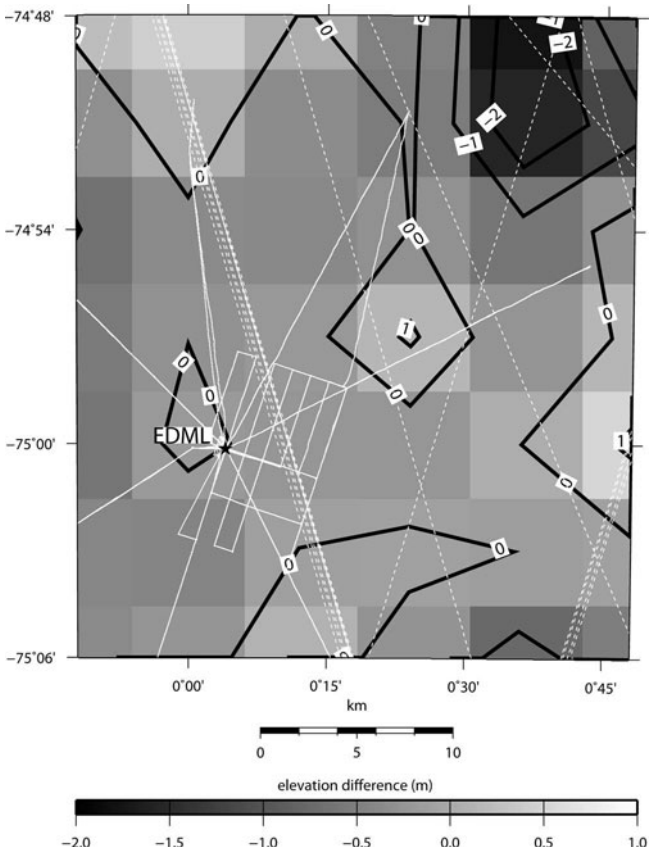

Fig. 6. Elevation differences of our GPS/GLAS12 DEM minus the Bamber and Bindschadler (1997) DEM. The contour interval is 1 m. Kinematic GPS and GLAS12 data coverage used in this paper (Fig. 2) are plotted as white dotted (GLAS12) and solid (GPS) lines.

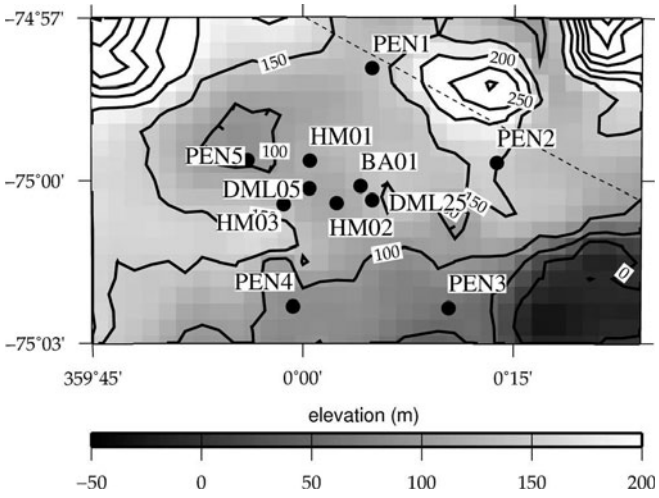

Fig. 7. Subglacial topography of the area of investigation gridded on a 500 m × 500 m raster after Steinhage and others (1999). The spacing between the contours is 50 m. The dotted line represents the ice divide corresponding to Bamber and Bindschadler (1997).

Bindschadler (1997) is about 0.3 m higher than our combined GPS/GLAS12 DEM.

The topography in the region of interest shows a smooth surface, slightly sloping down to the west. One major feature is a transient ice divide, which splits ~20 km upstream of the drilling location, thus separating three drainage basins. Of our 13 survey points, 12 are located between the two branches of the ice divide; only DML26 is located north of both ice branches (Fig. 4). As it represents a different drainage basin and flow regime, we exclude DML26 from further analysis. The ice divide and the local surface elevation are the largest factors determining the flow and strain field. This is evident from comparison of the mean slope direction at the drilling site with the mean flow direction of 273.5° from the GPS-based velocity measurements. Small differences in magnitude and direction of the horizontal ice-flow velocities of the survey points are likewise mainly caused by the relative location of the survey point in respect to the ice divide. Points very close to the ice divide are generally slower and the direction of movement is nearly parallel to the course of the divide (Fig. 4 and Table 2, e.g. PEN1). The magnitude of the flow velocity increases with increasing distance from the divide, and the northward flow component is reduced (Fig. 4; Table 2). An exception is PEN5, which has a slightly lower velocity (0.624 m a^{-1}) than PEN1 (0.643 m a^{-1}) despite the greater distance from the divide. Although this difference is smaller than the estimated conservative maximum velocity error of 0.059 m a^{-1}, we try to identify the origin of this variation.

Investigating the local bedrock topography in the vicinity of PEN5, available from airborne radio-echo soundings (Steinhage and others, 1999), PEN5 is found to be located above a depression of the subglacial topography (Fig. 7). The depression is ~5 km wide and several tens of meters deep, with respect to the surrounding average bedrock elevation. Because of the smoothing effect of ice dynamics, the surface elevation is much smoother than the bedrock topography. Surface topography varies only in the order of meters. The depression therefore simply causes locally increased ice thickness, but not a significant feature at the surface. The slightly lower velocity at PEN5, compared to the other stakes, is thus a consequence of the flux balance required by the larger ice thickness.

The surface strain rate at BA01, averaged from the strain triangles of the five pentagon points (PEN1–PEN5), is considered to be representative for the EDML ice core, as BA01 is only 93 m to the northeast of the drilling site. Most error estimates for the strain rates (Tables 3 and 4) are about equal to or smaller than the nominal value of the strain rate. For some strain rates with very small nominal values, the error is more than one order of magnitude larger (e.g. $\dot{\varepsilon}_x$ triangle 3, Table 4). We emphasize that the velocity errors are very conservative estimates, so the strain-rate errors are also conservative estimates. The average maximum principal component of the strain rate at BA01 is negative (-1.85×10^{-4} a^{-1}). It acts as a compressing force in the direction of 65.8°. The minimum principal component of the strain rate at BA01 is positive (2.32×10^{-5} a^{-1}). It therefore corresponds to a dilatational force and acts along an axis in the direction of 155.8°. This results from the low magnitude of the velocity at PEN5. Both BA01 and PEN2 (upstream of PEN5) are moving faster than PEN5, which induces the along-flow compression of the ice mass. The average vertical strain rate, as calculated above, shows that the compression in the northwest–southeast direction only partly compensates the dilatational component of the strain field in the northeast–southwest direction, perpendicular to the ice flow at EDML, and layer thinning is required in the vertical component to achieve balance.

CONCLUSION

We provide an improved dataset for the surface topography and flow velocity in the vicinity of the EDML drilling site. A DEM of high accuracy was derived from a combination of kinematic surface GPS measurements and satellite laser altimetry from ICESat's GLAS12 data. Static GPS measurements at 13 stakes between the austral summer seasons 1997/98 and 2005/06 provided the basis for deriving the flow velocity field and resulting strain rates. The flow velocity field is, in general, divergent along the course of and in between the two branches of the ice divide. On top of this general field, small velocity variations are superimposed, which are caused by local variations in ice thickness resulting from undulations in bedrock topography. The horizontal strain field, calculated from the velocities, shows lateral extension and smaller longitudinal compression. This results in layer thinning in the EDML ice core, which has to be accounted for to yield a correct interpretation of ice-core data.

ACKNOWLEDGEMENTS

The data of GPS reference stations were allocated by A. Rülke of the Institute for Planetary Geodesy of the Technical University of Dresden (http://www.tu-dresden.de/ipg/). Satellite altimetry data were provided by the US National Snow and Ice Data Center, Boulder, CO (http://nsidc.org/data/icesat/). The authors thank D. Jansen for helpful discussions. This work is a contribution to the European Project for Ice Coring in Antarctica (EPICA), a joint European Science Foundation (ESF)/European Commission (EC) scientific program, funded by the EC and by national contributions from Belgium, Denmark, France, Germany, Italy, The Netherlands, Norway, Sweden, Switzerland and the UK. The main logistic support at Dronning Maud Land was provided by AWI. This is EPICA publication No. 177. Preparation of this work was supported by Deutsche Forschumgsgemeinschaft with the 'Emmy Noether' scholarship EI-672/1 to O.E. This paper was enhanced significantly by the comments of M. King, R. Jacobel and R. Bindschadler.

REFERENCES

Bamber, J.L. and R.A. Bindschadler. 1997. An improved elevation dataset for climate and ice-sheet modelling: validation with satellite imagery. *Ann. Glaciol.,* **25**, 439–444.

Eisen, O., W. Rack, U. Nixdorf and F. Wilhelms. 2005. Characteristics of accumulation around the EPICA deep-drilling site in Dronning Maud Land, Antarctica. *Ann. Glaciol.,* **41**, 41–56.

EPICA Community Members. 2004. Eight glacial cycles from an Antarctic ice core. *Nature,* **429**(6992), 623–628.

EPICA Community Members. 2006. One-to-one coupling of glacial climate variability in Greenland and Antarctica. *Nature,* **444**(7116), 195–198.

Hvidberg, C.S., K. Keller and N.S. Gundestrup. 2002. Mass balance and ice flow along the north-northwest ridge of the Greenland ice sheet at NorthGRIP. *Ann. Glaciol.,* **35**, 521–526.

Paterson, W.S.B. 1994. *The physics of glaciers. Third edition.* Oxford, etc., Elsevier.

Shuman, C.A. *and 6 others*. 2006. ICESat Antarctic elevation data: preliminary precision and accuracy assessment. *Geophys. Res. Lett.,* **33**(L7), L07501. (10.1029/2005GL025227.)

Steinhage, D., U. Nixdorf, U. Meyer and H. Miller. 1999. New maps of the ice thickness and subglacial topography in Dronning Maud Land, Antarctica, determined by means of airborne radio-echo sounding. *Ann. Glaciol.,* **29**, 267–272.

Vittuari, L. *and 6 others*. 2004. Space geodesy as a tool for measuring ice surface velocity in the Dome C region and along the ITASE traverse. *Ann. Glaciol.,* **39**, 402–408.

Wessel, P. and W.H.F. Smith. 1991. Free software helps map and display data. *Eos,* **72**(41), 441, 445–446.

Zwally, H.J. *and 15 others*. 2002. ICESat's laser measurements of polar ice, atmosphere, ocean and land. *J. Geodyn.,* **34**(3–4), 405–445.

MS received 26 October 2006 and accepted in revised form 15 April 2007

PAPER II

Precise surface topography at the Ekströmisen, Antarctica, based on several geophysical data sets

ISPRS Journal of Photogrammetry and Remote Sensing, accepted

Precise surface topography of the grounded ice tongues at the Ekströmisen, Antarctica, based on several geophysical data sets

C. Wesche *, S. Riedel, D. Steinhage

Alfred Wegener Institute for Polar and Marine Research Bremerhaven, Germany

Abstract

As part of the CryoSat Cal/Val activities and the pre-site survey for an ice core drilling contributing to the International Partnerships in Ice Core Sciences (IPICS), ground based kinematic GPS measurements were conducted in early 2007 in the vicinity of the German overwintering station Neumayer (8.25° W and 70.65° S). The investigated area comprises the regions of the ice tongues Halvfarryggen and Søråsen, which rise from the Ekströmisen to a maximum of about 760 m surface elevation, and have an areal extent of about 100 km x 50 km each. Available digital elevation models (DEMs) from radar altimetry and the Antarctic Digital Database show elevation differences of up to hundreds of meters in this region, which necessitated an accurate survey of the conditions on-site. An improved DEM of the Ekströmisen surroundings is derived by a combination of highly accurate ground based GPS measurements, satellite derived laser altimetry data (ICESat), airborne radar altimetry (ARA), and radio echo sounding (RES). The DEM presented here achieves a vertical accuracy of about 1.3 m and can be used for improved ice dynamic modeling and mass balance studies.

Key words: GPS, ICESat, radar altimetry

1 Introduction

Ice sheets play a major role in the climate system and changes in their mass balance affect the global sea level. Currently, the absolute mass balances of the ice sheets are only slightly above the measurement uncertainties and changes in mass balance may even be below the precision of the measurements (Wingham et al., 1998; Abdalati et al., 2002; Zwally et al., 2002). The Antarctic ice sheet covers an area of about 12.4×10^6 km^2 with an average ice thickness of about 2.4 km (Massom and Lubin, 2006). The steep margins of the Antarctic ice sheet form the transition zone between the grounded flat interior and the floating ice shelves which are very sensitive for climate variability. The knowledge of the surface topography of the Antarctic ice sheet is an important input parameter for ice dynamic modeling and mass balance studies. Recent mass balance studies (Alley et al., 2007; Krinner et al., 2007) and ice dynamic modeling (Bamber and Huybrechts, 1996; Huybrechts et al., 2000) use digital elevation models (DEMs) derived from satellite and airborne altimetry. For the grounded part of Dronning Maud Land (DML), these models are not in agreement with each other, at least in coastal Dronning Maud Land (DML).

The area of investigation comprises the two grounded ice tongues of Halvfarryggen and Søråsen (Fig. 1) surrounding the Ekströmisen and reaches inland up to 72.3° S. In the past, this region has been rarely surveyed by

* Corresponding author.
Email address: christine.wesche@awi.de (D. Steinhage).

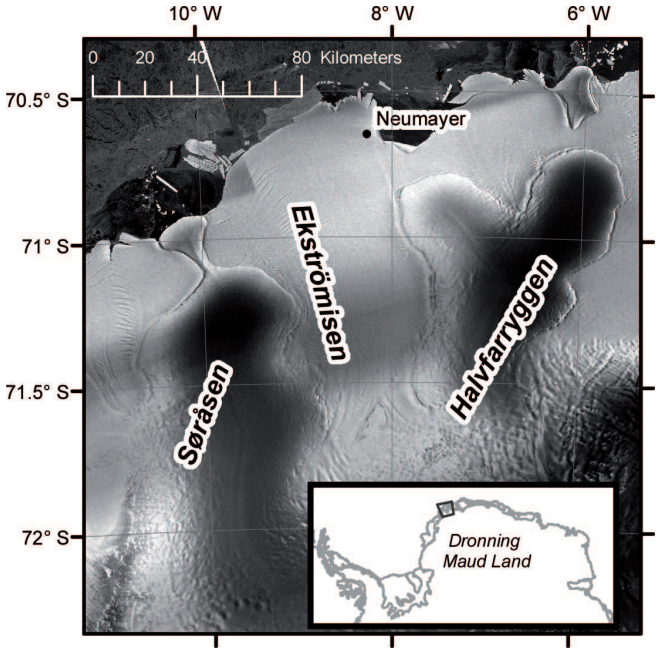

Fig. 1. A RADARSAT image of the investigated area. The black frame in the in-set shows the location of the area of investigation. The satellite picture (RAMP_v2 mosaic - Jezek and RAMP Product Team (2002)) shows a zoom on Halvfarryggen and Søråsen. The shading shows the backscattered intensities converted in grey values between 0 (low backscatter amplitudes) and 255 (high backscatter amplitudes).

ground based measurements, and different currently available DEMs show differences in elevations of several tenths up to hundreds of meters. Kinematic GPS measurements were recorded on Halvfarryggen and Søråsen within the framework of the International Partnerships in Ice Core Sciences (IPICS) pre-site survey for an ice-core drilling and the CryoSat Calibration and Validation activities (Fig. 2). By combining these ground based GPS measurements with laser altimeter measurements from NASA's Ice Cloud and Elevation Satellite (ICESat), airborne radar altimetry (ARA), and radio echo sounding (RES) a precise DEM has been constructed by referencing the remotely sensed data onto the ground based data. In this work, the different data sets were leveled and combined to achieve a DEM of

the area of investigation. The extent of the ice tongues was defined using the grounding line derived from SAR interferometry (pers. comm. R. Drews, 2007). For the north-east flank of Halvfarryggen, the grounding line (dashed grey line) was taken from the Antarctic Digital Database 4.0 (ADD4 - http://www.add.scar.org). To evaluate the quality of the new DEM, a comparison with already existing DEMs is shown later beside a crossover analysis of the various leveled input data.

2 Data and Methods

2.1 Kinematic GPS measurements

The kinematic GPS measurements were recorded during the field campaign in January and February of 2007. A Trimble SSI 4000 GPS receiver was mounted on a snow vehicle which was navigated along predefined tracks at a velocity between 10 and 12 km h^{-1} (Fig. 2 - black lines). Using 1 s observation intervals, the along track distance between the data points is approximately 3 m, which is slightly larger than the length of the vehicle. All kinematic GPS measurements were processed using local reference stations (Tab. 1). The local reference stations (DML94 to DML97, Tab. 1) were non-permanent GPS stations, which provided reference data with a recording interval of 1 s only for local survey period. The position of each local reference station was determined with the aid of the International GNSS Service (IGS) network data and commercial post-processing software, including precise ephemerides, and the ionosphere-free solution. In order to check the stationarity of the local reference stations, a kinematic process-

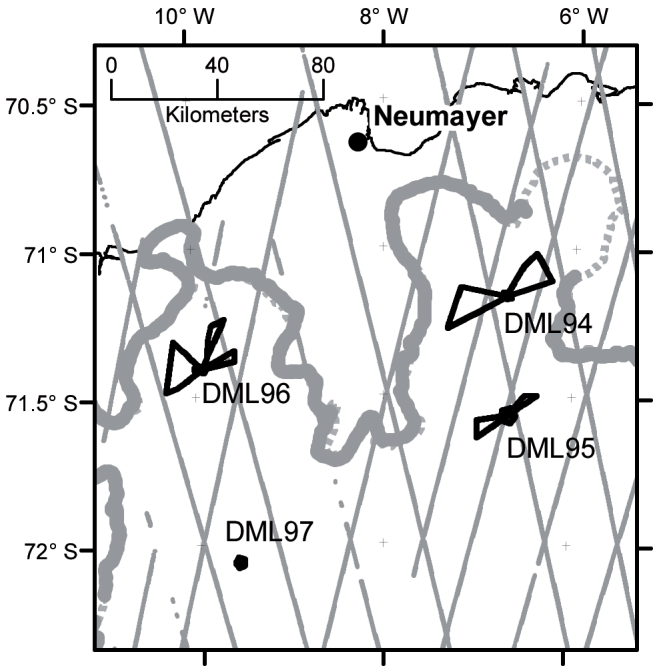

Fig. 2. Coverage of kinematic GPS (black) and ICESat (thin grey) data. The bold grey line represents the grounding line, derived from SAR interferometry (pers. comm. R. Drews, 2007), the dashed grey line is the grounding line which is taken from ADD4 data (http://www.add.scar.org) and the fine black line shows the ice shelf extent also taken from ADD4 data.

ing of the data has been done. The resulting positions are scattered within 2 mm around the averaged position, so stationarity during the survey period can be assumed. The kinematic GPS measurements were processed in kinematic mode in the same manner as the static measurements. The systematic errors have been minimized by using the local reference stations described above (King, 2004). The baselines between the local reference stations and the rover never exceeded 26 km.

A crossover-point analysis was performed to check the uncertainties in the kinematic ground based GPS measurements. The histogram in figure 3 shows the distribution of the elevation differences. Two outliers with an elevation difference greater than 0.1 m are located at the flanks of the profiles,

Table 1

Local reference stations.

station	**longitude**	**latitude**	**elevation [WGS84]**	**period**
DML94	6.6989° W	71.1621° S	690.4 m	14.01.-18.01.07
DML95	6.6670° W	71.5680° S	538.8 m	21.01.-23.01.07
DML96	9.9167° W	71.4083° S	654.6 m	25.01.-30.01.07
DML97	9.5583° W	72.0640° S	760.2 m	31.01.-01.02.07

where the surface roughness is high, which cause large elevation differences. Removing these outliers from further investigations, the mean error at intersection points is 0.03 m with a standard deviation of 0.02 m.

2.2 Satellite laser altimetry

To generate the DEM, the Geoscience Laser Altimetry System (GLAS) onboard NASA's ICESat is used. The GLAS provides, amongst 14 other parameters, ice sheet elevation data (GLA12) between 86° N and 86° S. Altimetry data were received with a 1064 nm laser pulse, with a footprint of about 70 m and an along-track spacing of 172 m. The predicted accuracy of the elevation measurements is 15 cm averaged over the diameter of the footprint (Zwally et al., 2002). Positioning errors are quoted to be 1 arcsec (Schutz et al., 2005). The elevation measurements from the GLAS are referenced to the TOPEX/Poseidon (T/P) ellipsoid, whereas the GPS data refer

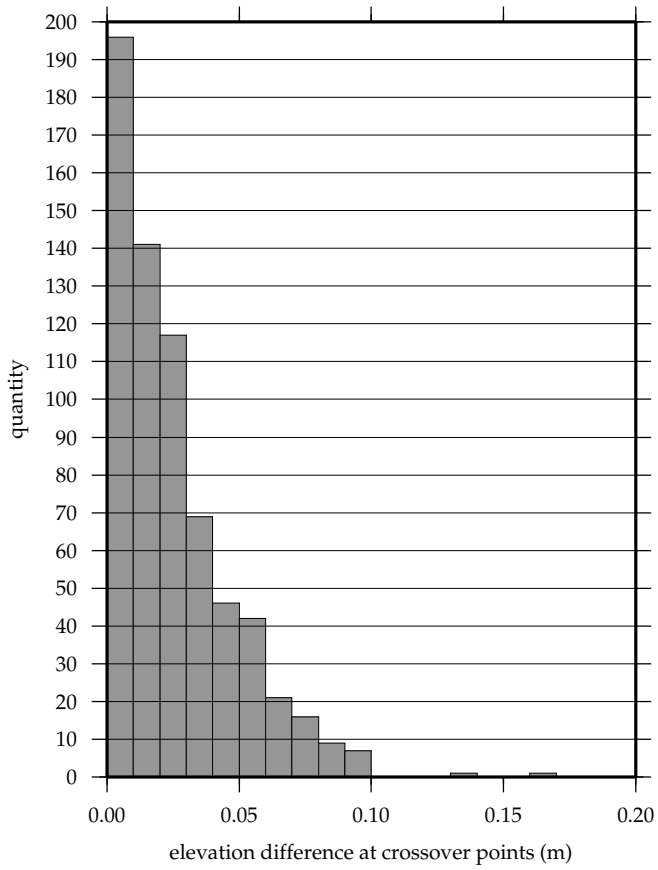

Fig. 3. Histogram of elevation differences at internal crossover points (666) of the ground based kinematic GPS measurements.

to the WGS84 ellipsoid. The minimum difference between these two ellipsoids is 70 cm at the equator and the maximum difference is 71.4 cm at the poles. In the region of interest one can assume that the elevation differences between T/P and WGS84 are approximately 71 cm and the GLA12 elevations have been corrected according to the WGS84 ellipsoid.

The ICESat data included GLA12 Release 28 Laser-3g (2006-10-25 to 2006-11-27) and Laser-3h (2007-03-12 to 2007-04-14) (Zwally et al., 2003) (Fig. 2 - thin grey lines). The altimetry data, provided by the National Snow and Ice Data Center (NSIDC - http://nsidc.org/data/icesat/), were processed with the NSIDC GLAS Altimetry elevation extractor Tool (NGAT).

The main error source for ICESat altimetry data is clouds. Fricker et al.

(2005) show that the quality of ICESat measurements with the 1064 nm laser is highly degraded by cloudy conditions, because the infrared laser pulses were unable to penetrate clouds. The GLA12 data used here were split into ascending and descending ground tracks. A simple script is used, to find and remove elevation leaps greater than 50 m comparing neighbouring data points along track with a maximum space of 500 m between each other. Afterwards, an additional visual check was made. Hence, the cloud degrading factor can be barred from this investigation.

Another accuracy degrading feature is the surface slopes in the region of interest. A 2° slope, combined with the 1 arcsec positioning error results in an elevation error of 10 cm (Martin et al., 2005). Based on the new DEM presented here, the slopes at Halvfarryggen and Søråsen were calculated for 1 km x 1 km grid cells. The GLA12 data were recorded over a mean slope of 0.77° and 77 % of the data points were recorded over slopes smaller than 1°. According to this the slope induced error is between 4 and 5 cm, which has to be added to the predicted elevation accuracy of 15 cm of Zwally et al. (2002). Therefore, the predicted elevation accuracy is about 20 cm on average.

After the cloud correction, crossover-point analyses within and between the various GLA12 laser measurement periods were performed. The arithmetic means of the absolute elevation differences at crossover points of the laser periods are 0.24 m (L3g) and 0.22 m (L3h). For determining the accuracy of a combined GLA12 elevation data set, the number of crossover points, which were involved in determining the arithmetic means above, were used to calculate a weighting factor. The weighted mean of the arithmetic means is calculated, resulting in a crossover error of 0.23 m. For further investigations, the mean of elevations at crossover point is used.

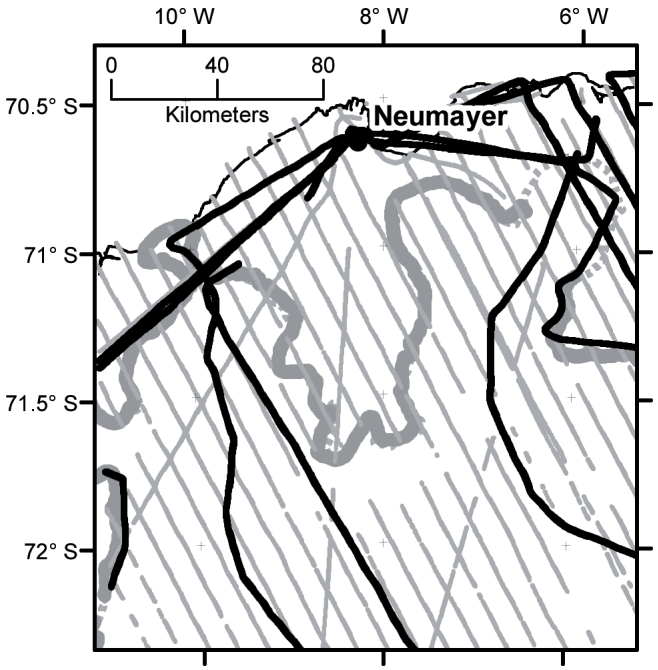

Fig. 4. Coverage of the ARA (black) and RES (thin grey) data. The bold grey line represents the grounding line, derived from SAR interferometry (pers. comm. R. Drews, 2007) and the dashed grey line is the grounding line which is taken from ADD4 data (http://www.add.scar.org) and the fine black line shows the ice shelf extent also taken from ADD4 data.

2.3 Airborne radar altimetry and radio echo sounding

Airborne kinematic GPS combined with ARA and RES provides almost complete coverage for DML. In order to generate a reference DEM of the grounded ice surrounding the Ekströmisen, data from several campaigns (1998/99 to 2004/05 - Fig. 4) were used. The AWI research aircraft POLAR2 is equipped with Trimble SSI 4000 GPS receivers, a HONEYWELL AA-300 radar altimeter (4.3 GHz carrier frequency - ARA) and a RES system operating at 150 MHz, which was specially designed for the use in polar regions (Nixdorf et al., 1999). For generating an elevation model, available post-processed airborne kinematic GPS and ARA data from the campaigns

1998/99 and 2000/01 were used. For this purpose, the radar altimeter data were corrected with regard to the attitude of the aircraft using a modified Airborne SAR Interferometric Altimeter System (ASIRAS) processor (pers. comm. V. Helm, 2006). The derived flight altitude of the aircraft was then subtracted from the GPS height. A crossover-point analysis was performed and results in a mean elevation precision of the ARA measurements of 0.44 m.

On the campaigns for the "Validation, densification, and Interpretation of Satellite data in Antarctica using airborne and groundborne measurements for the determination of gravity field, magnetic field, ice-mass balance, and crustal structure" (VISA) 2001/02 to 2004/05, (see Fig.4), the ARA could not be applied due to the flight level of about 4000 m of the aircraft (the HONEYWELL radar altimeter has an operation altitude of 0 to 760 m above ground). In these cases data from surface reflections of the ice thickness measurements of the RES data were used. A detailed description of the RES equipment is given in Nixdorf et al. (1999). The absolute position of the aircraft is determined from post-processed kinematic GPS data. The distance from the RES antenna to the surface was determined by the onset of the reflected electromagnetic wave (Steinhage et al., 2001) and was then subtracted from the GPS height to obtain the surface topography. This calculation was done for every campaign and by means of crossover-point analyses, the data were leveled to minimize elevation branches between the different campaigns. Afterwards, a second crossover-point analysis of the leveled RES data over grounded ice was made, and an elevation uncertainty of 0.60 m was obtained.

The new DEM is a combination of four different data sets. By using different data sets, the advantages of the data sets could be used to minimize their disadvantages.

In contrast to both satellite based altimetry and ARA/RES, ground based GPS measurements are unaffected by the atmosphere and signal penetration into the snow surface. Furthermore, systematic errors of the ground based GPS measurements have been minimized, by using the short baselines during the post-processing (King, 2004). These represent the best possible surface topography measurements. On this account, the ground based GPS measurements were used as reference elevations. To determine the mean elevation difference between the GPS and the other data sets, crossover-point analyses have been made for leveling. For comparing GPS and GLA12, the elevations of GPS were averaged over the area of the GLA12 footprint (diameter of about 70 m) at crossover points. The analyses result in mean elevation differences of -0.11 m for GPS minus GLA12, 0.78 m for GPS minus ARA and 23.17 m for GPS minus RES.

The GLA12 elevations differences oscillate around the mean difference of -0.11 m with one obvious exception. At one crossover point, the GPS elevation lies 1.46 m above the GLA12 elevation. This crossover point is situated on GLA12 ground track 309. A closer look on track 309 reveals a detrended along track elevation (Fig. 5 - black line). The roughness of the surface (Fig. 5 - black dots) is determined by the subtraction of detrended elevation from the GLA12 elevations, which results in a mean roughness of 0.17 m. The crossover point (Fig. 5 - bold cross) is located in region with a roughness of

0.37 m, which is distinctly above the mean roughness. Additionally, the GPS elevations show a trend within the GLA12 footprint with a difference between maximum and minimum elevation of 1.55 m. This indicates that this crossover point can be regarded as an outlier. It was excluded during the determination of the mean elevations difference to the kinematic GPS data. The GLA12 elevations data were shifted vertically by 0.11 m to level them to the GPS heights. Looking at the mean elevation difference between GPS

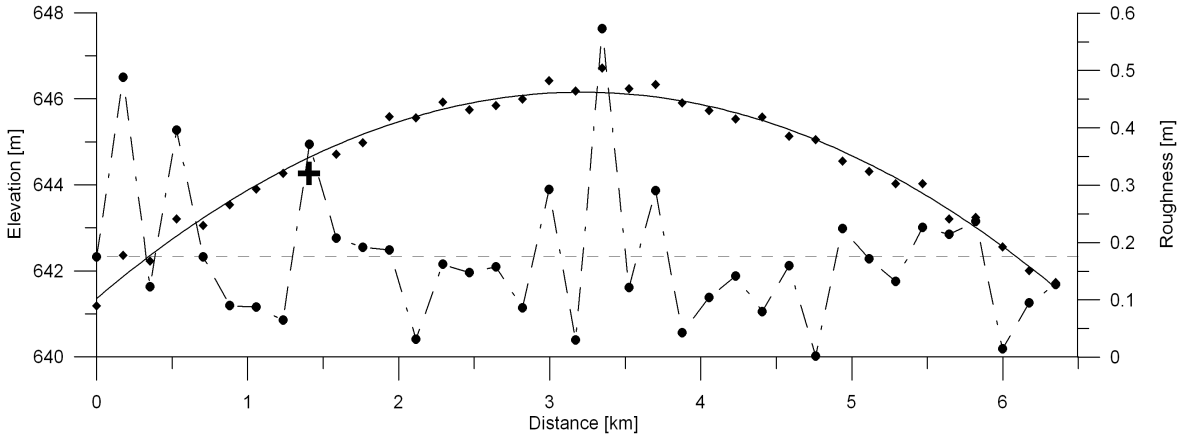

Fig. 5. 2-D profile of GLA12 track 309 (L3g). The plot shows the elevation and the surface roughness against the distance [km] along the ground track elevations (diamonds). The bold cross represents the location of the crossover point between GPS and GLA12. The black line shows the second order polynominal fit to the GLA12 elevations along track. The black dots show the roughness of the surface at the GLA12 ground track and the dashed line the mean roughness along the profile. The dash-dot line shows the direct connection between the roughness dots for better visibility.

and ARA (0.78 m), it can be seen, that the ARA elevations are below the GPS measurements. This can be attributed to the penetration of the radar signal into the snow surface (Ridley and Partington, 1988). In addition, radar altimetry is highly affected by the slope, because the radar signal is not reflected from the nadir point to the antenna, but rather from that point from

the surface, which is nearest to the antenna (Brenner et al., 1983). For this reason the ARA data were filtered for slopes larger than 1.5 °.

The HONEYWELL radar altimeter of the aircraft has a maximum squint angle of 6° in flight direction and this causes a divergence between true and measured elevation at the position of the aircraft. In case the flight direction is inland with increasing elevations, the radar altimeter looks uphill. This results in an error in determining the vertical distance of the aircraft at a particular position to the ground and an error in determining the elevation at this point. If the flight direction is from grounded to floating ice with decreasing elevations, the radar altimeter looks downhill, which results also in large elevation differences.

The elevation differences between GPS and RES data are much larger (23.17 m) than between GPS and ARA data. This is simply due to the fact, that the electromagnetic waves of the RES penetrate deeper into the firn than the higher frequency signal of the ARA (Hofer and Mätzler, 1980). Other limiting factors are on the one hand the small-scale variability in surface properties, which also changes the penetration depth of the signal, and on the other hand the subjective definition of the onset of the surface reflectance signal. These two factors affect the elevation accuracy, but to a minor degree than the penetration depth in total. Both, ARA and RES were leveled to the GPS measurements by the determined mean elevation differences (0.78 m for ARA and 23.17 m for RES).

After these corrections, all data sets were combined into one. The evaluation of crossover points of different periods of GLA12 measurements do not reveal any temporary trend. Therefore, the elevations of the ARA and RES were leveled to the ground based GPS elevations even though they have been acquired in different austral summer seasons. The final data set was

gridded with an Ordinary Kriging (OK) on a 1 km x 1 km grid (Fig. 6). OK is a geostatistical interpolation method, which determines the interpolated value as a function of the distance to neighbouring data points and the associated variance, and relies on the spatial correlation structure to calculate the weighting values during interpolation (Chaplot et al., 2006). Because of

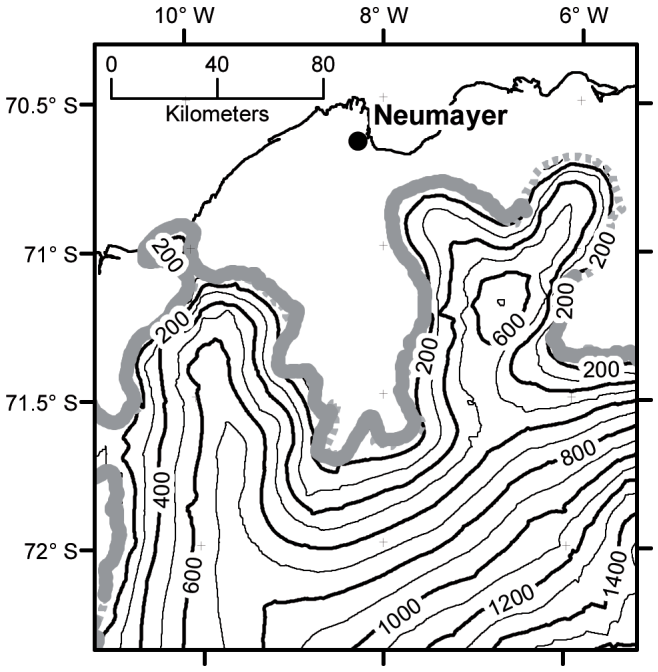

Fig. 6. New DEM of the investigated area. The spacing of the contour lines (black) is 100 m. The bold grey line represents the grounding line, derived from SAR interferometry (pers. comm. R. Drews, 2007) which is complemented by the the dashed grey line from ADD4 data (http://www.add.scar.org). The fine black line shows the ice shelf extent and is also taken from ADD4 data.

the tidal movement and flexure, the ice shelf is not included in this DEM. A reliable model of the tidal flexure of the ice shelf would enable the extension of this work, but the development of such a model lies beyond the scope of this paper. For estimating the accuracy of the DEM presented here, the uncertainties of the different data sets were summed up. The accuracies

are 0.03 m (GPS), 0.23 m (GLA12), 0.44 m (ARA), and 0.60 m (RES). The conservative estimated accuracy of the DEM presented here is therefore 1.30 m.

3 Discussion

Using highly accurate GPS data as elevation reference, resulted in 14 crossover points for validating laser altimetry data from NASA's ICESat. To obtain a larger number of crossover points between non-satellite-based and satellite based data, ARA and airborne RES (leveled to GPS) were used additionally. Though the combination of all data sets, it can be assured, that for every 1 km x 1 km grid cell at least one data point is available. The OK interpolation method yields the best estimations for landscapes with strong spatial structure (Chaplot et al., 2006), like the coastal areas of the Antarctic ice sheet.

In coastal regions, currently existing DEMs show large differences with each other (Bamber and Gomez-Dans, 2005). The focus of comparing the new DEM with existing DEMs relies on two available DEMs, the one from Bamber and Bindschadler (1997) (JLB97) and the Radarsat Antarctic Mapping Project Version 2 (RAMP_v2 1 km resolution) (Liu et al., 2001). While the JLB97 DEM is derived from ERS-1 radar altimetry data, the RAMP_v2 DEM is a combination of different data sets. In the area of investigation the RAMP_v2 elevation data were complemented by data of the ADD4 (http://www.add.scar.org) (Liu et al., 2001). As the DEM presented here focuses on a coastal region, the differences between JLB97 and RAMP_v2 and the new DEM were determined. For the comparison all data was sampled the same grid cell size as the DEM presented here. Afterwards, JLB97 and

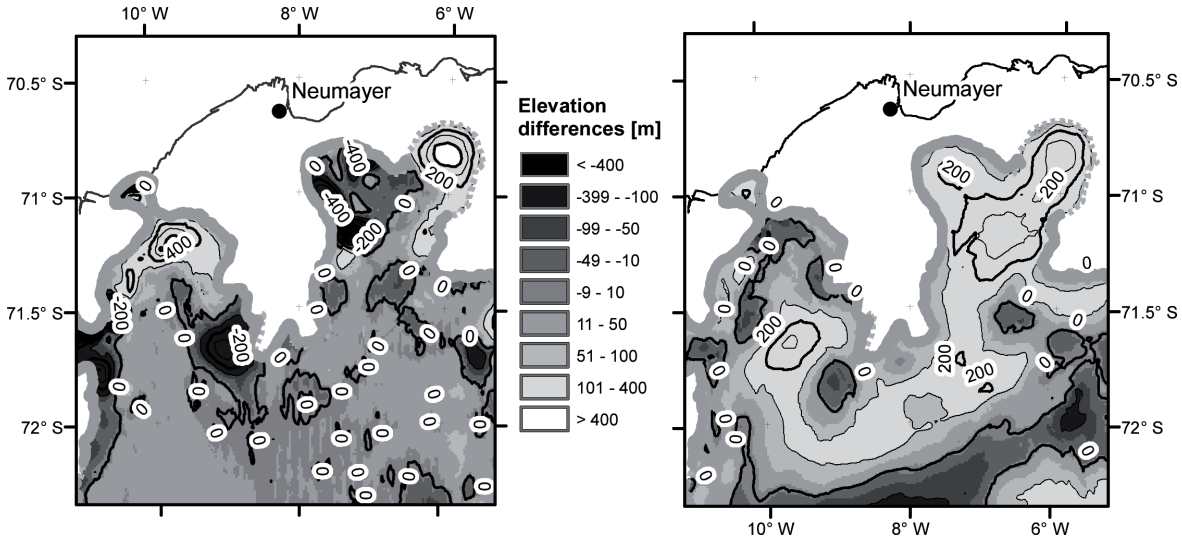

Fig. 7. Map of the elevation differences between the new DEM and JLB97 (left) and new DEM and RAMP_v2 (right). The contour interval is 100 m. The bold grey lines represents the grounding line from SAR interferometry (pers. comm. R. Drews) and the dashed grey line is the grounding line which is taken from ADD4 data (http://www.add.scar.org) and the fine black line shows the ice shelf extent also taken from ADD4 data.

RAMP_v2, were subtracted from the new DEM (Fig. 7). Figure 7 (left) shows the differences between the new DEM and JLB97, and one can see good agreement in the southern part of the investigated area, while the northern parts of Halvfarryggen and Søråsen show large elevation differences. At the eastern flank of Halvfarryggen and the northern part of Søråsen the new DEM is about 400 m higher than JLB97. In some regions in the vicinity of the grounding line, the JLB97 DEM is about 200 m to 400 m higher than the newly derived DEM. At the margins of Halvfarryggen and Søråsen, the slopes are larger than 1° and the elevation difference and its standard deviation increases with the slope (slope-induces error (Brenner et al., 1983)). The negative elevation differences can be attributed to this error. The reason for the large positive differences between this new DEM and JLB97 at the

east flank of Halvfarryggen and Søråsen can not be explained.

In figure 7 (right) RAMP_v2 DEM was subtracted from the newly derived DEM. The highest differences are about 300 m in large parts of Halvfarryggen and the southern part of Søråsen. The new DEM and RAMP_v2 agree only with each other in small parts of the grounded ice in the south of the investigated area. As mentioned before, in the region of interest the RAMP_v2 DEM is supplemented with ADD4 data (Liu et al., 2001). Bamber and Gomez-Dans (2005) compared the RAMP_v2 DEM with GLA12 and found, that the errors in the coastal regions of the ice sheet are in the order of ± 100 m. This investigation shows, that the discrepancies are even more, between -200 m to 300 m.

4 Conclusion

The usage of remote sensing data (especially for altimetry) requires ground based data for validation. The coastal regions of the Antarctic continent are not well covered with ground based elevation measurements, but in combination with airborne data, reliable reference measurements for satellite data are available. The new DEM is a combination of ground based GPS measurements, airborne, and satellite altimetry. By combining different data sets the inherent errors of the single data sets can be reduced by taking advantage of the unique features of the individual data sets, and an accurate DEM can be constructed.

Airborne and satellite data have to be validated with ground based measurements, especially in sloped regions, where airborne and satellite altimetry is imprecise due to the prevailing surface slopes. A combination

of ground based measurements with remote sensing data provides sufficient data coverage for the construction of a reliable digital elevation model of the surface topography.

Comparisons with already existing DEMs show large elevation differences on Halvfarryggen and Søråsen. Current available DEMs do not provide the accuracy requirements for reliable ice sheet modeling, because they show very high elevation differences with each other in coastal regions. By using highly accurate ground based GPS data as true reference elevations, the approximation of the real surface of the DEM presented here is much higher than at the RAMP_v2 DEM. JLB97 shows, apart from Halvfarryggen and Søråsen, a very good agreement with the new DEM.

The aim is to generate an accurate DEM of whole DML from geophysical data sets. Both mass balance studies and ice dynamic modeling with respect to the sea level change and paleoclimatic reconstruction, will benefit from the in the future derived and improved surface topography.

5 Acknowledgement

The authors thank Dr. Doris and Martin Bertges for their support. Preparation of this work was supported by the Bundesministerium für Wirtschaft (BMWi) through the CryoVEx activities 50EE0505. The airborne data mapped within the VISA project were supported by Deutsche Forschungsgemeinschaft (DFG), founded under grants Di 473/17-1 and Jo 191/8-1. Thanks to the National Snow and Ice Data Center (NSIDC) for providing the ICESat data, the NGAT elevation extraction tool and the RAMP_v2 data.

The authors also thank the editor O. Hellwich and the two anonymous reviewers for their helpful comments.

References

Abdalati, W., Krabill, W., Frederick, E., Manizade, S., Martin, C., Sonntag, J., Swift, R., Thomas, R., Wright, W., Yungel, J., 2002. Airborne laser altimetry mapping of the Greenland ice sheet: application to mass balance assessment. Journal of Geodynamics 34, 391–403.

Alley, R. B., Spencer, M. K., Anandakrishnan, S., 2007. Ice-sheet mass balance: assessment, attribution and prognosis. Annals of Glaciology 46, 1–7.

Bamber, J. L., Bindschadler, R. A., 1997. An improved elevation dataset for climate and ice-sheet modelling: validation with satellite imagery. Annals of Glaciology 25, 439–444.

Bamber, J. L., Gomez-Dans, J. L., 2005. The accuracy of digital elevation models of the Antarctic continent. Earth and Planetary Science Letters 237, 516–523.

Bamber, J. L., Huybrechts, P., 1996. Geometric boundary conditions for modelling the velocity field of the Antarctic ice sheet. Annals of Glaciology 23, 364–373.

Brenner, A. C., Bindschadler, R. A., Thomas, R. H., Zwally, H. J., 1983. Slope-induced errors in radar altimetry over continental ice sheets. Journal of Geophysical Research 88 (C3), 1617–1623.

Chaplot, V., Darboux, F., Bourennane, H., Leguedois, S., Silvera, N., Phachomphon, K., 2006. Accuracy of interpolation techniques for the derivation of digital elevation models in relation to landform types and data density. Geomorphology 77, 126–141.

Fricker, H. A., Borsa, A., Minster, B., Carabajal, C., Quinn, K., Bills, B., 2005. Assessment of ICESat performance at the salar de Uyuni, Bolivia. Geophysical Research Letters 32 (L21S06).

Hofer, R., Mätzler, C., 1980. Investigations of snow parameters by radiometry in the 3-to 60-mm wavelength region. Journal of Geophysical Research 85 (C1), 453–459.

Huybrechts, P., Steinhage, D., Wilhelms, F., Bamber, J., 2000. Balance velocities and measured properties of the Antarctic ice sheet from a new compilation of gridded data for modeling. Annals of Glaciology 30, 52–60.

Jezek, K., RAMP Product Team, 2002. RAMP AMM-1 SAR Image Mosaic of Antarctica. Fairbanks, AK Alaska Satellite Facility, in association with the National Snow and Ice Data Center, Boulder, CO, Digital media.

King, M., 2004. Rigorous GPS data-processing strategies for glaciological applications. Journal of Glaciology 50 (171), 601–607.

Krinner, G., Magand, O., Simmonds, I., Genthon, C., Dufresne, J.-L., 2007. Simulated Antarcitc precipitation and surface mass balance at the end of the twentieth and twnty-first centuries. Climate Dynamics 28, 215–230.

Liu, H., Jezek, K. C., Li, B., Zhao, Z., 2001. Radarsat antarctic mapping project digital elevation model version 2. Boulder CO National Snow and Ice Data Center, Digital media.

Martin, C. F., Thomas, R. H., Krabill, W. B., Manizade, S. S., 2005. ICESAT range and mounting bias estimation over precisely-surveyed terrain. Geophysical Research Letters 32 (L21S07), doi:10.1029/2005GL023800.

Massom, R., Lubin, D., 2006. Polar Remote Sensing. Vol. II Ice Sheets. Springer Verlag, Berlin Heidelberg New York.

Nixdorf, U., Steinhage, D., Meyer, U., Hempel, L., Jenett, M., Wachs, P., Miller, H., 1999. The newly developed airborne radio-echo sounding sys-

tem of the AWI as a glaciological tool. Annals of Glaciology 29, 231–238.

Ridley, J. K., Partington, K. C., 1988. A model of satellite radar altimeter return from ice sheets. International Journal of Remote Sensing 9 (4), 601–624.

Schutz, B. E., Zwally, H. J., Shuman, C. A., Hancock, D., DiMarzio, J. P., 2005. Overview of the ICESat Mission. Geophysical Research Letters 32 (L21S01), doi:10.1029/2005GL024009.

Steinhage, D., Nixdorf, U., Meyer, U., Miller, H., 2001. Subglacial topography and internal structure of central and western Dronning Maud Land, Antarctica, determined from airborne radio echo sounding. Journal of Applied Geophysics 47, 183–189.

Wingham, D., Ridcout, A., Scharroo, R., Arthern, R., Shum, C., 1998. Antarctic elevation change from 1992 to 1996. Science 282, 456–458.

Zwally, H., Schutz, B., Abdalati, W., Abshire, J., Bentley, C., Brenner, A., Bufton, J., Dezio, J., Hancock, D., Harding, D., Herring, T., Minster, B., Quinn, K., Palm, S., Spinhirne, J., Thomas, R., 2002. ICESat's laser measurements of polar ice, atmosphere, ocean, and land. Journal of Geodynamics 34, 405–445.

Zwally, H. J., Schutz, R., Bentley, C., Bufton, T., Herring, T., Minster, J., Spinhirne, J., Thomas, R., 2003. GLAS/ICESat L2 Antarctic and Greenland Ice Sheet Altimetry Data V001. Boulder, CO National Snow and Ice Data Center, Digital media.

PAPER III

An improved DEM and refined ice divides location for central Dronning Maud Land, Antarctica

In review at Journal of Glaciology

An improved DEM and refined ice divides location for Dronning Maud Land, Antarctica

Christine Wesche[1], Sven Riedel[1,2], Daniel Steinhage[1], Olaf Eisen[1] and Hans Oerter[1]

[1] *Alfred Wegener Institute for Polar and Marine Research, Bremerhaven, Germany*

[2] *Institute for Geosciences, Division Geophysics, Christian Albrechts University, Kiel, Germany*

email: christine.wesche@awi.de

ABSTRACT. The knowledge of ice sheet surface topography and the location of the ice divides are essential for ice dynamic modeling. An improved digital elevation model (DEM) of Dronning Maud Land (DML), Antarctica, is presented in this paper. It is based on ground-based kinematic GPS profiles, airborne radar altimetry, and data of the airborne radio-echo sounding system, as well as spaceborne laser altimetry from NASA's Ice, Cloud and land Elevation Satellite (ICESat). The accuracy of ICESat ice sheet altimetry data in the area of investigation is discussed. The location of the ice divides is derived from aspect calculation of the topography and is verified with several velocity data derived from repeated static GPS measurements.

INTRODUCTION

The knowledge of the present state of the Antarctic ice sheet is essential for an accurate interpretation of ice cores as well as for modeling of ice dynamic processes. A comparison of the digital elevation models (DEMs) of Bamber and Bindschadler (1997) (JLB97) and Liu and others (2001) (RAMP Version 2) shows elevation differences of up to several hundred meters in the region north of the coastal mountains of Dronning Maud Land (DML), which yield in different results using these DEMs for calculating ice volumes. The ice volume will strongly affect future sea-level modeling (Clark and Mix, 2002; Huybrechts, 2003) and thus the need of an improved elevation model in this area is obvious.

Ice cores are favourably drilled near low-velocity zones as ice divides or ice domes. The construction of the velocity field requires accurate knowledge of the ice divide position, because of high sensitivity of the transition from divide flow to flank flow at an ice divide. The interpretation, e.g. agemodel, of the deep ice core (EDML), drilled within the European Project for Ice Coring in Antarctica (EPICA) near the German summer station Kohnen (0.0667° E, 75.0018° S) (Wesche and others, 2007) will be improved by taking into account the new derived ice divide position presented here, because Kohnen station is located between two ice divides, which fork in the east of the station. Therefore, the position of the forking and the course of the two ice divides are of particular interest.

In this work, an improved digital elevation model (DEM) of DML is generated from several ground-based kinematic GPS measurements, airborne altimetry data and satellite laser altimetry data. Based on the new surface topography and an extended as to Wesche and others (2007) net of point measurements of the surface flow velocity, the location of the ice divides is determined.

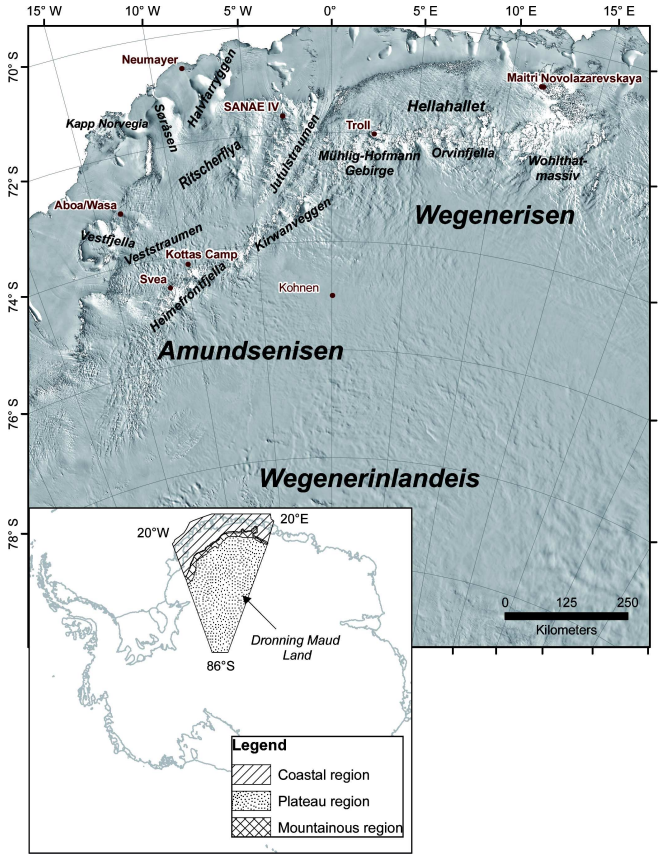

Fig. 1. Map of Dronning Maud Land. The area of investigation and its separation in three parts is shown in the overview map of Antarctica. The grounding and coast lines are taken from MODIS Mosaic of Antarctica (MOA) (Haran and others, 2006).

DATA AND METHODS

The improved DEM was generated from a combination of different data sets: (i) ground-based kinematic GPS data, which provide the best approximation to the true surface elevation, (ii) airborne altimetry from several surveys, and (iii) laser altimeter measurements of NASA's Ice, Cloud, and land Elevation Satellite (ICESat). In addition to the elevation data, flow velocities in the plateau region were determined from repeated static GPS measurements to verify the (re-)location of the ice divides in central DML. In the following sections an introduction to the data sets and their accuracy is given.

Satellite laser altimetry

ICESat is equipped with the Geoscience Laser Altimety System (GLAS), which provides worldwide altimetry and atmospheric data. For generating the DEM, the ice sheet altimetry data (GLA12) release 28 were used (Zwally and others, 2007). The footprint of the GLAS is about 70 m and the elevation data are averaged over this region. For a detailed description of GLAS see Zwally and others (2002) and Brenner and others (2003).

The GLA12 elevation data were corrected for detector saturation from returned pulse energy (Fricker and others, 2005) and for ocean tides using the global ocean tide model GOT99.2 (Ray, 1999). This tide model does not perform well around Antarctica, whereas the TPXO6.2 global tide model (Egbert and Erofeeva, 2002) is the best available model for this region (King and Padmann, 2005). Therefore, the routinely applied tide correction was removed and the actual release TPXO7.1

Table 1. Absolute mean elevation differences and standard deviations of GLA12 data at crossover points given in meters. Numbers of crossover points are given in brackets. The mean in the last line is the pooled mean elevation difference.

Laser	Period	Coast	Mountain	Plateau
Laser3g	2006-10-25 to 2006-11-27	0.73± 0.71 m (236)	0.84± 1.08 m (161)	0.16± 0.25 m (20342)
Laser3h	2007-03-12 to 2007-04-14	0.68± 1.97 m (154)	0.82± 1.33 m (72)	0.14± 0.17 m (12732)
Mean		**0.70 m**	**0.83 m**	**0.15 m**

global ocean tide model was applied. In the next step the data were divided into three parts, the coastal region (north of the coastal mountain range, Fig. 1 diagonal banded area), the mountainous region (separating the coastal region from the interior, Fig. 1 checkered area) and the plateau region (south of the coastal mountain range, Fig. 1 irregular dotted area). The elevation differences within every single data set were determined by crossover-point analyses. The search diameter of comparable elevations is equal the footprint of 70 m. The internal accuracies of the laser periods are given in Table 1. It summarizes the elevation differences of the GLA12 measurements, which are varying depending on the investigated area and laser period. The predicted elevation accuracy of 0.15 m (Zwally and others, 2002) was only achieved for the plateau region with a mean slope of 0.16± 0.14°. The slope was calculated from the surface topography with a cell size of 2.5 km × 2.5 km. For the coastal region (mean slope 0.75± 0.51°) and the mountainous region (mean slope 1± 1.10°), the mean absolute elevation differences (here accuracy) are about four to five times higher. Plotting the 3-sigma corrected elevation differences (all elevation differences larger than 3-sigma were removed to avoid outliers) against the slope (Fig. 2) there is no slope dependence for elevation differences at crossover points visible.

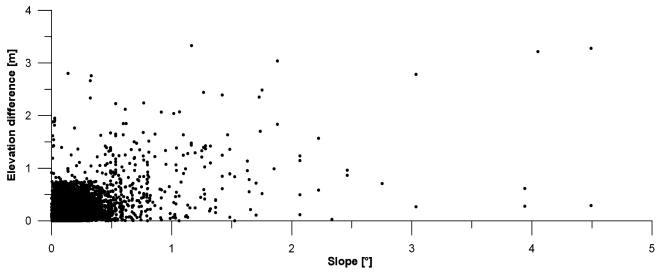

Fig. 2. 3-sigma corrected elevation differences of the L3g and L3h GLA12 measurements against the slope, which is averaged over 2.5 km^2.

The coefficient of determination is 0.19, which means that only 19% of the elevation differences can be explained by the slope. Quite another picture shows Figure 3, where standard deviation of the elevation differences in the separated regions (coastal, mountainous and plateau) for laser periods L3g and L3h (Fig. 3(A)) are shown. The standard deviations are larger in the regions with higher mean slopes, but there are also variations in the two laser periods. It can not be confirmed that in the mountainous region (mean slope of 1°) are always the largest standard deviations of the elevation differences. A similar picture is shown in Figure 3 (B). The mean elevation differences at crossover points for four slope classes are variable with the laser period. The smallest mean elevation difference is always in low slope regions below

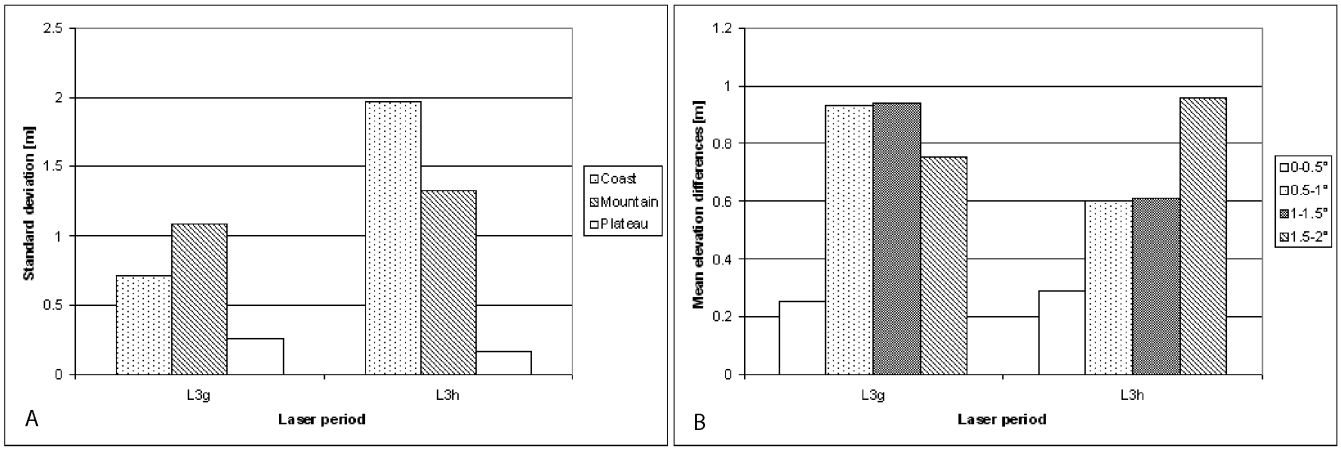

Fig. 3. Bar charts showing the GLA12 L3g and L3h standard deviation of the elevation differences with regard to the investigation area (A) and the mean elevation differences for different slopes (B).

0.5°, but apart from this the largest mean elevation differences are not necessarily in regions with slopes between 1.5 and 2°.

Airborne altimetry data

In this work, two different airborne based altimetry data sets are used. Basic purpose of both is to determine the altitude of aircraft above the snow surface, which is later subtracted from the derived GPS height of the flight track. The data were recorded between 1998 and 2005 and are a by-product of the pre-site survey of the EDML deep-drilling site and the VISA (Validation, densification, and Interpretation of Satellite data in Antarctica using airborne and groundborne measurements for the determination of gravity field, magnetic field, ice-mass balance and crustal structure) survey. The radar signal is its independence from weather conditions. This advantage makes them a good supplementation to ground-based kinematic GPS and spaceborne laser altimetry.

The on-board HONEYWELL-AA 300 radar altimeter (4.3 GHz carrier frequency) has an operational altitude of 760 m above ground (Honeywell AA-300 Manual, 1998), for that reason the airborne radar altimetry (ARA) data are only available for the campaigns 1998/99 and 2000/01. During gravimetry measurements within the VISA project (between 2001 and 2005), the altitude during the flight was between 3600 and 4800 m a.s.l., and thus mostly too high for useable ARA data. Therefore, the radio echo sounding (RES) data are used. The RES system (150 MHz carrier frequency) was actually designed for ice thickness measurements. The reflection of the pulse at the air-ice interface yields in a surface response of the signal, because of the different velocity of propagation of the radar signal in air and ice. An overview of the data coverage is given in Figure 4.

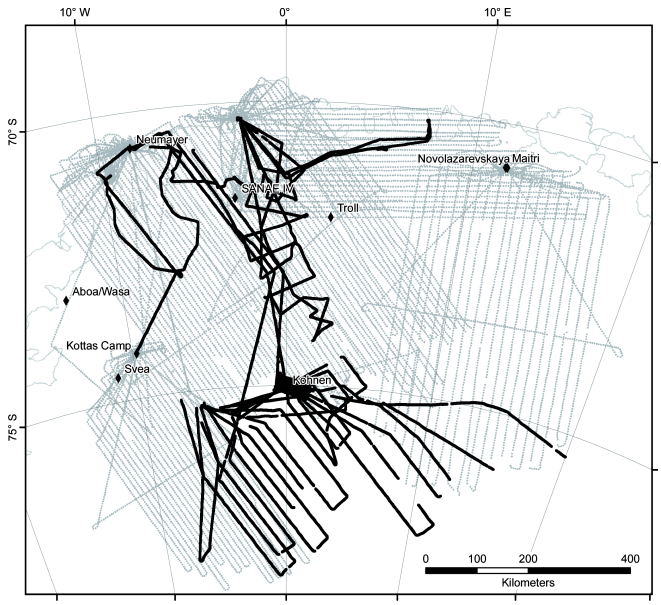

Fig. 4. The coverage of airborne altimetry data. The black lines representing the ARA and the grey lines are the RES flight lines. Grounding and coast lines are taken from MOA (Haran and others, 2006).

Not for all RES flight lines elevation data are available. To minimize the slope-induced error all ARA data, recorded over a slope higher than 1.5°, were removed (4.5%). Thus, the maximum theoretical slope-induced error is about 0.26 m (determined by the equation given in Brenner and others (1983)).

Kinematic GPS measurements

Three different kinematic GPS data sets were used. For two of them, a Trimble SSi4000 GPS receiver was mounted on a snow vehicle, which was navigated along pre-defined tracks in austral summer season 2000/01 near the German summer station Kohnen (0.07° E, 75.00° S) and in the vicinity of the German overwintering station Neumayer (8.25° W, 70.65° S) in January and February 2007 (Wesche and others, 2007, submitted). These profiles were processed with local reference stations (Fig. 5, black lines) to shorten the baselines between the reference and the rover. This improves data quality by reducing systematic errors (King, 2004). Kinematic GPS profiles in the hinterland of Neumayer station, processed with remote reference stations, were added (Fig. 5, grey lines). The accurate positions of these profiles were determined by using the data of the permanent reference station Vesleskarvet near the South African station SANAE IV or the Finnish station Aboa (Fig. 1 and 5).

Because the recording interval at the reference stations is 30 s (Vesleskarvet) or 15 s (Aboa), these data were interpolated to an interval of 1 s to retain the data density of the ground-based GPS data, which were recorded with an interval of 1 s. The software tool INTERPO of the National Geodetic Survey (NGS) offers the possibility to resample the data of the remote reference stations. After processing all GPS data located on the Ekström ice shelf were corrected for ocean tides with the TPXO7.1 model (Egbert and Erofeeva, 2002).

The accuracy (mean absolute elevation difference) of every single data set was determined with crossover-point analyses. The analyses revealed an accuracy of 0.03 m for the measurements using local references and 0.06 m for the coastal measurements using Vesleskarvet. Unfortunately, there are no crossover points within the traverse data, therefore only

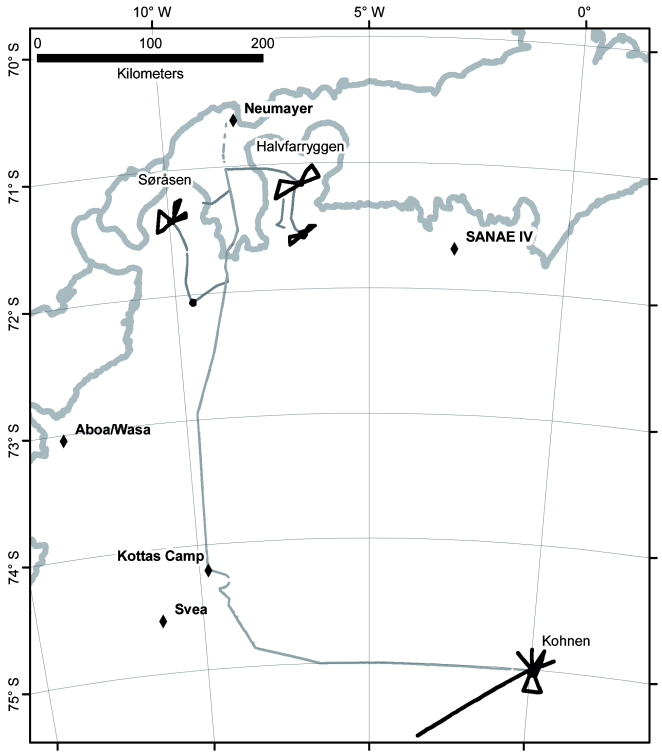

Fig. 5. Coverage of kinematic GPS data. The black lines represent the GPS profiles processed with a local reference station (Wesche and others, 2007, submitted), the grey lines indicate profiles processed with remote reference stations. The grounding and coast lines (bold grey) are taken from MOA (Haran and others, 2006).

the quality check of the post-processing software GrafNav (Waypoint) gives an estimate of the accuracy. According to the software's quality check, all data points with an accuracy worse than 1.0 m were removed.

Static GPS measurements

Repeated static GPS measurements were made in DML over several years using aluminium stakes as marker. Firstly, the purpose of static GPS measurements is the usage as a local reference station and secondly, to determine the surface velocity. Such an approach is presented in Wesche and others (2007) and five new velocity measurements are presented here.

The post-processing of the static GPS data was done using several reference stations, precise ephemerides and ionospheric-free solution. Local reference stations were used for the determination of the stake positions. Thirteen velocity-point measurements in the direct vicinity of the German Kohnen station were already presented in Wesche and others (2007). The five additional velocities measurements are shown in Table 2. A detailed description of the accuracy estimation procedure of 0.06 m a^{-1} of the static GPS data is given in Wesche and others (2007).

An improved DEM for DML

The investigations described here were made for the three regions, presented in relation to the satellite altimetry data. The new DEM is a combination of four different data sets. The ground-based kinematic GPS data are the best approximation to the real surface topography and were used as reference elevations. Several crossover-point analyses were performed to level the remotely sensed data to the ground-based GPS data. First of all, the error induced by the penetration of the ARA

Table 2. The flow velocities of various point measurements on the Antarctic plateau. The positions are available in the PANGAEA database (doi: xxx)

Name	Longitude	Latitude	Surface flow [m a^{-1}]	Flow direction [°]	Period of averaging
DML01	2.5493° E	74.8564° S	0.54	293.2	Jan. 1997 - Jan. 1999
DML02	3.9185° E	74.9683° S	3.18	153.5	Jan. 1997 - Jan. 1999
DML03	1.9609° E	74.4995° S	7.40	128.9	Jan. 1997 - Jan. 1999
DML07	3.4306° W	75.5816° S	4.28	229.6	Jan. 1997 - Jan. 2001
DML19	0.9951° W	75.1674° S	1.87	213.3	Jan. 1999 - Jan. 2001

signal into the snow surface is determined by a crossover-point analysis with the ground-based GPS data, which is 2.25 m on the plateau and 2.28 m in the coastal region. The ARA data were then shifted by these values. Indeed, the penetration depth of the ARA signal has a spatial variation, but the GLA12 data are highly affected by surface fog or surface snow drift, which cannot be avoided completely. Thus a crossover-point analysis between the ARA (previously shifted to the GPS data) and GLA12 was performed and resulted in elevation differences at crossover points, which are below the data sets accuracy. Therefore, the GLA12 data were not leveled to the ARA data. Because of the lower frequency, the penetration depth of the RES data is higher than the one of the ARA signal (Rott and others, 1993). A crossover-point analysis between these two data sets resulted in elevation differences of 21.97 m in the coastal region, 25.35 m in the mountainous region, and 24.02 m at the plateau. The RES data were shifted by these values.

Afterwards, the corrected data sets were merged into data sets for the coastal, mountainous and plateau region. Each spatial data set was interpolated with the "Ordinary Kriging" routine on a 2.5 km x 2.5 km raster and mosaiced to the final improved DEM for central DML (Fig. 6).

RESULTS AND DISCUSSION

The improved DEM is a result of four different elevation data sets, they all have different accuracies and spatial coverage. Because the above presented ground-based kinematic GPS data have a vertical accuracy of 0.03 m and were not affected by weather conditions and penetration of the signal into the surface, they are used as reference to determine the accuracy of the final improved DEM at two locations. For this purpose, the elevation differences between the DEM and the ground-based kinematic GPS data (processed with local reference stations - black lines in Fig. 5) are calculated. To this end heights within a raster cell of the DEM were averaged. In the coastal region, the heights of the leaf-like profiles in Figure 5 were used. The elevation differences are varying between -33.49 and 58.29 m with a mean of -2.66 m and a mean standard deviation within the raster cells of 4.45 m. The maximum and minimum elevation differences are quite large, but this can be contributed to the smoothing effect of the interpolation. The slopes in the coastal region were flattened by the interpolation. The mean standard deviation is also large, which is caused by the resolution of 2.5 km $\times$ 2.5 km of the DEM. The GPS heights are varying within a raster cell and show a rough surface (Fig. 7 A). The roughness is calculated over 2.5 km by the absolute difference of the GPS derived surface elevation to a calculated fit (70 m running average). The surface in the coastal region has a mean roughness of 0.1 m with a maximum of 0.4 m. But what is clearly shown is, that the elevation of the GPS data decreases by about 14 m, which is the main reason for the large standard deviation of the GPS

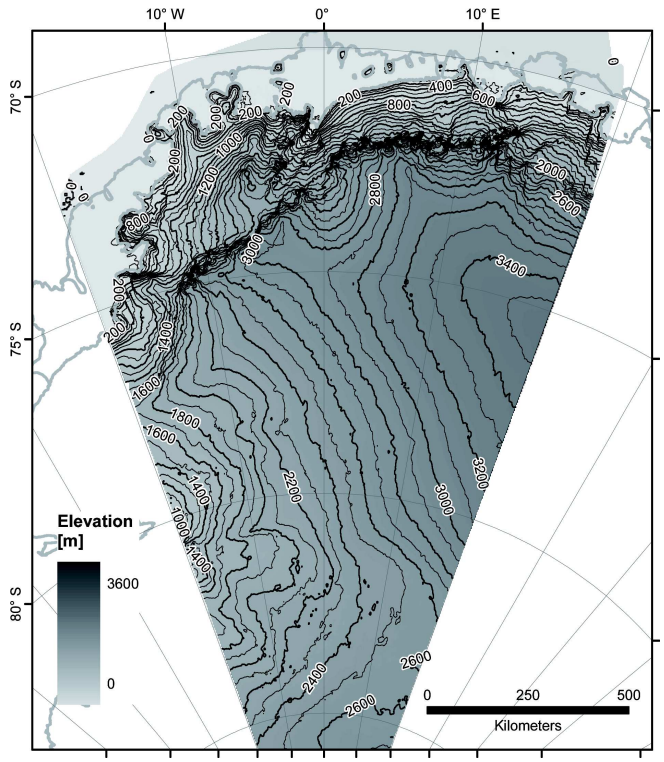

Fig. 6. The improved DEM for DML. The spacing of the contour lines is 100 m. Grounding line and the coast line, represented as a bold grey lines, are taken from MOA (Haran and others, 2006).

height within the 2.5 km × 2.5 km raster cell. On the plateau, the ground-based kinematic GPS data in the vicinity of the Kohnen station were used. The mean elevation differences averaged over a 2.5 km raster cell is -0.65 m with a maximum of 0.11 m and a minimum of -1.77 m. The mean standard deviation within a raster cell is 0.26 m. As demonstrated in Figure 7 B, the surface measured with the ground-based GPS is flat (variation of 0.4 m) and the roughness is very small (mean roughness is 0.03 m). The mean elevation differences show a very good agreement of the improved DEM to the highly accurate ground-based GPS data.

For comparing the improved DEM presented here with commonly used DEMs (JLB97 and RAMP) the volume differences are used. The differences were calculated by the difference in elevation.

The volume differences purports, that the differences between the improved DEM and the commonly used DEMs (JLB97 and RAMP) are not very large. But a direct comparison of the elevation differences shows that the differences can reach up to several hundreds of meter (Fig. 8 A to F).

Table 3. Volume differences between the improved DEM and JLB97 and RAMP, respectively.

DEM	Coast Difference	Mountain Difference	Plateau Difference
RAMP	+2976 km^3	+1903 km^3	-47145 km^3
JLB97	-339 km^3	+1448 km^3	-17234 km^3

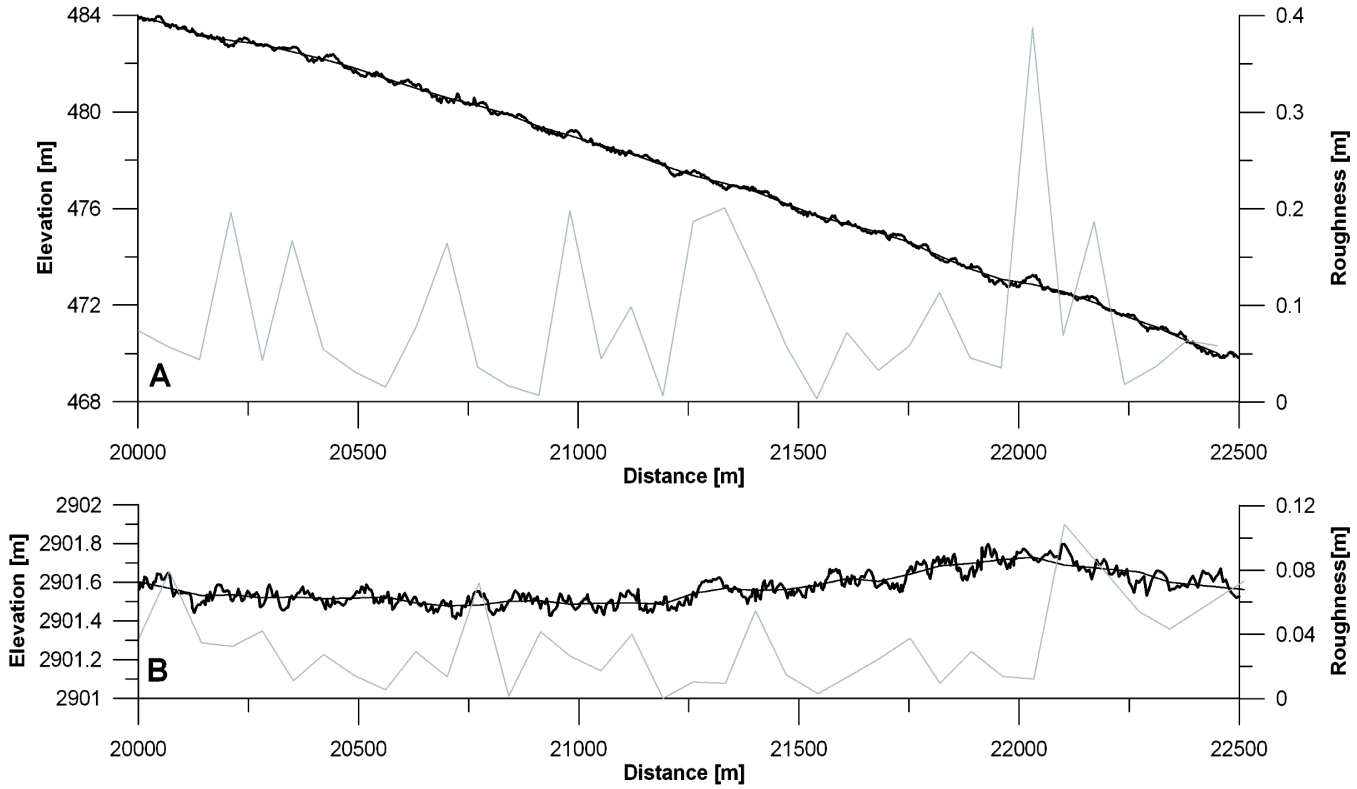

Fig. 7. The elevations along a distance of 2.5 km (thick black lines) in the coastal region (A) and in the plateau region (B). The thin black lines show the 70 m running average to the elevation data and the grey line shows the roughness of the surface. Note: The elevations and roughnesses of the surface have different scales.

The histograms in Figure 8 show different distributions of the elevation differences. Because the JLB97 has a resolution of 5 km $\times$ 5 km the improved DEM was sampled on this cell size. The other way around, the RAMP DEM has a higher resolution than the new DEM, so it was sampled down to a cell size of 2.5 km $\times$ 2.5 km. Figure 8 A shows, compared to D, a narrow peak of elevation differences and the number of differences above 100 m and below -100 m is also smaller. In the coastal region the RAMP DEM (Figure 8 B) shows higher elevation differences and a slightly shift to the negative differences. This can be attributed to the use of large scale topographic maps for generating the RAMP DEM. The elevation differences between the new DEM and JLB97 can be explained by the slope-induced error (Brenner and others, 1983). In the mountainous region the elevation differences between the improved DEM and JLB97 and RAMP, respectively, show a similar distribution. Also in this case, the distribution of the differences between the improved DEM and RAMP is wider than the distribution obtained from the comparison with the JLB97 DEM. But both show elevation differences up to $\pm$ 600 m. A wider distribution of elevation differences calculated using the RAMP DEM can also be found in the plateau region (Fig. 8 F). There is one prominent peak representing elevation differences between zero and five meter. Apart from that there is a flat distribution. Elevation differences calculated using JLB97 (Fig. 8 C) show a wide maximum and a rapid decrease of quantity. The large differences in the plateau region are basically in the area south of 81.5° S. In this region, the RAMP DEM consists of airborne altimetry, with a precision of $\pm$ 50 m (Liu and others, 2001).

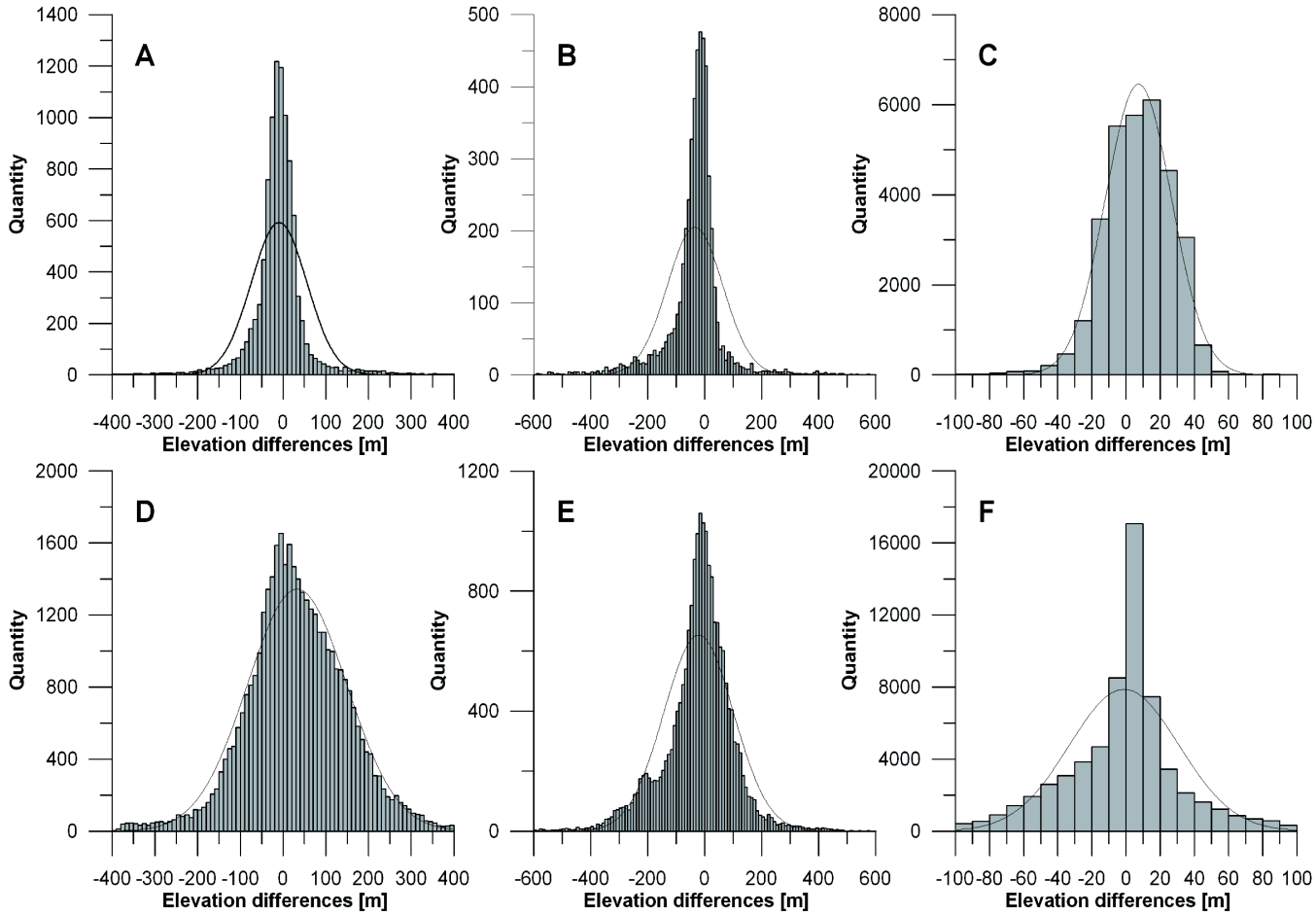

Fig. 8. Histograms of elevations differences between the improved DEM and JLB97 (A-C) and RAMP (D-F) for the three investigation regions (coastal region A and D, mountainous region B and E and plateau region C and F). The thin black lines are the Gaussian fits of the elevation difference distributions.

(Re-)location of the ice divides in central DML

An ice divide separates two neighboring catchment areas. The topographic ice divide, on which is focussed here, is located on the highest surface elevation along a cross section of the DEM. The flow regime near an ice divide is characterized by slow parallel flow along the course of the ice divide. This effect can be found up to three to five times of the ice thickness apart from its course (Raymond, 1983; van der Veen, 1999). With increasing distance to the divide, the flow velocity becomes less affected and the ice flows more divergent to the course. Ice divides and domes are preferred ice-core drilling locations, because of their the minimally disturbed internal layering, which simplifies the paleoclimatic interpretation of the ice (Raymond, 1983).

In this work, the locations of the ice divides in DML are derived by the improved DEM and the calculated aspect of the topography in DML (Fig. 9). The "old" ice divide (Fig. 9 - grey dashed line) was derived from the DEM of Bamber and Huybrechts (1996) which has a resolution of 5 km $\times$ 5 km. In most parts, the courses of the "old" and new ice divides are less than 5 km apart from each other, which is about 1.5 to 2 times the ice thickness. In the east of the region of interest, one position of an ice divide cannot be confirmed, in return a more western one is found. In the coastal region, a

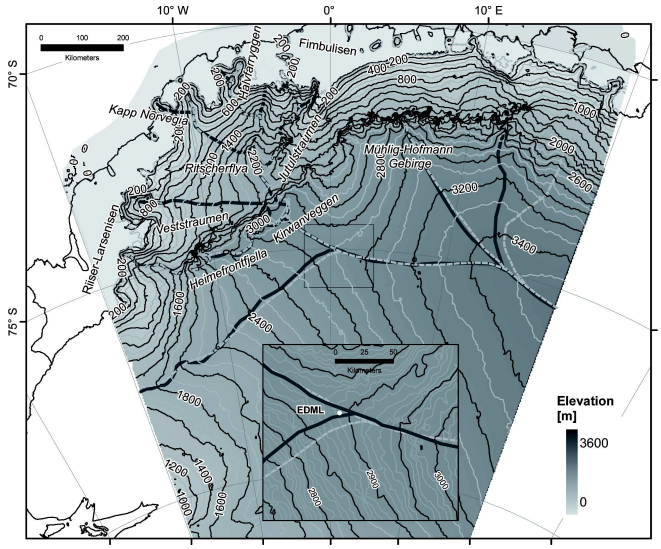

Fig. 9. A map of the re-located ice divides (bold black lines) and the location of the ice divides, based on the DEM of Bamber and Huybrechts (1996) (dashed grey lines). The thin black line showing the grounding line and the coastline based on MOA (Haran and others, 2006). The white dot in the small map shows the location of EDML.

few additions were made. Some ice divides end at the mountain range, because their course cannot be traced through the mountains.

The re-location of an ice divide may change the direction of the flow at a given point. Therefore, the re-location is of particular interest near the EDML deep-drilling site, because it helps to interpret the climate proxies derived from ice-core analyses. Because of the higher resolution of the improved DEM, the location of the transient ice divide near Kohnen station and thus near EDML is also improved.

The location of the northern ice divide in Figure 10 changes only slightly. The forking is shifted about 15 km downstream, which results in a 10 to 15 km shift westwards of the southern ice divide. Further on, EDML is located between two ice divides, being about 4 km apart from the northern divide and about 2.5 km from the southern one. With an ice thickness of 2782 ± 5 m, EDML is in-between the region, which is affected by the flow near ice divides. The surface velocity measurements presented in Table 2 and in Wesche and others (2007) show the flow field around EDML. Looking at DML07 and DML27, both are about 4 km apart from the ice divides, the flow directions are parallel to the course of the ice divide, which confirms the basic principle of flow near an ice divide. DML02 (25 km apart) and DML26 (8 km apart) show a divergent flow to the location of the ice divide, which shows that the area around the ice divide, which is influenced by the special flow regime, is about three times the ice thickness.

CONCLUSIONS

The improved DEM presented in this investigation is a combination of four different data sets. The accuracy assessment of ICESat ice sheet altimetry data shows the realistic valuation of the spaceborne laser altimetry. Since the remotely sensed data are leveled to high accurate ground based GPS data, the DEM represents the true surface elevation very well. Using this DEM, ice dynamic modeling will be improved significantly. Another important part is the localization of the topographic ice divides in DML. Due to the 2.5 km × 2.5 km resolution of the DEM, the course of the ice divides could be

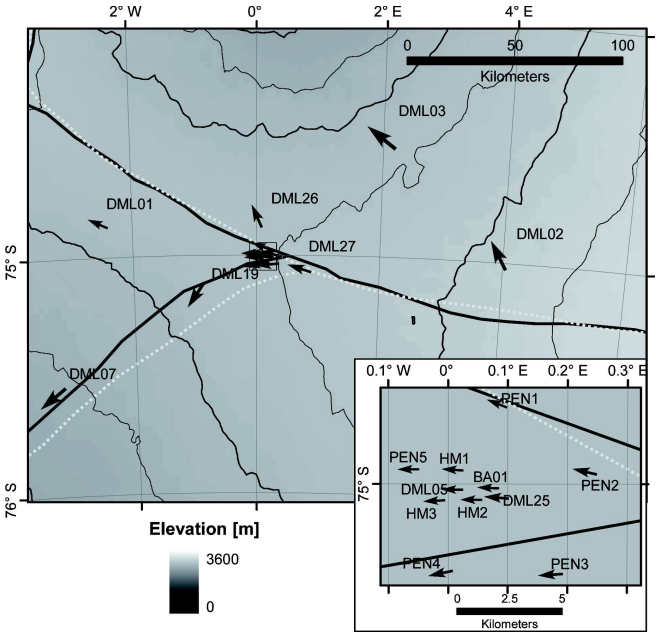

Fig. 10. A zoom to the static GPS measurements. The graduated arrows present the flow velocities of the 18 static points. In the small map it is zoomed to the rectangle marked in the big map. The black lines represent the new ice divide, the dashed grey lines the old. In the background, the new DEM with 100 m contour lines.

determined more precisely than using JLB97 with an resolution of 5 km $\times$ 5 km (Bamber and Bindschadler, 1997). With the aid of the new ice divides, the estimation of the origin of the ice, drilled at Kohnen station (Huybrechts and others, 2007), can be improved, which contributes to the accurate paleoclimatic interpretation of the climate proxies.

ACKNOWLEDGMENTS

This work was supported by the Bundesministerium für Wirtschaft (BMWi) through the CryoVEx activities 50EE0505. The authors thank the National Snow and Ice Data Center for providing the ICESat data and a special thank to Jennifer Bohlander, for providing the MOA grounding and coast lines.

References

Bamber, J. L. and R. A. Bindschadler, 1997. An improved elevation dataset for climate and ice-sheet modelling: validation with satellite imagery, *Annals of Glaciology*, **25**, 439–444.

Bamber, J. L. and P. Huybrechts, 1996. Geometric boundary conditions for modelling the velocity field of the Antarctic ice sheet, *Annals of Glaciology*, **23**, 364–373.

Brenner, A. C., R. A. Bindschadler, R. H. Thomas and H. J. Zwally, 1983. Slope-induced errors in radar altimetry over continental ice sheets, *Journal of Geophysical Research*, **88**(C3), 1617–1623.

Brenner, A. C., H. J. Zwally, C. R. Bentley, B. M. Csatho, D. J. Harding, M. A. Hofton, J.-B. Minster, A. Roberts, Saba J. L., R. H. Thomas and D. Yi, 2003. Derivation of range and range distribution from laser pulse waveform analysis for surface elevations, roughness, slope, and vegetation heights, *GLAS Algorithm Theoretical Basis Document Version 4.1*, **Greenbelt, MD**, Goddard Space Flight Center.

228 Clark, P. U. and A. C. Mix, 2002. Ice sheet and sea level of the Last Glacial Maximum, *Quatenary Science Reviews*, **21**, 1–7.

229 Egbert, G. D and S. Y. Erofeeva, 2002. Efficient inverse modeling of barotropic ocean tides, *Journal of Atmospheric and*
230 *Oceanic Technology*, **19**(2), 183–204.

231 Fricker, H. A., A. Borsa, B. Minster, C. Carabajal, K. Quinn and B. Bills, 2005. Assessment of ICESat performance at the
232 salar de Uyuni, Bolivia, *Geophysical Research Letters*, **32**(L21S06).

233 Haran, T., J. Bohland, T. Scambos, T. Painter and M. Fahnestock, 2006. MODIS mosaic of Antarctica (MOA) image map,
234 *Boulder, Colorado*, **National Snow and Ice Data Center**, Digital media.

235 Honeywell AA-300 Manual, 1998. System description and installation manual - AA-300 Radion Altimeter System.

236 Huybrechts, P., 2003. Antarctica: modelling, In: Mass Balance of the Cryosphere: Observations and Modeling of Contem-
237 porary and Furture Changes, eds. Bamber. J. L. and A. J. Payne, Cambrigde University Press, chap. 13, 491–524.

238 Huybrechts, P., O. Rybak, F. Pattyn, U. Ruth and D. Steinhage, 2007. Ice thinning, upstream advection, and non-climatic
239 biases for the upper89EDML ice core from a nested model of the Antarctic ice sheet, *Climate of the Past*, **3**, 577–589.

240 King, M., 2004. Rigorous GPS data-processing strategies for glaciological applications, *Journal of Glaciology*, **50**(171), 601–
241 607.

242 King, M. and L. Padmann, 2005. Accuracy assessment of ocean tide models around Antarctica, *Geophysical Research Letters*,
243 **32**(L23608).

244 Liu, H., K. C. Jezek, B. Li and Z. Zhao, 2001. Radarsat Antarctic Mapping Project digital elevation model version 2, *Boulder*
245 *CO*, **National Snow and Ice Data Center**, Digital media.

246 Ray, R. D., 1999. A global ocean tide model from TOPEX/Poseidon altimetry: GOT99.2, *NASATechnical Memo*, (209478).

247 Raymond, C.F., 1983. Deformation in the vicinity of ice divides, *Journal of Glaciology*, **29**(103), 357–373.

248 Rott, H., K. Sturm and H. Miller, 1993. Active and passive microwave signatures of Antarctica firn by means of field
249 measurements and satellite data, *Annals of Glaciology*, **17**, 337–343.

250 van der Veen, C. J., 1999. Fundamentals of Glacier Dynamics, Balkema, Rotterdam u.a.

251 Wesche, C., O. Eisen, H. Oerter, D. Schulte and D. Steinhage, 2007. Surface topography and ice flow in the vicinity of the
252 EDML deep-drilling site, Antarctica, *Journal of Glaciology*, **53**(182), 442–448.

253 Wesche, C., S. Riedel and D. Steinhage, submitted. Precise surface topography of the grounded ice tongues at the Ek-
254 strömisen, Antarctica, based on several geophysical data sets, *ISPRS Journal of Photogrammetry and Remote Sensing*.

255 Zwally, H.J., B. Schutz, W. Abdalati, J. Abshire, C. Bentley, A. Brenner, J. Bufton, J. Dezio, D. Hancock, D. Harding, T. Her-
256 ring, B. Minster, K. Quinn, S. Palm, J. Spinhirne and R. Thomas, 2002. ICESat's laser measurements of polar ice, atmo-
257 sphere, ocean, and land, *Journal of Geodynamics*, **34**, 405–445.

258 Zwally, H. J., R. Schutz, C. Bentley, T. Bufton, T. Herring, J. Minster, J. Spinhirne and R. Thomas, 2007. GLAS/ICESat
259 L2 Antarctic and Greenland Ice Sheet Altimetry Data V028, *Boulder, CO*, **National Snow and Ice Data Center**, Digital
260 media.

PAPER IV

A new digital elevation model in western Dronning Maud Land (Antarctica), based on differential SAR Interferometry

IEEE Transactions on Geoscience and Remote Sensing, accepted

A spatially adjusted elevation model in Dronning Maud Land, Antarctica, based on differential SAR Interferometry

Reinhard Drews, Wolfgang Rack, *Member, IEEE* Christine Wesche, Veit Helm

Abstract—In this study we derived a new digital elevation model (DEM) in western Dronning Maud Land (Antarctica) by using differential interferometric SAR (DInSAR). It is based on acquisitions from the European Remote Sensing satellites ERS-1/2 in combination with IceSAT's geoscience laser altimeter (GLAS). The DEM is compiled out of 116 scenes from the ERS-1 ice phase and the ERS-1/2 (tandem) mission between 1994 and 1997. Profiles from laser altimetry of the IceSAT satellite were taken in 2003 and served as ground control for the DEM generation. By using three different SAR processors we separate internal processing errors from external errors such as an unknown atmospheric contribution. The mosaicked DEM includes the grounded ice sheet on the gently sloped catchment basins of the Ekströmisen and the Veststraumen as well as parts of the Heimefront Fjella mountain range. It covers an area of approximately 130 000 km^2 on a (50x50) m grid. For the uncertainty estimation independent IceSAT tracks from 2004-2007 were used together with GPS and airborne LIDAR data. The height error varies spatially in average from 1-2 meters up to 15-20 meters. No systematic changes were detected over the 10 year period. Also the data set does not allow easily to assess variations in radar penetration depth into snow. The DEM was filtered and resampled iteratively in order to account for the spatial variation of noise. It mostly outperforms other DEMs currently available in the region and will serve for future elevation models from the Cryosat and the Terra SAR-X tandem mission as the late 1990s baseline to monitor temporal changes in ice sheet elevation.

Index Terms—Digital Elevation Model, Differential SAR Interferometry, Dronning Maud Land, Antarctica, GLAS, IceSAT

1 Introduction

THE surface elevation on the coastal margins of the Antarctic ice sheet is largely unknown at the required accuracy to monitor short term temporal changes. Currently available Digital Elevation Models (DEMs) in our area of interest are the RAMPv2 [14], the GLAS/IceSAT-model [6], and the JBL97-model [10]. The RAMPv2 originates from the Radarsat Mapping Project and is mainly deduced from ERS-1's radar altimeter. It is gridded to 200 meters. In areas of steep relief it is combined with terrestrially derived data like airborne data and GPS measurements from the Antarctic Digital Database. JBL97 is a DEM with 5 km postings and is based on ERS-1 radar altimetry as well [3]. The GLAS/IceSAT DEM is deduced from IceSAT's laser altimeter and was released from the National Snow and Ice Data Center (NSIDC) in 2007. In our area of interest RAMPv2 deviates partly more than 150 meters from JBL97, GLAS/IceSAT and GPS profiles (see Fig. 1). Glas/IceSAT performs better than JBL97 especially in the vicinity of underlying IceSAT tracks.

Precise and highly resolved DEMs are needed for a variety of glaciological applications, such as mass balance and accumulation studies [1], input for numerical flow models, mapping of displacement fields, or ice core analysis [18]. The previously mentioned DEMs often do not offer the needed horizontal res-

- *R. Drews, C.Wesche, and V. Helm are at the Alfred Wegener Institute for Polar and Marine Research, Am Handelshafen 12, Bremerhaven, Germany.*
  E-mail: rdrews@awi.de
- *W. Rack is at the Gateway Antarctica Centre for Antarctic Studies and Research, Canterbury University, Christchurch, New Zealand*

Manuscript received XXXX XX, XXXX; revised XXXX XX, XXXX.

olution and vertical accuracy. This motivates the derivation of a DEM through a differential interferometric approach. Satelliteborne interferometric SAR (InSAR) is a well known technique to derive area-wide, fine resolution DEMs and velocity fields. Detailed introductions can be found for example in [15], [7] or [17]. Similar studies with respect to icesheets were previsously performed in [13], [11], or [2].

The authors in [2] reported localized residual elevation discrepancies between the DInSAR DEMs and IceSAT altimetry and speculated on the origins such as atmospheric contribution and varying penetration depth. Our interest is to derive a larger scale DEM using the same technique, quantify the obtainable accuracy, and link deviations to two kinds of errors: Firstly internal errors due to uncertainties within the radar/INSAR processing and secondly to external errors such as an atmospheric contribution. Secondly, we present a DEM with a varying spatial resolution which accounts for the spatial variation of noise.

2 METHODOLOGY

In an interferometric multipass procedure two acquisitions are combined to derive a mixed interferogram which contains a topographical contribution as well as a contribution from the ice sheet's displacement in-between the two acquisitions. In order to separate these two parameters a differential approach (DInSAR) as described in [13] is chosen: Under the assumption of a constant velocity flow, the displacement is canceled by differencing two interferograms of the same scene. The main processing steps comprise the SAR processing of the raw data, coregistration of the scenes, interferogram formation, phase unwrapping, differencing of the interferograms, the baseline refinement and the rectification to the resulting height map. As previously done in [21], the baseline refinement uses GCPs from IceSAT's laser altimeter (GLA 12 Release 24, Laser 1 (20.02.2002 - 29.02.2002) and Laser 2a (24.09.2003 - 18.11.2003) [22]) as tiepoints. Limitations are the restricted availability of coherent SAR image pairs and the lack of real GCPs. An unknown atmospheric contribution as well as a varying penetration depth may deteriorate the quality of the resulting DEM.

Following a user based approach we investigate the robustness and sensitivity of the SAR raw data processing by analyzing SLC data from three different SAR processors with varying scene length in azimuth. Some DEMs were derived from SLC frames from the German Processing and Archiving Facility (D-PAF; processing date between 2003 and 2007). Resulting DEMs often show phase discontinuities on the boarder of adjacent frames which cannot fully be explained by baseline inaccuracies. In order to enable strip-line processing we used Gamma's Modular SAR processor (MSP), and for comparison EarthView's advanced precision processor (APP). All other steps were performed with Gamma's interferometry software [19].

Fig. 1 displays the ERS frames which were used in this study. Alltogether 19 DEMs were separately derived and mosaicked to a final DEM. In overlapping areas, a weighted average was applied which reduced the overall noise level. The weights cc were given by the estimated coherence of the respective DEM. In detail:

$$\mathrm{DEM}_{(i,j)} = \frac{\sum_k^N cc_{(i,j)}^k \mathrm{dem}_{(i,j)}^k}{\sum_k^N cc_{(i,j)}^k} \qquad (1)$$

with

$$cc_{i,j}^k = \left\{ \begin{array}{ll} cc_{i,j}^k & \text{if} \quad cc_{i,j}^k > 0.6 \\ 0 & \text{otherwise.} \end{array} \right\}$$

where k indexes the individual DEMs and N is the number of DEMs that overlap at the location (i,j). Usually N is in between 2 and 4. A threshold for coherence was chosen to avoid areas of high noise where phase unwrapping errors are likely.

For the uncertainty estimation the final DEM is compared to IceSAT tracks as well as independent GPS and LIDAR profiles. Whereas these cover only a relatively small area, the differencing of the individual DEMs in overlapping areas gives an estimate of the DEM's accuracy on a larger scale. In order to isolate processing errors we compare independently processed raw data. This will be investigated in the next section.

3 Accuracy analysis

3.1 SAR raw-data and DInSAR processing

The SAR raw-data processing aims to reconstructs an image out of several reflected pulses, by using the Doppler history of the individual targets (see for example [8] or [9]). The resulting high resolution image is a single look complex (SLC) file which stores a complex number (in-phase and quadrature) corresponding to phase and amplitude. After the double-differencing of 4 SLCs the conversion from differential phase to height can be approximated by [16]:

$$z = \frac{\lambda r_0 \sin(\theta_0)}{4\pi} \frac{\Delta\phi_f}{B_{\perp,0}} \quad (2)$$

where the unwrapped and flattened phase ϕ_f is turned into height z (above a reference ellipsoid) by using the perpendicular component of the refined baseline B, as well as the look angle θ_0, the slant range distance r_0 and the wavelength λ. Apart from the wavelength all parameters have a range and azimuth dependency which is not marked explicitly.

Processing uncertainties can be visualized (1) by comparing overlapping areas of adjacent frames which were processed individually or (2) by comparing DEMs which are based on a set of SLCs from different SAR processors. In both cases the resulting DEMs rely on the same raw data and deviations can be entirely attributed to the SAR processing.

As a specific example we consider two adjacent frames (5157 and 5175) in track 407 which is marked with 4 in Fig. 1. From this raw data strip we derived 5 DEMs (D1,D2,Ev1,Ev2,G) which are listed in table 1. D1 and D2 are based on 8 SLCs from the german D-PAF, Ev1 and Ev2 are based on 8 SLCs from Earth-View's APP. G is based on 4 SLCs from the MSP where the raw data of the two frames was concatenated.

TABLE 1
Comparison of IceSAT GCPs to DEMs from track 407 based on SLCs from different SAR processors

id	SLCs	frame	s_{Ice} [m]
D1	D-PAF	5157	-0.32 ± 3.1
D2	D-PAF	5175	-0.35 ± 7.0
Ev1	APP	5157	0.29 ± 2.0
Ev2	APP	5175	0.40 ± 5.1
G	MSP	5157-5175	0.00 ± 3.7

At first, the individual DEMs are compared with the corresponding GCPs which were used for the baseline refinement. The mean deviation s_{Ice} in all cases scatters around zero with a standard deviation of 2 to 7 meters (see table 1). Many long IceSAT tracks show random deviations from 1 to 2 meters which points out the generally high quality of those particuar DEMs. However, in some localized areas the deviations are systematic and reach up to 10 to 15 meters which is illustrated in Fig. 2. Characteristic dents are for instance visible in the upper right and lower left corner of D2. These dents are evident in many DEMs and cannot be removed with low order polynoms in a global fit over an entire frame. From a perspective of a user it is interesting to know whether these localized deviations have geophysical reasons or if they are due to the processing. In our case many of them are due to the processing, since depending on which set of SLCs has been used they appear in different places. This can be seen in Fig. 2 where the previously mentioned dents from D2 are not visible in G.

For further investigation the 5 DEMs are differenced. The difference fields of D1, Ev1,and G as well as the difference fields of D2,Ev2, and G show deviations of up to 15 meters in some areas. Similar deviations can be seen in the overlapping area of D1 and D2. This emphasizes that most of the localized deviations along the IceSAT tracks are processing artifacts.

The magnitude of processing uncertainties can be explained with deviations in the differential phase and baselinemodels. The typical INSAR approach to correct for both inaccuracies in the state vectors and phase tilts due to SAR processing is an overall fit of GCPs to the unwrapped differential phase. This alters the baseline in a way that the resulting orbit model complies best to the used set of GCPs. As a result, deviations in the final baseline model are partly interconnected with SAR processing phase uncertainties. As an example serves Fig. 3 where the deviations in the differential phase, differential baseline, and height are plot-

ted along a range profile (indicated in Fig. 2) which intersects D1,D2, Ev2, and G. It becomes evident that the various DEMs are tilted with respect to each other. The largest tilts can be seen in the pairs D2-G and D2-D1. Similar results are obtained for the case that the two frames in G are processed seperatly.

The height differences from Fig. 3 can be modeled using equation 2. If only differences of the refined differential baseline and the differential phase are considered, the height deviation $z - z'$ can be approximated as

$$z - z' = \frac{\lambda r_0 \sin\Theta_0}{4\pi} \cdot \left(\frac{\Delta\phi_f B'_{\perp,0} - \Delta\phi'_f B_{\perp,0}}{B'_{\perp,0} B_{\perp,0}} \right) \quad (3)$$

by using formula 2. The + in the lowest plot of Fig. 3 indicate that this analytical deviation predicts the observed height deviation well. It supports the idea that differences in the baseline model and phase are in fact the main parameters for the deviation.

The deviations in the differential phase are rooted in the SAR processing. If SLCs from different SAR processors are compared (as done in [4]) they sometimes exhibit a small residual phase ramp in our case. This can be shown via auto-interferograms between APP and D-PAF SLCs (the MSP SLCs are not processed to a zero Doppler geometry and thus are not directly comparable to APP and D-PAF SLCs). Also some parameters, as for example the Doppler Centroid and its range dependency, are estimated for each individual frame so that phase discontinuities can be observed on the boarders, even if the same SAR processor has been used. In case of G we processed the SLC pairs to a common Doppler for maximum spectral overlap. Possibly tilts and dents in phase of the single SLCs are caused by differences in the estimation of the Doppler Centroid and its range dependency. For the latter, the D-PAF SLCs are usually based on a quadratic function whereas MSP's representation tends to be linear. The low contrast within the scenes as well as larger squint angles in the southern hemisphere [19] may be an explanation why the precise estimation of the Doppler Centroid is limited. What is seen in Fig. 3 as the deviation in differential phase is the summation of tilts from the individual SLCs.

It should be noted that in other examples the differences in a similar comparison did not exceed the general noise level. Also a comparison with independent GCPs which is shown in a section below points to a higher accuracy in other areas of the DEM. However, from a perspective of a user it must be assumed that processing uncertainties are not always negligible. Although strip-line processing removes discontinuities between frame boundaries it does not necessarily raise the overall accuracy. Also the global comparison with IceSAT GCPs alone does not reflect the DEMs accuracy. We also investigated if localized deviations between the DEM and GCPs may be attributed to the level of backscattered power and penetration depth. The absence of any dependence may be an indication that a varying depth of the effective point of scattering cannot be detected or is only of minor importance compared to the previously mentioned processing artifacts.

We globally adjusted each individual DEM with a third order polynomial to the GCPs, which generally improves the DEM's quality and diminishes differences in overlapping areas. However, only in few cases it is possible to completely remove dents using polynomial fits.

3.2 Atmospheric Contribution

Variations in tropospheric water vapour content are a source of lateral inhomogenities in refractivity ([20], [7]) which is often neglected for the comparable dry polar atmosphere. This is illustrated in Fig. 4 showing a residual DEM which was derived from frame 5661 of track 31 and track 45. The mean elevation of that area is 1800 m. Track 31 was recorded several times in March 1994 (ERS-1 ice phase), track 45 is a combination from interferograms of 1996 and 1997. A wave like pattern with an amplitude of about 20 meters and a wavelength of about 10 km can be seen in the difference field. In this obvious case the pattern can be recognized in single interferograms from track 31 (9-12 and 12-15 March 1994), and the pattern can be traced to the data acquisition of 12 March 1994, 1:40 UTC. A NOAA AVHRR satellite image (11 March 1994, 23:17 UTC) shows a dominant

high cloud band in the area of the image frame, which is related to a deep pressure system with its centre located off the coast at about 12W/68S (24 hour polar MM5 reanalysis forecast, Byrd Polar Research Center). It causes a strong south-easterly flow over the Heimefrontfjella mountain range. Wavelike structures in the AVHRR image with similar spatial scales cannot be spotted exactly in the area of the ERS SAR image but in the area to the northwest. This is probably because the two hour time difference in data acquisition between the AVHRR and the SAR image. Temperature differences indicate a close sequence of high and low clouds with significant differences in water vapour content and precipitable water. The wave amplitude in the March 12 SAR image corresponds to a total path delay of 9 mm. This particular frame was not considered for the DEM, but it is a showcase that in general atmospheric contributions could be large and cannot be neglected, especially for low baselines. Because the data base for differential interferograms in this area is limited, we cannot assume that this contribution is cancelled out by our stacking procedure.

3.3 Validation with GCPs from IceSAT, kinematic GPS, and airborne laser altimetry

For the comparison the DEM is sampled to a 50 m grid. As GCPs serve IceSAT tracks, profiles from Airborne Laser Altimetry and GPS measurements.

IceSAT · The comparison includes independent IceSAT tracks from GLA12 Release 28 (L3b - L3h) which were recorded in 2004-2007. A comparison with the individual laser periods in each year does not reveal a systematic change in surface elevation compared to our DEM. Therefore we combine all laser periods for further comparison. The height error of the laser altimetry varies in-between 14 to 59 cm as a function of surface slope [5]. The mean deviation compared to our DEM is $s_{IceSAT} = (-0.9 \pm 9.6)$ m. For the comparison areas with a coherence below 0.8 were masked. This excluded about 10% of the GCPs. Additionally a minor part ($\sim$ 0.01%) of the points with deviations larger than 50 m were excluded and regarded as outliers caused for example by phase unwrapping errors in areas with high noise. The corresponding histogramm is displayed in Fig. 5. The deviations do not follow a Gauss distribution, but have longer tails in the positive and negative domain. This can be caused amongst others by hidden phase unwrapping errors, unnoticed atmospheric contributions, or by an actual change of heights in between the acquisitions of the ERS scenes and the IceSAT tracks. Generally the deviations to IceSAT tracks in areas of good coherence (> 0.9) are about 1-2 meters, whereas in areas of lower coherence the standard deviation increases up to 15-20 m. The localized nature of deviations which was already considered in section 3.1 is still apparent in the mosaicked DEM and are probably often due to residual processing errors. Further independent measurements are given by GPS and airborne laser altimetry. Both data sets enable the evaluation of the DEM inbetween IceSAT tracks.

Airborne Laser Altimetry · The airborne laser scanner altimetric survey took place December 2007. The position of the profile is illustrated in Fig. 1. It was flown with the POLAR5, the new polar scientific aircraft of the Alfred Wegener Institute. Apart from the primary laser scanner instrumentation (RIEGL LMS-Q280), the POLAR5 was equipped with a Honeywell inertial navigation system (INS), 4 GPS receivers and ASIRAS (ESA's Airborne SAR Interferometric Altimeter System). The laser instrumentation scanned at an approximate off nadir angle of +/-22.5 with a scan rate of 80 Hz. Each scan consisted of 113 single laser shots. The average flight level of 700 m above ground together with an average ground speed of 67 m/s result in an along- and across-track laser point seperation of 1 m and 6 m respectively. As reference for the differential GPS post-processing a GPS ground station was set up at Novo station, Sanae. The geocoded laser scanner DEM of the 115 km long profile was determined using post-processed GPS, INS and the calibrated laser scanner range measurements. The accuracy of the DEM, including the GPS uncertainty, is within 10 cm, with smaller errors at the vicinity of the nadir scan angle. This is a similar to the results obtained by [12] over Greenland.

After filtering the DInSAR DEM with a coherence threshold of 0.8, which excluded 10% of the DInSAR grid points, the difference of the laser scanner DEM and the DInSAR DEM reveals a deviation of $s_{ALS} = (2.9 \pm 4.1)$ m. The constant offset may be due to the processing or possibly to a real change of height as the ALS data is from 2007. The small standard deviation emphasizes the good quality of the DInSAR DEM in that region. Local deviations are not apparent. A corresponding histogram is illustrated in Fig. 5 and shows that the deviations follow a Gauss distribution.

GPS · An approximately 400 km long GPS traverse is illustrated in Fig. 1. It connects the german over-wintering station Neumayer with Kohnen and was collected in 2005. The GPS antenna was mounted on top of a dragged living container. A recording interval of 1 s and the along track velocity of about 10 - 12 km/h results in an along track spacing of 3 m. The GPS data was processed with a commercial post-processing software including reference stations, precise ephemerides, and ionospheric-free solutions. As reference stations served the South African station Sanea IV (2.84°W and 71.67°S) and the Finnish station Aboa (13.41°W and 73.04°S). Because of their recording interval of 30 s and 15 s, the reference data was interpolated to an 1 s interval by using INTERPO from the National Geodetic Survey. The mean accuracy is taken from the processing report of the software, since no crossover points can be found. Overall 78 % of the data points have an accuracy in between (0.05 - 0.40) m and all data points have have deviations smaller than 1 m. For the comparison the GPS points are sampled to the respective cell sizes of the DInSAR DEM, JBL97, GLAS/IceSAT, and RAMPv2. The DInSAR DEM was filtered with a threshold in coherence of 0.8 which excluded approximately 10 % of the available grid points. In this example JBL97 and GLAS/IceSAT show smaller variances (0-30) m compared to RAMPv2 which deviates over large areas more than 100 m. The DInSAR DEM shows localized deviations as already observed in the comparison with IceSAT tracks, however it approximates the GPS traverse better in shape as well as absolute value compared to the other DEMs. The deviation is $s_{GPS} = (-1.2 \pm 8.0)$m. A corresponding histogram is illustrated in figure 5. The longer tails in the positive and negative domain are likely to be caused by the same effects as already mentioned during the comparison with the IceSAT data.

4 Spatial variation of noise

As discussed above, the quality of the DEM varies spatially with the present coherence, atmospheric contribution and possibly varying penetration depth. With decreasing coherence the general noise level increases. Averaging the DEM by a factor of $n \times n$ decreases the standard deviation by a factor of n at the cost of spatial resolution. We chose a simple algorithm to resample the DEM iteratively to lower the standard deviation under a threshold of 5 m. Therefore we estimated the standard deviation on the 50 meter grid in detrended 750x750 m windows. If the standard deviation was below the threshold the sub-windows were excluded, otherwise the DEM was resampled with a 50 m increment up to a maximum cell size of 500 m. This results in a DEM with a varying spatial resolution which is shown in Fig. 6. Especially areas with steep relief in the Heimefront Fjella mountain range and some coastal areas had a lower coherence and needed higher resampling or were completely masked out. The largest part of the DEM however remains on a 50 m grid.

5 Conclusion

In this study 19 independent DEMs were derived through a differential interferometric approach. The mosaicked DEM covers an area of approximately $1.30 \cdot 10^5 \text{km}^2$. Overlapping parts of the adjacent frames and auto-interferograms were used to separate different error sources. In that process a cross comparison between DEMs, which are based on the same raw data but on different SLCs was performed. It could be shown that processing errors are not always negligible, and often depend on the processing history of the used SLCs. From a user perspective it is difficult to evaluate and adjust possible inaccuracies within the processing

which superimpose geophysical effects such as a varying penetration depth. Large obvious errors from atmospheric contributions are only visible in a small part of the DEM. The overall coherence is high, but also areas of lower coherence are well mapped. The DEM was resampled iteratively with a spatially varying resolution and an estimated standard deviation below 5 m. The largest part of the DEM is on a 50-m grid. For future work more sophisticated methods will be applied to smooth the DEM.

A comparison with an approximately 400 km long GPS traverse on the 50-m grid reveals an error of $s_{GPS} = (-1.2 \pm 8)$ meters. The deviations to the airborne laser altimetry profiles are $s_{ALS} = (2.9 \pm 4.1)$ meters and towards IceSAT GCPs $s_{Ice} = (0.7 \pm 9.7)$ meters. Since other available DEMs show larger deviations, this DEM can be considered to have the best horizontal and vertical resolution currently available in that region. Although the overall accuracy is high, the used data sets and methods do not easily allow to assess a variation of radar penetration depth into snow.

ACKNOWLEDGMENTS

The ERS SAR data were made available by ESA through the project AO3108. Airborne laser data were acquired for the DLR project 50EE0505.

The authors would like to thank C. Werner from Gamma Remote Sensing for help during the processing and M. Bässler from the TU Dresden for the provision of sample data. Further we thank the Gateway Antarctica for enabling a six month internship for R. Drews. The stay was financed by the "Evangelisches Studienwerk e.V. Villigst".

IceSAT, RAMP, and AVHRR satellite data were provided through NSIDC. MM5 reanalysis data were provided by D. Steinhoff, Polar Meteorology Group, Byrd Polar Research Center. Thanks to H. Koivula and J. Mäkinen, Finnish Geodetic Institute, for providing the Aboa GPS reference data.

REFERENCES

[1] H. Anschütz, O. Eisen, H. Oerter, D. Steinhage, and M. Scheinert, "Investigating small-scale variations of the recent accumulation rate in coastal dronning maud land, east antarctica," *Annals of Glaciology*, vol. 46, pp. 14–21, 2007.

[2] S. Baek, O. Kwoun, A. Braun, L. Zhong, and C. Shum, "Digital elevation model of king edward vii peninsula, west antarctica, from sar interferometry and icesat laser altimetry," *IEEE Geoscience and Remote Sensing Letters*, vol. 2, no. 4, pp. 413–417, Oct. 2005.

[3] J. Bamber and J. Gomez-Dans, "The accuracy of digital elevation models of the antarctic continent," *Earth and Planetary Science Letters*, vol. 237, pp. 516–523, sep 2005.

[4] A. Barmettler, P. Pasquali, D.Small, and D. Nuesch, "Cross-compatibility of ers-slc-products," *Proceedings FRINGE SAR Interferometry Working Group: 2nd Workshop, Zürich*, October 1996.

[5] A. C. Brenner, J. P. DiMarzio, and H. J. Zwally, "Precision and accuracy of satellite radar and laser altimeter data over the continental ice sheets," *IEEE Transactions on Geoscience and Remote Sensing*, vol. 45, no. 2, pp. 321 – 331, Feburary 2007.

[6] J. DiMarzio, A. Brenner, R. Schutz, C. Shuman, and H. Zwally, "Glas/icesat 500 m laser altimetry digital elevation model of antarctica." *Boulder, Colorado USA: National Snow and Ice Data Center. Digital media.*, 2007.

[7] R. Hanssen, *Radar Interferometry, Data Interpretation and Error Analysis*. Kluwer Academic Publishers, 2001.

[8] A. Hein, *Processing of SAR Data*. Springer, 2004.

[9] F. W. I. Cumming, *digital processing of Synthetic Aperture Radar data*. Artech House, 2005.

[10] R. B. J. Bamber, "An improved elevation dataset for climate and ice-sheet modelling: validation with satellite imagery," *Annals of Glaciology*, vol. 25, pp. 438–444, 2001.

[11] I. Joughin, D. Winebrenner, M. Fahnestock, R. Kwok, and W. Krabill, "Measurements of ice-sheet topography using satellite radar interferometry," *Journal of Glaciology*, vol. 42, no. 140, pp. 10 – 22, 2005.

[12] W. B. Krabill, W. Abdalati, E. B. Frederick, S. S. Manizade, C. F. Martin, J. G. Sonntag, R. N. Swift, R. H. Thomas, and J. G. Yungel, "Aircraft laser altimetry measurement of elevation changes of the greenland ice sheet: Technique and accuracy assessment," *J. Geodyn.*, vol. 34, no. 3-4, p. 357, 2002.

[13] R. Kwok and M. Fahnestock, "Ice sheet motion and topography from radar interferometry," *IEEE Transactions on Geoscience and Remote Sensing*, vol. 34, no. 1, pp. 189–200, Januar 1996.

[14] H. Liu, K. Jezek, B.Li, and Z.Zhao, "Radarsat antarctic mapping project digital elevation model version 2," *Boulder, CO: National Snow and Ice Data Center. Digital media.*, 2001.

[15] J. Mohr, N. Reeh, and S. Madsen, "Three-dimensional glacial flow and surface elevation measured with radar interferometry," *Nature*, vol. 391, January 1998.

[16] P. A. Rosen, S. Hensley, H. A. Zebker, F. H.Webb, and E. J. Fielding, "Surface deformation and coherence measurements of kilauea volcano, hawai, from sir-c radar interferometry," *Journal of Geophysical Research*, vol. 101, pp. 23 109–23 125, 1996.

[17] R. Rosen, S. Hensley, I. Joughin, S. F. Li, E. Rodríguez, and R. Goldstein, "Synthetic aperture radar interferometry," *Proceedings of the IEEE*, vol. 88 No. 3, march 2000.

[18] G. Rotschky, W. Rack, W. Dierking, and H. Oerter, "Retrieving snowpack properties and accumulation estimates from combination of sar and scatterometer measure-

ments," *IEEE Transactions on Geoscience and Remote Sensing*, vol. 44, no. 4, pp. 943–956, April 2006.

[19] C. Werner, U. Wegmüller, T. Strozzi, and A. Wiesmann, "Gamma sar and interferometric processing software," *ERS-EnviSAT Symposium, Gotheburg, Sweden*, May 2002.

[20] S. Williams, Y. Bock, and P. F., "Integrated satellite interferometry: Tropospheric noise, gps estimates and implications for interferometric synthetic aperture radar products," *Journal of geophysical research*, vol. 103, pp. 27 051–27 068, November 1998.

[21] H. A. Zebker, C. L. Werner, P. A. Rosen, and S. Hensley, "Accuracy of topographic maps derived from ers-1 interferometric radar," *IEEE Transactions on Geoscience and Remote Sensing*, vol. 32, no. 4, pp. 823–836, July 1994. [Online]. Available: citeseer.ist.psu.edu/zebker94accuracy.html

[22] H. J. Zwally, R. Schutz, C. Bentley, J. Bufton, T. Herring, J. Minster, J. Spinhirne, and R. Thomas, "Glas/icesat l2 antarctic and greenland ice sheet altimetry data v001," *Boulder, Colorado USA: National Snow and Ice Data Center. Digital media.*, 2003.

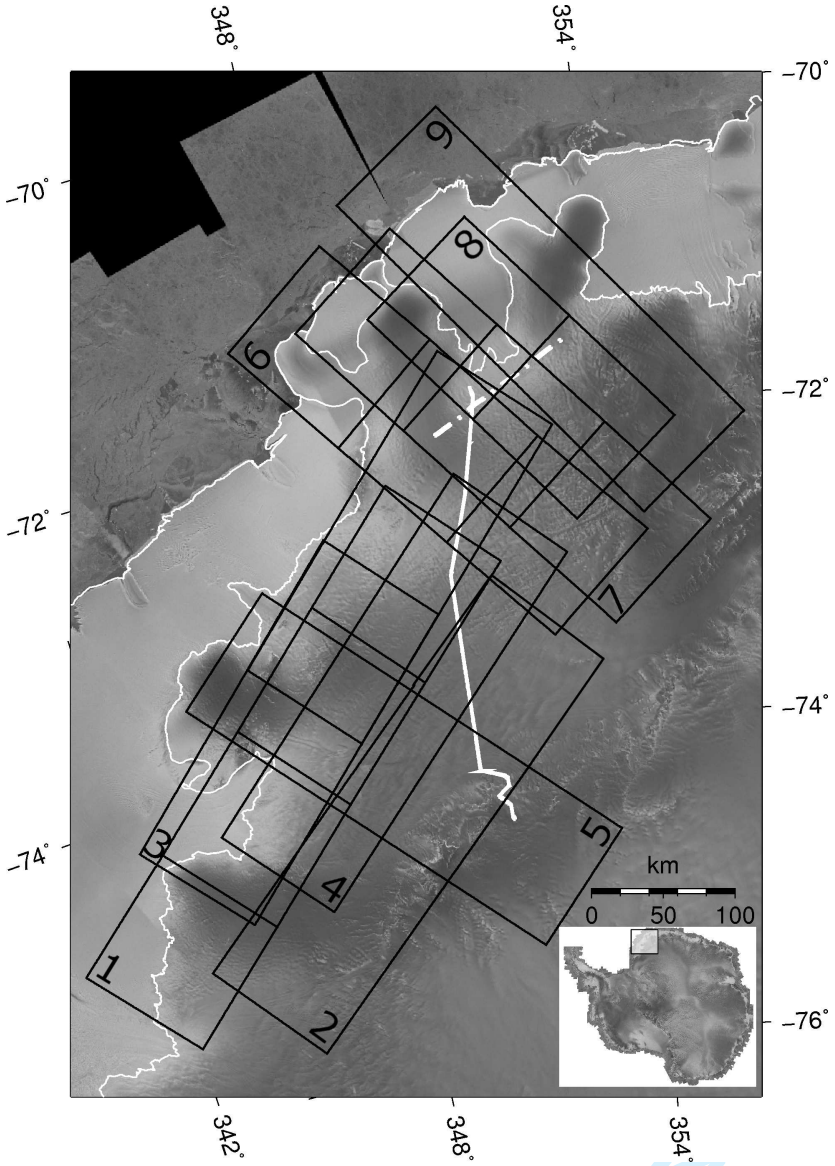

id	track	frame	date	differential $\bar{B}_{\perp}$ (m)
1	450	5139-5193	2/3 Nov-23/24 Mar 95/96	67
2	35	5157-5193	12/15/18 Mar 94	101
3	221	5103-5139	5/6 Mar-9/10 Apr 1996	233
3	221	5157-5175	17/18 Oct-9/10 Apr 95/96	86
4	407	5139-5175	30/31 Oct-18/19 Mar 95/96	235
5	17	5607-5643	14/17/20 Mar 94	27
6	31	5661-5697	06/09/12 Mar 1994	81
7	45	5661-5679	22/23 Mar-13/14 Mar 96/97	193
8	2	5679	15/16 Jan-19/20 Feb 1996	230
9	460	5679-5715	16/17 Feb-22/23 Mar 96	159

Fig. 1. **Overview of the used ERS satellite frames. White solid line: GPS traverse from Neumayer to Kohnen. White dashed line: the airborne laser scanner profile.**

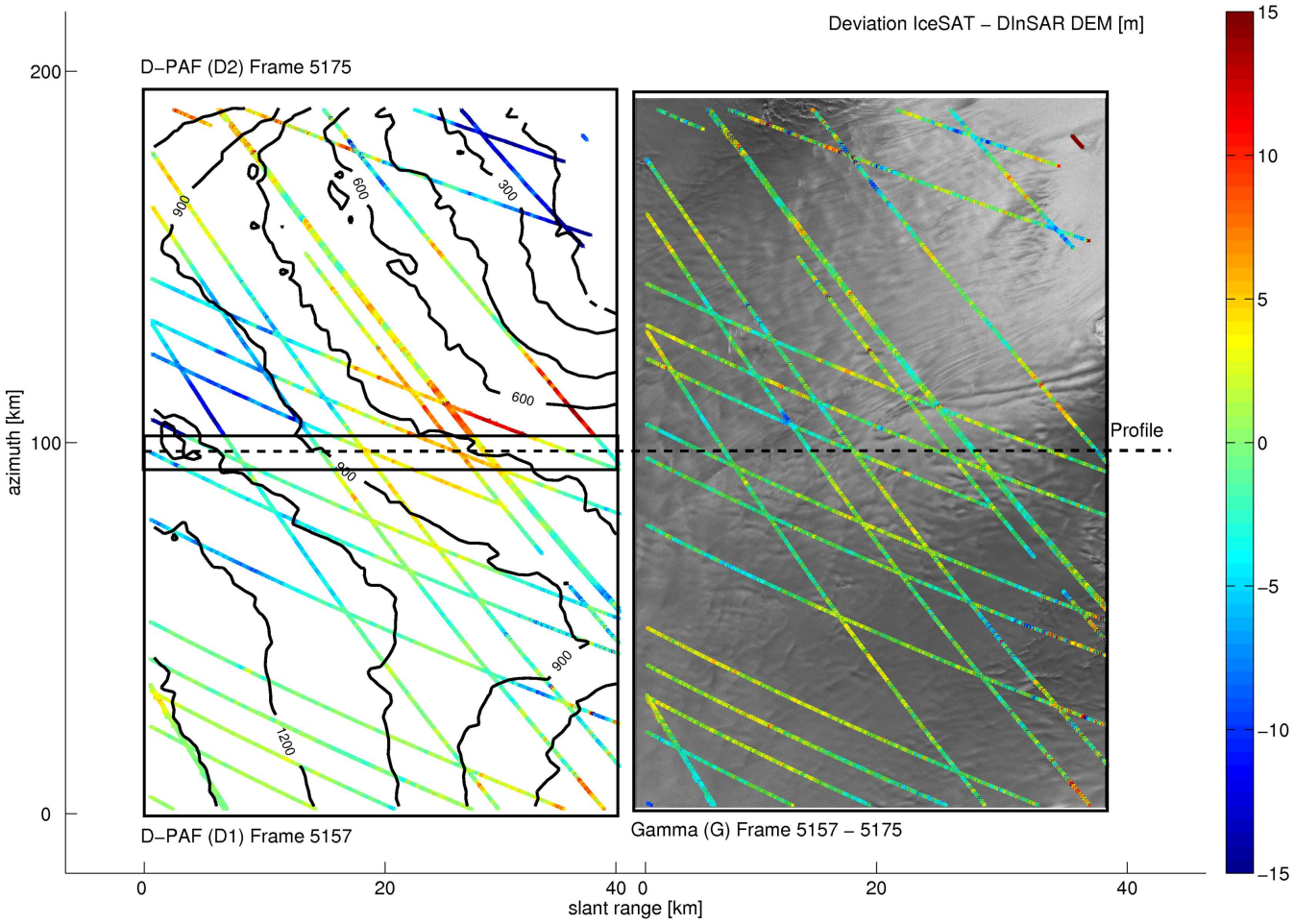

Fig. 2. **Comparison of IceSAT ground control points with DEMs based on different SAR processors. Localized dents appear as processing artifacts for instance in the upper left and lower right corner of D2.**

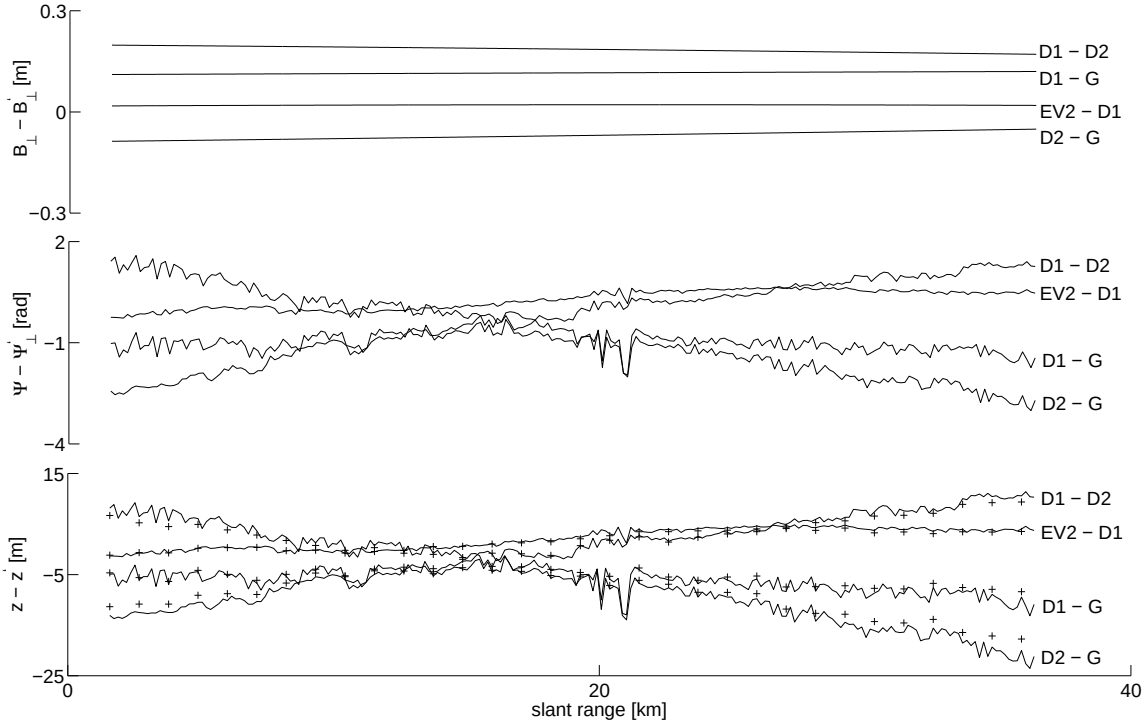

Fig. 3. **Comparison of differential perpendicular Baseline $B_\perp$, differential phase ϕ, and height z for a profile in range within the overlapping areas of independently processed DEMs (D1,D2 with D-PAF, Ev1 with EarthView, and G with MSP). The + in the lowest plot mark the predicted height error according to equation 3. The profiles are gridded to a 160 m raster for reasons of visibilty.**

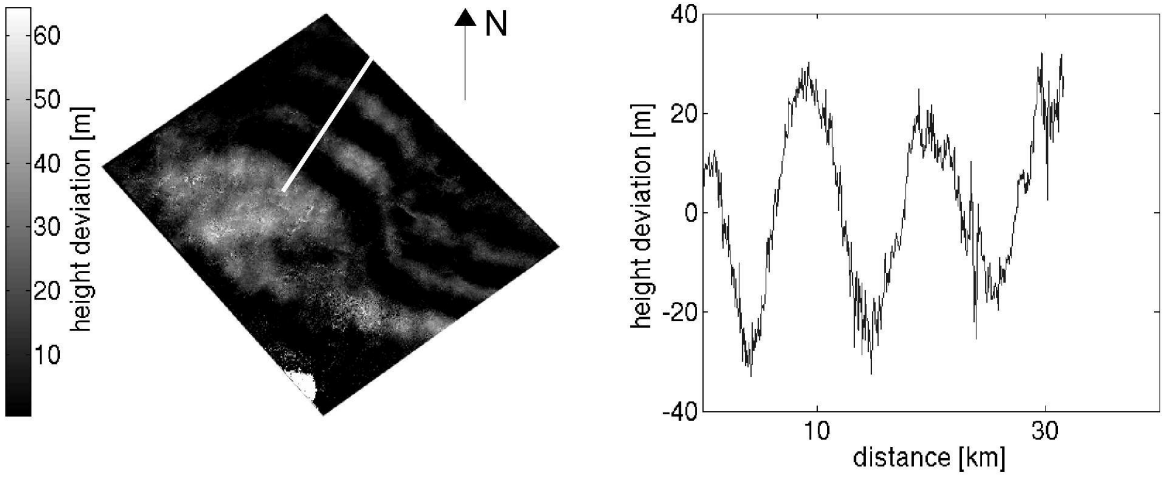

Fig. 4. **Differences in DEMs from track 031 (1996) and track 045 (1996/1997) in frame 5661. On the right is a profile across the wave like structure (marked with white line on the left).**

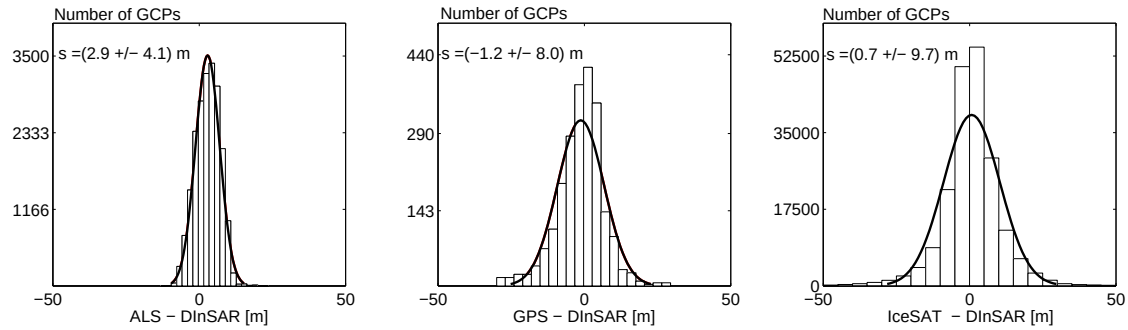

Fig. 5. **Histogram of the DInSAR DEM compared to IceSAT, GPS and ALS ground control points. The DInSAR data was filtered with a threshold of 0.8 in coherence, which excluded approximately 15 percent of the IceSAT GCPs and less than 10 percent of the ALS and GPS points. The black line represents the corresponding Gaussian distribution.**

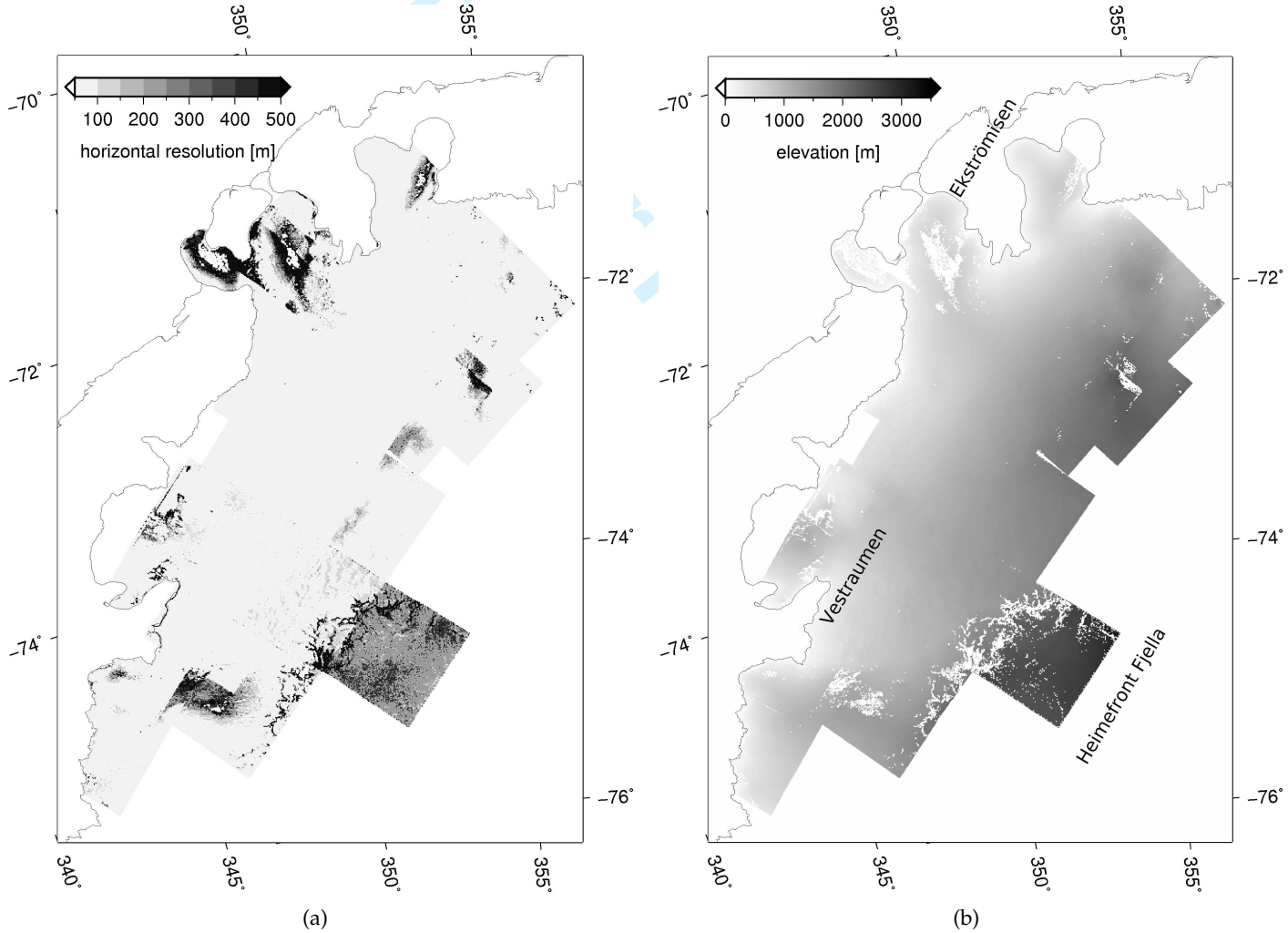

Fig. 6. **Horizontal resolution (a) and resampled final DEM for Dronning Maud Land (b). Areas in (b) with a standard deviation higher than 5 m are masked out.**